Check for updates

AMERICAN THORACIC SOCIETY DOCUMENTS

Quantitative Imaging Metrics for the Assessment of Pulmonary Pathophysiology

An Official American Thoracic Society and Fleischner Society Joint Workshop Report

Connie C. W. Hsia, Jason H. T. Bates, Bastiaan Driehuys, Sean B. Fain, Jonathan G. Goldin, Eric A. Hoffman, James C. Hogg, David L. Levin, David A. Lynch, Matthias Ochs, Grace Parraga, G. Kim Prisk, Benjamin M. Smith, Merryn Tawhai, Marcos F. Vidal Melo, Jason C. Woods, and Susan R. Hopkins; on behalf of the American Thoracic Society and the Fleischner Society

This official workshop report was approved by the American Thoracic Society on October 1, 2022, and the Fleischner Society on September 20, 2022

Abstract

Multiple thoracic imaging modalities have been developed to link structure to function in the diagnosis and monitoring of lung disease. Volumetric computed tomography (CT) renders three-dimensional maps of lung structures and may be combined with positron emission tomography (PET) to obtain dynamic physiological data. Magnetic resonance imaging (MRI) using ultrashort–echo time (UTE) sequences has improved signal detection from lung parenchyma; contrast agents are used to deduce airway function, ventilation–perfusion–diffusion, and mechanics. Proton MRI can measure regional ventilation-perfusion ratio. Quantitative imaging (QI)–derived endpoints have been developed to identify structure–function phenotypes, including air–blood–tissue volume partition, bronchovascular remodeling, emphysema, fibrosis, and textural patterns indicating architectural alteration. Coregistered landmarks on paired images obtained at different lung volumes are used to infer airway caliber, air trapping, gas and blood transport, compliance, and deformation.

This document summarizes fundamental "good practice" stereological principles in QI study design and analysis; evaluates technical capabilities and limitations of common imaging modalities; and assesses major QI endpoints regarding underlying assumptions and limitations, ability to detect and stratify heterogeneous, overlapping pathophysiology, and monitor disease progression and therapeutic response, correlated with and complementary to, functional indices. The goal is to promote unbiased quantification and interpretation of *in vivo* imaging data, compare metrics obtained using different QI modalities to ensure accurate and reproducible metric derivation, and avoid misrepresentation of inferred physiological processes. The role of imaging-based computational modeling in advancing these goals is emphasized. Fundamental principles outlined herein are critical for all forms of QI irrespective of acquisition modality or disease entity.

Keywords: ventilation-perfusion-diffusion; lung mechanics; computed tomography; positron emission tomography; magnetic resonance imaging

ORCID IDs: 0000-0003-1995-1407 (C.C.W.H.); 0000-0002-6062-6377 (J.H.T.B.); 0000-0002-1236-4210 (B.D.); 0000-0001-5461-0646 (S.B.F.); 0000-0003-3007-9947 (J.G.G.); 0000-0001-8456-9437 (E.A.H.); 0000-0001-5915-6745 (D.L.L.); 0000-0002-6329-2325 (D.A.L.); 0000-0002-0936-6979 (M.O.); 0000-0002-5619-4145 (G.P.); 0000-0002-6344-4720 (G.K.P.); 0000-0002-0619-5799 (B.M.S.); 0000-0002-3211-6337 (M.T.); 0000-0003-1988-6844 (M.F.V.M.); 0000-0002-8080-7511 (J.C.W.); 0000-0002-8672-0986 (S.R.H.).

You may print one copy of this document at no charge. However, if you require more than one copy, you must place a reprint order. Domestic reprint orders: amy.schriver@sheridan.com; international reprint orders: louisa.mott@springer.com.

Correspondence and requests for reprints should be addressed to Connie C. W. Hsia, M.D., Department of Internal Medicine, Division of Pulmonary and Critical Care Medicine, 5323 Harry Hines Boulevard, Dallas, TX 75390-9034. E-mail: connie.hsia@utsouthwestern.edu.

This article has a data supplement, which is accessible from this issue's table of contents at www.atsjournals.org.

Ann Am Thorac Soc Vol 20, No 2, pp 161–195, Feb 2023
Copyright © 2023 by the American Thoracic Society
DOI: 10.1513/AnnalsATS.202211-915ST
Internet address: www.atsjournals.org

Contents

Overview

Quantitative analysis of functional and structural lung imaging complements traditional visual assessment, playing an important role in enhancing the understanding of physiology and pathophysiology, as well as diagnosis and monitoring of lung disease and treatment response. Structural features such as airway dimensions and branching patterns can be quantified down to the seventh generation, and different approaches, including threshold, histogram, and morphological and textural patterns, can be used to evaluate parenchyma. Functional imaging with computed tomography (CT), positron emission tomography (PET), single-photon emission CT (SPECT), and magnetic resonance imaging (MRI) use endogenous molecules, injected contrast agents, or radioactive isotopes as tracers for measuring changes in airway caliber and mechanical properties, regional ventilation and perfusion distributions, and their spatiotemporal relationships. Processes such as gas diffusion across alveolar septal tissue, through blood, and into capillary red blood cells (RBCs) can be quantified using hyperpolarized gas MRI and used to estimate oxygen transfer. Many of these techniques require expensive equipment and sophisticated computations while hardware and analytical approaches are rapidly advancing. Major challenges in the development and application of imaging metrics include technical and analytical standardization across modalities and platforms, effects of differing lung inflation states, image acquisition, segmentation and measurement techniques, quality of training data, lack of gold standards for validation of imaging-derived measurements, and the need to verify interpretation of imaging-based conclusions against physiological and clinical outcomes. This workshop statement summarizes the principles and approaches for quantifying imaging-based data to yield meaningful physiological insight, their advantages and limitations, and future directions.

Introduction

Innovation in Lung Imaging

Thoracic imaging is a rapidly evolving field with a central role in the diagnosis and monitoring of lung disease, providing insights linking structure to function. Volumetric CT is routinely used to render three-dimensional (3D) maps of lung structures (e.g., individual lobes and the bronchovasculature), and combined with PET to obtain functional data. Beyond routine visual assessment, quantitative imaging (QI) endpoints could be used in clinical trials to identify anatomical and physiological phenotypes (e.g., airway remodeling, progressive emphysema and fibrosis, textural patterns quantifying architectural alterations) (1, 2). Intravenous iodine and dual-energy CT (DECT) are used to separate blood and tissue volumes. In addition to imaging static structure, coregistered landmarks on paired images obtained at different lung volumes are used to infer regional air trapping, lung compliance, and deformation. MRI using ultrashort–echo time (UTE) sequences improves signal detection from lung parenchyma, and contrast agents (e.g., oxygen, hyperpolarized [HP] noble gases) are used to deduce physiological processes (e.g., distributions of ventilation, perfusion, and alveolar diffusion). Proton MRI is used to measure regional perfusion and ventilation-perfusion ratio

Key Conclusions and Recommendations

- Imaging modalities (CT, PET, SPECT, and MRI) offer innovative quantitative information on lung structure and function, including regional air and tissue volumes, airway and vascular dimensions, lung mechanics, regional alveolar ventilation, perfusion, ventilation–perfusion matching, and alveolar–capillary diffusion.
- State-of-the-art imaging and analytical techniques evolve rapidly; assumptions and limitations of each should be clearly stated to avoid misinterpretation of results.
- Lung tissue density is higher in gravitationally dependent than nondependent regions. Lung volume and posture during image acquisition affect tissue, air and blood distributions, physiology, and quantification. Acquisition conditions (e.g., lung volume, breath-hold duration, image resolution, both nominally and functionally) should be documented and standardized when possible and considered in data interpretation.
- Quantitative analysis of imaging data should follow basic principles of unbiased study design and sampling scheme to ensure that each part of the structure or region of interest has equal probability of being sampled. Measurements should be related to a well-defined anatomical or volumetric reference space (e.g., per milliliter of lung or lobar volume) and normative data when appropriate.
- Optimizing the accuracy of landmark segmentation, registration, and automated image analysis protocols are major areas in need of research and validation. Methodology should be clearly described.
- Established guidelines (e.g., for lung densitometry) and characterized reference standards should be followed to maximize reproducibility among sessions, scanners, and modalities.
- Automated exhaustive voxel-by-voxel image analysis increases precision (reproducibility of measurements) but not necessarily accuracy (closeness to the "true" value). High-precision measurements may exacerbate systematic bias and reduce the accuracy of results.
- Care should be taken to select appropriate physiological parameters for correlation with imaging metrics, and the limitations of comparisons should be considered (e.g., between imaging-derived supine end-inspiratory lung volume and upright total lung capacity by plethysmography).
- Gas exchange is determined by *alveolar ventilation* (rate of fresh gas delivery to the alveoli), *diffusion* (rate of gas transfer across the alveolar–capillary–blood barrier), and *perfusion* (rate of blood delivery to pulmonary capillaries). Terminology describing these functions inferred from imaging should be precise to avoid confusion, e.g., specific ventilation with alveolar ventilation, pulmonary blood volume with perfusion.
- Functional lung imaging remains emergent. Many techniques lack rigorous validation or gold standards. There is a need for more studies using robust animal models of disease to directly validate conclusions on the basis of *in vivo* imaging against quantitative structural analysis.
- Computational models of physiological processes, grounded in the laws of physics, may be combined with imaging metrics to aid the prediction, validation, and mechanistic interpretation linking the imaged findings to function.

($\dot{V}_A/\dot{Q}$) without injected contrast, while ^{13}N-nitrogen PET provides dynamic data on physiological processes, yielding novel insights into physiological and pathophysiological mechanisms.

Challenges

Advances in QI are crucially dependent on technology and computational power. Massive data sets are run through "black box" algorithms, distilled into selected "biomarkers" that may be correlated with global function, e.g., forced vital capacity (FVC), 6-minute-walk distance, or findings on biopsy samples, to evaluate their ability to detect, stratify, and monitor lung disease. Numerous imaging modalities, manufacturers, platforms, and algorithms may not integrate smoothly (3, 4). Emergent QI metrics vary among centers in the methods of acquisition, quantification, interpretation, and extrapolation; all involve assumptions of how the imaged structures relate to function.

Technological advances contribute to difficulty in standardization. In addition, the use of medical jargon makes it difficult for the less initiated to evaluate the potential and limitations of QI-derived metrics. Systematic errors may arise at each step (Table 1) of image acquisition, processing, and analysis, including *1*) technical issues (e.g., depth of inspiration, acquisition protocol, signal-to-noise ratio, resolution); *2*) nonrepresentative sampling of parts of interest (e.g., comparing regions, lobes, or airways); *3*) lack of a well-defined reference space (e.g., lobe volume); *4*) inaccurate landmark coregistration for evaluating paired images obtained at different lung volumes; and *5*) failure to consider basic physiology and/or biological or spatiotemporal heterogeneity (e.g., anatomical or gravitational gradients, respiratory cycles, nonuniform disease, or mixed pathology such as coexisting emphysema and fibrosis). Tables 1 and 2 summarize the basic steps in lung imaging and analysis with examples, caveats, and practice principles.

The lung deforms under its own weight, much like a vertically stretched Slinky® spring (5). Lung tissue density is higher in gravitationally dependent than nondependent regions, as alveolar size at resting volume is smaller (6–10) except at total lung capacity (TLC); standardizing lung volume at acquisition is important. In addition to ghravitationally based hydrostatic gradients, variation in alveolar size also creates apparent perfusion gradients because capillaries within alveolar walls are closer

Table 1. Steps and considerations in imaging the lung, examples, and practical principles

Imaging and Analytical Steps	Examples	Practical Principles and Caveats
Optimize image acquisition	End-inspiration vs. end-expiration, supine vs. prone, before or after bronchodilator treatment	Standardize when possible
Highlight structures of interest	Use of contrast agents, spin states, or exogenous tracers	Describe methodology in detail
Delineate structures of interest on images	Segmentation, landmark registration and coregistration, image warping	Algorithms are available in the public domain
Filter images	Reduce noise, sharpen edges, and enhance selected features	Avoid overfiltration, which may introduce distortion or bias
Measure attenuation/density/signal intensity/rate of signal change	Compare global or regional histograms. Select threshold values. Look for architectural patterns.	Discrete threshold values may not fully describe a continuum of changes
Select and measure imaged structures (e.g., airway, blood vessels, parenchyma)	Determine quality, quantity (e.g., number, length, diameter, volume), and their distribution. Compare groups at global, stratified, or regional level.	Include measures of heterogeneity (e.g., coefficient of variation or error)
Distill data into selected "imaging biomarkers"	For example, LAA, fSAD, Pi10, VDP	Different metrics are at varying stages of standardization and validation. Vendor-specific algorithms may not fully harmonize with one another despite each being validated
Incorporate relevant assumptions and models to infer function	Rates of gas or blood delivery, conductance or uptake	Examine whether assumptions are free of bias and have been rigorously validated
Establish reproducibility of biomarkers	Repeated measures across platforms, subjects, and time	Examine factors causing variability
Validate imaging biomarkers against existing standards depending on modality	Compared with, for example, lung water gravimetry, microparticle deposition, multiple-breath gas washout, multiple–inert gas elimination technique	Examine limitations of existing standards to ensure proper use
Correlate imaging biomarkers with regional and global structural and functional indices	For example, postmortem morphometry in animal models, surgical or biopsy specimens, physiological tests and standards	Ensure correlation with the comparable/equivalent parameters
Assess predictive value of imaging biomarkers	Monitor serial changes across time, pathological conditions, or before and after intervention	May require multicenter trials

Definition of abbreviations: fSAD = region of functional small airway disease; LAA = low attenuation area; Pi10 = wall thickness of airways with inner perimeter of 10 mm; VDP = ventilation defect percentage.

together in dependent lung, which will vary with lung volume (11). Variation in alveolar size also creates gradients in regional alveolar ventilation ($\dot{V}_A$) and fresh gas delivery to the alveolar space because alveoli in nondependent regions expand less for a given change in pressure and are less well ventilated. These deformable properties of the lung also vary with posture (6–8, 10, 12, 13). The wedge shape of the lung means that more lung volume lies in the dependent third in supine posture than prone posture (13, 14), thus affecting gravitational deformation. The lung matches shape with the thorax, resulting in greater expansion of nondependent lung while supine, compared with dependent lung (14). Lung volumes measured by spirometry also vary with posture (15, 16), thereby complicating comparisons of imaging data obtained supine with those obtained prone or on upright pulmonary function tests.

Overcoming these challenges is critical to ensuring that *1*) imaging metric derivation is accurate and reproducible and *2*) measurements accurately represent (patho)physiology to guard against misinterpretation of results in all QI applications irrespective of modalities or disease entities.

Goal and Significance

This American Thoracic Society (ATS)–Fleischner Society workshop aims to promote unbiased quantification and physiologically accurate interpretation of *in vivo* imaging results to enhance understanding of pulmonary structure–function relationships and to compare what are believed to be comparable metrics obtained using different imaging modalities. Addressing the challenges of QI metrics has a high physiological and clinical impact because these imaging modalities are not risk free. CT and PET involve radiation exposure, especially when specialized protocols (e.g., inspiration–expiration, pre- and postcontrast) are used. MRI may be time consuming and cumbersome. Contrast injections may cause adverse reactions or impair renal function. Advanced imaging and analysis require sophisticated equipment, infrastructure, and manual steps or edits that substantially increase the financial burden of

Table 2. Common sources of systematic errors in imaging and analysis

Type of Error	Examples of Error
Technical issues during acquisition	Differences in hardware and software, acquisition protocol, signal-to-noise ratio, and resolution Differences in posture (supine, prone) and lung volume (full inspiration or expiration) Motion artifacts
Biased sampling of structure for analysis	Not spatially randomized Not representative of the whole lung Comparison of mismatched airways (e.g., from different hierarchical locations)
Failure to define an appropriate reference space	Expressing results only as a ratio of two quantities without the absolute volume of the lung, lobe, or region of interest
Issues with segmentation or registration	Inaccurate identification of landmarks Landmarks have been altered by disease or are congenitally absent Inability to resolve distal structures (e.g., capillaries from venules on CT, intraacinar airways on micro-CT)
Inaccurate assumptions or simplifications	Assuming alveolar airspaces are spheres Ignoring postural differences (e.g., between supine imaging and upright lung function tests) Assuming blood contained in large vessels represents local perfusion
Failure to consider spatiotemporal and biological heterogeneity	Anatomical or gravitational gradients in tissue density, ventilation, and perfusion Variations in respiratory or cardiac cycles Nonuniform or mixed pathology

Definition of abbreviation: CT = computed tomography.

health care. It is imperative that the fundamental challenges be systematically addressed to facilitate meaningful advances.

Methods

A multidisciplinary panel of thoracic imaging, pulmonary medicine, physiology, pathology, stereology, bioengineering, and biophysics experts was convened to examine the *1*) accuracy of major current QI biomarkers derived from CT, PET, and MRI in representing underlying structure and physiology; *2*) caveats in methodology, interpretation, and extrapolation of QI biomarkers to structure–function endpoints; and *3*) key knowledge gaps for validation and further exploration. Participants reviewed the literature and focused on QI metrics used to infer major pulmonary structural and physiological processes: volume partition, attenuation-based parenchymal and bronchovascular analysis, mechanics ventilation, perfusion, ventilation–perfusion matching, and diffusion. Emerging technology and applications (17, 18) were discussed. General principles for accurate quantification are emphasized for all modalities and diffuse lung diseases irrespective of specific diagnoses. For each modality, the committee reviewed current QI metrics in terms of accuracy, precision and reproducibility, assumptions, limitations, validation against independent structural or functional measures, and how QI metrics could be incorporated into biophysical models to predict lung function. Discussion facilitated consensus on current capabilities, limitations, and future directions. Findings were synthesized into this report. Although specific guidelines are not part of this report, general "good practice" approaches for developing and evaluating emergent metrics are outlined (Table 1).

Lung nodule analysis, covered separately by both the ATS and the Fleischner Society, is not included. The nascent field of artificial intelligence (AI) or machine learning (ML) is beyond the scope of the present report (*see* Reference 19 for further information); some AI algorithms are publicly available. The committee believes that a robust understanding of good practice principles and the assumptions and limitations of QI metrics are prerequisites for the successful development and application of AI and ML to image quantification. Potential conflicts of interest were disclosed and managed in accordance with ATS policies. Workshop participants with relevant industry-funded research participated in the discussion and writing but were recused from comparing the imaging or analysis methods with others in the relevant sections of the report.

Stereological Principles in Quantitative Image Analysis and Basic Measurements

Stereology is the statistical science that forms the basis of a set of practical methods (*see* below) for extracting accurate and precise quantitative structural information from imaging data sets of irregular objects. Stereological methods make no assumptions regarding shape, size, orientation, or spatial distribution of objects and are unbiased by design instead of relying on geometric model assumptions (e.g., assuming that alveolar airspaces are spheres) that may introduce bias. Stereology is the method of choice for quantifying lung structure in microscopy, for which standards, principles, and practical applications have been rigorously defined (20–25). The same principles apply to CT, micro-CT, PET, MRI, and other modalities ("*in vivo* morphometry") (26), used in the brain (27–30), heart (31), and lung (26, 32, 33), among other organs.

Optimizing Accuracy and Precision

In a quantitative data set, "accuracy" refers to the closeness of the data to the true value and depends on both sensitivity and specificity (34) that is, accuracy = number of (true-negative + true-positive)/(all negative + all positive)

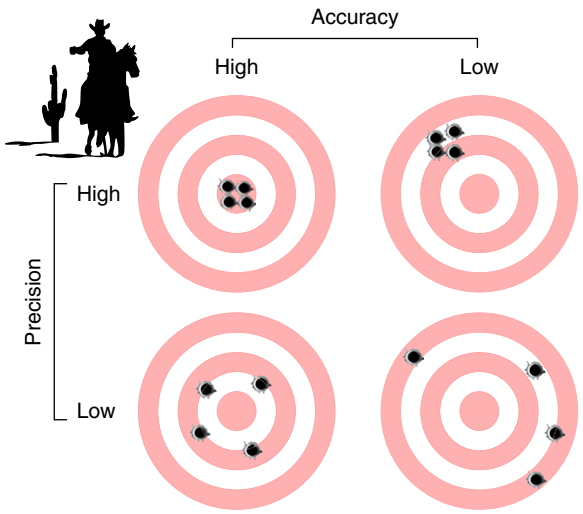

Figure 1. Precision, bias, and quality of study design. In an ideal study design (left upper target), there is no bias, and the measurements (solid dots) cluster tightly (high precision) in and around the target "true value" (high accuracy). In a less optimal design (left lower target), precision is lower but without bias, as the measurements scatter near the target. In a poor study design (right upper target), highly precise but biased measurements ensure that the target will never be hit. In another poor study design (right lower target), bias combined with low precision allows a small possibility of hitting the target. Therefore, more measurements do not increase accuracy if bias exists at higher levels of study design (e.g., sampling of structures or regions, or intersubject heterogeneity). Automated exhaustive measurements could aggravate inaccuracy and reduce efficiency because of the time and effort required to achieve a given coefficient of error (the "do more less well" principle) (25, 36, 37). Adapted by permission from Reference 35.

measurements. "Bias" refers to systematic errors leading to inaccuracy, such as improper sample selection, assumptions that systematically deviate from reality, incomplete visualization of the structures of interest, or overprojection. "Precision" refers to measurement reproducibility and depends mainly on sampling design and size and distribution of the sample (35). Bias can be neither detected in the data nor decreased by making more measurements and is avoided *a priori* only by rigorous study design and using unbiased methods throughout the study. In contrast, precision can be checked and, if necessary, adjusted by increasing the sample size or number of measurements. It is more efficient to invest extra effort into the higher levels of study design (e.g., more subjects per study group, more regions of interest per subject) than the lower levels (e.g., more voxels per field of view), because the former more robustly addresses interindividual and intraindividual variability. Smart data are more efficient than big data. By applying unbiased sampling techniques, it is not always necessary to exhaustively analyze each voxel (the "do more less well" principle) (25, 36, 37). In a well-designed study, precision is tuned such that the coefficient of error within subjects ("noise") is significantly smaller than that between subjects (biological variation) within a study group ("signal"); exhaustive measurements to further increase precision beyond this point are inefficient because of the extra time and effort required (37) and may amplify systematic errors (Figure 1). However, repetitive imaging can often be made to assess response to intervention. Baseline between-subject variability becomes less important in longitudinal studies in which subjects act as their own controls.

Only Unbiased Sampling Can Yield Unbiased Data

The practical stereological methods are sampling and measurement. Unbiased sampling designs guarantee statistically representative samples and generally must be spatially randomized (each part of the structure of interest has equal probability of being sampled). For anisotropic lung structures (airways and vessels), some parameters (surface area, length) also require spatial orientation randomization. Specific sampling designs have been developed for different purposes, such as systematic uniform random sampling for global assessment, isotropic uniform random sampling for randomization of orientation (e.g., surface area of conducting airways), stratified sampling for targeting subcompartments defined by anatomy (e.g., lobes) or pathology (e.g., normal vs. diseased regions), fractionator sampling for estimation of particle numbers independent of tissue deformation (e.g., alveoli), and proportionator sampling for weighted sampling with known probability according to defined tissue characteristics (e.g., marker-labeled regions) (20, 35, 38, 39). Voxel-by-voxel automated image analysis ensures neither accuracy nor precision of the results, nor does it obviate the need to strictly follow stereological sampling principles. Systematic sampling of micro-CT images has been used to explore differences between surface and core alveoli in mouse lung (32) and to correlate *ex vivo* imaged small airway gas trapping to *in vivo* lung tissue measurements in chronic obstructive pulmonary disease (COPD) to characterize terminal bronchiole loss, narrowing, and obstruction (33).

Basic Stereological Measurements

First-order parameters are volume (three-dimensional [3D]), surface (two-dimensional [2D]), length (one-dimensional [1D]), and number (zero-dimensional [0D]). Measurements are performed using geometric test probes, such as points (0D), lines (1D), planes (2D), or volumes (3D). The probes interact with the imaged pixels or voxels, creating "events" that can be counted. Raw counts provide ratios (volume, surface, length, and number densities) that are multiplied by the reference space volume to obtain absolute measures for the lung or subcompartment.

Defining the Reference Space

It is crucial to define and measure a biologically meaningful reference space (e.g., volume of the lung or lobe) as the starting point for analysis and endpoint for data reporting. Measurements expressed only as ratios (e.g., "number per unit volume") are subject to the "reference trap," whereby a change in the ratio can be due to a change in the numerator, the denominator, or both, leading to interpretive ambiguity (40). An efficient way of measuring volume, point counting (41), is used to quantify acinar components by micro-CT (42, 43) and extrapulmonary organ volume by CT (44, 45), a forerunner of voxel-by-voxel summation of the volume of the imaged structure.

Assessing Heterogeneity with Stereology

Object size may be expressed as a number- or volume-weighted mean volume. When both number- and volume-weighted volumes are known, an object's size distribution can be estimated. Spatial distribution of objects in subcompartments within a reference space may be expressed by a "relative labeling index," that is, (observed number of objects per subcompartment)/(expected number of objects per subcompartment if randomly distributed) (46). Stereology has been applied to quantify acinar structures by HP gas MRI combined with modeling of alveolar gas diffusion to infer regional gas exchange and its heterogeneity in normal and pathological states (26).

Assessing Lung Parenchyma

CT Attenuation

CT lung attenuation (measured in Hounsfield units [HU]) of a voxel comprises air, tissue, and blood and is extensively used in assessing emphysema, air trapping, fibrosis, and infiltrative conditions (47) (Table 3). Interscanner variability in calibration, radiation dose, acquisition and reconstruction protocol, lung mask, and other parameters affects comparisons across platforms and institutions and may be minimized by frequent calibrations of air and water and by using lung-specific phantoms to ensure measurement consistency (48). The QIBA (Quantitative Imaging Biomarkers Alliance) has published a detailed profile for lung densitometry with standardized protocols to minimize these issues (49).

Volume Measurement

Segmentation of lungs from other structures allows calculation of lung volumes (50). Lung volumes measured using physiological methods typically refer to gas volume, while conventional CT attenuation–derived "anatomical" lung volume also includes tissue volume and, presumably, microvascular blood in vessels below the limits of CT resolution. Lobes may be segmented on the basis of bronchial and fissure anatomy (51). Total lung or lobe volume may be partitioned into air and air-free "tissue" volumes (10, 52); the latter includes microvascular blood volume (53–56).

Lung segmentation algorithms vary in their inclusion of central vasculature, resulting in differences in volume measurement (57). The QIBA protocol provides a basis for standardizing the software for these metrics (49). Incomplete or partially obliterated fissures could impede lobar segmentation. Approaches combining bronchial and fissure anatomy with deep learning can minimize errors (58, 59).

Parenchymal attenuation varies with lung volume (10). CT images are typically acquired at end-inspiration or end-expiration, with potential variations in transpulmonary pressure at a given lung volume, thereby introducing variability in results. Submaximal inspiration leads to underestimation of pulmonary emphysema; both lung inflation and tissue loss influence CT densitometry (60). Although measuring transpulmonary pressure is impractical in most studies, it is imperative to recognize errors caused by lung volume variations and train the subject with detailed breathing instructions (48, 49). Spirometric gating facilitates a consistent lung volume but is often impractical for large multicenter studies (61–64). For longitudinal studies, density metrics may need to be adjusted for lung volume. Progressive emphysema or fibrosis will itself change lung volume. Alternatively, lung volume may be included as a covariate in multivariate analysis.

The attenuation of air is −1,000 HU, and that of water is 0 HU (65). Tissue is a composite of materials (blood, protein, fat)

Table 3. Types of quantitative computed tomography analysis in diffuse lung disease

	Examples	Utility
First-order metrics	Attenuation histogram Mean Median Skew Kurtosis (peakness) Threshold (low or high attenuation) Matched images at different lung volumes for PRM or DPM techniques	Summarize statistics of attenuation distribution for whole lung or ROIs Calculate lung or lobar volumes and regional tissue density (fractional tissue volume) Assess absolute or percentage of low- or high-attenuation volumes Distinguish among air trapping, obliteration of alveoli, and parenchymal abnormalities
Higher order metrics	Fractal dimensions Run-on matrices Gray-level co-occurrence matrices	Texture analysis Reticular infiltrate Consolidation Ground-glass opacity Honeycombing Traction bronchiectasis Describe spatial relationships among features
	Model based (supervised and/or unsupervised machine learning algorithms)	Optimize (semi)automatic detection and classification of anatomical features Detailed comparisons among ROIs within and among subjects Use complex mathematical and statistical models
Specific structures	Airways Conducting blood vessels	Measure dimensions (e.g., diameter, cross-sectional area, length, wall thickness) Describe branching patterns (e.g., angles, symmetry) and spatial relationships

Definition of abbreviations: DPM = disease probability measure; PRM = parametric response mapping; ROI = region of interest.

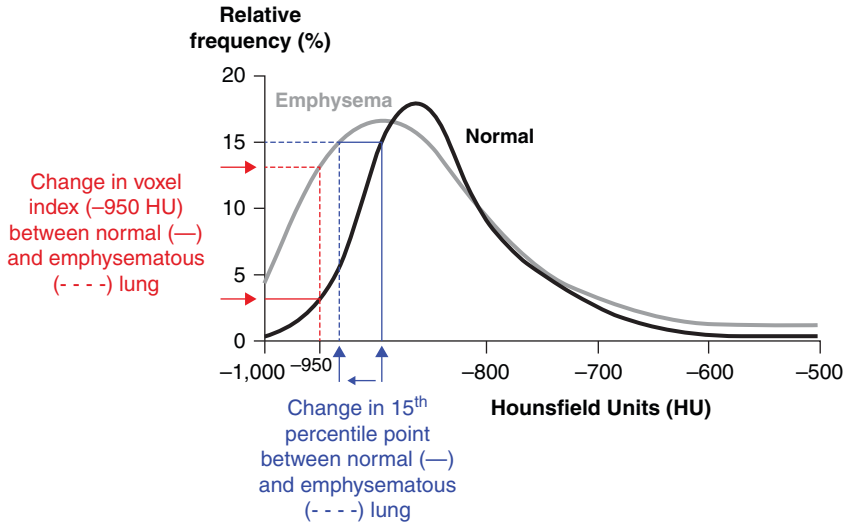

Figure 2. Attenuation histograms in normal lung and in emphysema and the derivation of densitometry indices. In this example, the 15th percentile point (in Hounsfield units [HU]) is defined as the cutoff value below which 15% of voxels with the lowest density are distributed. The voxel index at a threshold of −950 HU is shown and defined as the percentage of voxels with values less than −950 HU. Adapted by permission from Reference 368.

with nonzero attenuation. Variability in tissue attenuation can arise from fluctuations in regional perfusion, blood volume, and extravascular compartments. High-attenuation regions (66) may reflect atelectasis, blood, fluid, cells, or fibrosis. CT-derived lung tissue volume overestimates anatomical extravascular lung tissue volume (55) and correlates poorly with *in vivo* alveolar gas-exchanging tissue (including microvascular blood) volume measured using physiological methods at a similar mean transpulmonary pressure; discrepancy remains even after subtracting pulmonary blood volume (PBV) and may be due partly to residual blood within microvessels below the CT resolution limit (<1 mm) (56). These sources of attenuation changes contribute to variability in CT-based metrics for assessing the tissue compartment. Some differentiation of blood from extravascular tissue is possible through the use of intravenous contrast agent or DECT (67, 68). Four-dimensional dynamic CT (69) permits the quantification of regional tissue nonlinearity and hysteresis (reflecting difference between inspiratory and expiratory lung compliance), although at a lower resolution and higher radiation exposure. MRI also provides dynamic imaging, but with lower resolution, relatively lower air/tissue contrast, and fewer standardized metrics.

First-order CT-derived metrics based on volume and the attenuation histogram provide statistical summaries for regions of interest. Selected attenuation thresholds have been adopted to quantify low- and high-attenuation parenchymal volumes as reflecting alveolar obliteration and/or small airway obstruction and parenchymal inflammation and fibrosis, respectively. The mean lung attenuation with or without spirometry gating (70) and absolute or fractional lung volume below selected attenuation thresholds at full inspiration (e.g., −910 HU [71], −950 HU [72, 73], and −960 or −970 HU [74]), or the lowest 15th percentile of attenuation histogram (75), have been used to index terminal air space enlargement and/or alveolar obliteration in emphysema (Figure 2). As both radiation dose and reconstruction algorithm affect densitometry results, threshold selection should be adapted to local protocol (76). CT-derived total lung volume (TLV) may be statistically adjusted to a "predicted" physiological TLC (77–79) or the log(TLV) analyzed as a covariate (79).

Caveats: Formal guidelines are lacking for the selection of pulmonary function tests in validating QI metrics. Nonetheless, there are strong correlations between CT-derived TLV and plethysmographic TLC in a normal patient population (80) and in individuals with idiopathic pulmonary fibrosis (81). CT-derived indices also correlate robustly with expiratory subcompartments (e.g., functional residual capacity, residual volume, residual volume/TLC) in representing gas trapping in small airway disease (82, 83). In COPD, measures from inspiratory CT (e.g., low-attenuation area ⩽ −950 HU) show larger discrepancies against spirometry than plethysmography and in predicting spirometry as COPD severity increases (84), whereas measures from expiratory CT (e.g., low-attenuation area ⩽ −856 HU) correlate with spirometry in smokers (85). In COPD, TLC by plethysmography is significantly larger than that by end-inspiratory high-resolution CT (86, 87); discrepancy correlates with air trapping and hyperinflation, possibly reflecting a postural difference between modalities and/or plethysmographic underestimation of alveolar pressure as airway resistance increases (88, 89).

Improving the accuracy of segmentation, landmark registration, and automated image analysis is under active research. Advanced imaging techniques and analysis are often at early developmental stages and not rigorously validated. Vendor-specific algorithms may provide metrics incongruent with one another regardless of separate validation of each.

Small Airway Disease

Pathology of small conducting airways (⩽2 mm in diameter) may be detected on CT images as mosaicism (heterogeneous parenchymal attenuation on inspiratory CT), air trapping (expiratory CT), ground-glass opacities, centrilobular nodules, tree-in-bud opacities, and subsegmental atelectasis (90, 91). To quantify air trapping, paired inspiratory/expiratory CT may be aligned for landmark coregistration. Individual voxels are classified as low attenuation, functional small airway disease (fSAD), or normal using either fixed attenuation thresholds (parametric response mapping [PRM]) (92–99) or continuous distributions of volume-dependent attenuation changes (disease probability measure [DPM]) (92, 100). Air-trapped regions on expiration, without voxels classified as low attenuation on inspiration, indicate fSAD with normal attenuation on inspiration but reduced absolute attenuation on expiration (PRM) or relative attenuation changes with lung volume changes (DPM). fSAD from either method correlates with multivariate lung function endpoints (95–98, 100). DPM and PRM yield consistent results in normal subjects. In subjects with COPD, DPM

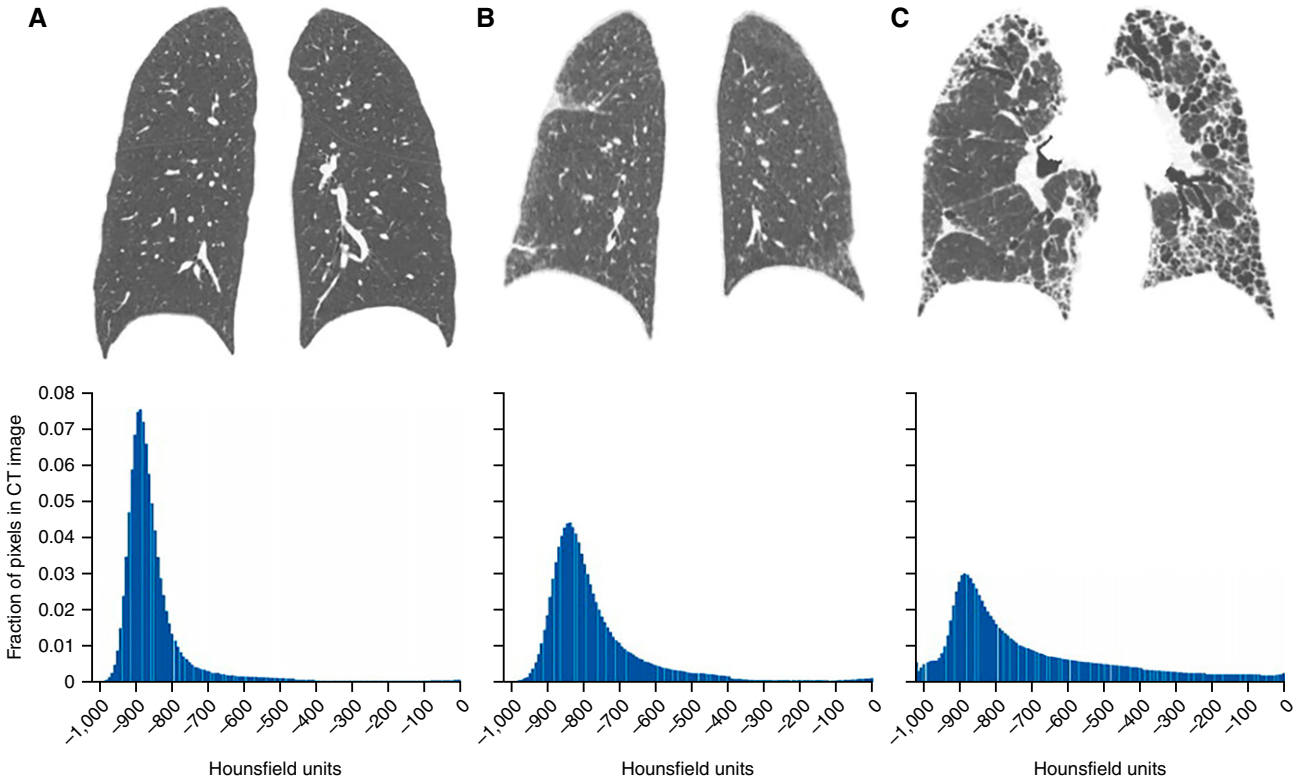

Figure 3. (*A–C*) Coronal computed tomography (CT) reconstructions and corresponding CT histograms from (*A*) a healthy individual, (*B*) a patient with mild lung fibrosis, and (*C*) a patient with advanced lung fibrosis. In the healthy individual with no lung fibrosis, the CT histogram is sharply peaked and skewed to the left compared with a Gaussian normal distribution. In the patient with mild fibrosis, the curve is less peaked (less kurtotic) and less skewed. This tendency is even more substantial in the patient with advanced lung fibrosis. Reproduced by permission from Reference 101.

classifies more voxels as emphysematous and gas trapped than PRM and may be less influenced by scanner or respiratory effort variability (92, 100). Compared with multibreath nitrogen washout testing and airway oscillometry, both PRM and DPM correlate with airway resistance and reactance; DPM correlations are slightly stronger. Emphysema (%) for both correlates best with multibreath nitrogen washout measure of acinar airway inhomogeneity (100). The practical significance of the differences between DPM and PRM remains unclear; more comparisons are needed.

Caveats: Image coregistration requires reliable tracking of landmarks; the accuracy of landmark identification is usually impossible to validate. Landmarks may be affected by disease (e.g., fissures for tracking lobar volume may be obliterated in advanced COPD or interstitial lung disease [ILD] or congenitally incomplete or absent).

Interstitial Lung Disease (ILD)

Thin-section CT is the standard method for imaging ILD subtypes, severity of infiltrates, inflammation, injury, or fibrosis and monitoring progression and therapy. Subtle parenchymal changes in subclinical or regional ILD can be quantified from whole-lung attenuation histograms (Figure 3). Architectural distortion and regional heterogeneity in reticular infiltration, ground-glass opacity, or consolidation may be captured using texture-based metrics (101) (Table 3). Common metrics include the fractional volume of high attenuation (e.g., between −600 and 250 HU) (102) and reticular/honeycomb abnormalities (103, 104). In addition, regional tissue density calculated from the attenuation difference between intrathoracic air and air-free tissue, its coefficient of variation (54), and the skewness and kurtosis of attenuation histogram (54, 101) can be used to assess local or global heterogeneity of attenuation, discern divergent patterns between emphysema and ILD progression (Figure 4), and detect subclinical abnormalities in kindred with telomerase mutations predisposing to pulmonary fibrosis (105).

Caveats: Current smoking status increases baseline lung attenuation independent of underlying pathology (77). A change in smoking status could affect the measurement and interpretation of changes in lung attenuation. Selection and validation of approaches remain empirical.

Textural Metrics

Measurement of attenuation alone provides insufficient information. Textural metrics characterize the 3D architecture of and relationships among airspaces, lung tissue, and bronchovasculature (106–112). Emerging techniques incorporate imaging data into machine learning and statistical models to classify disease types and severity, with optimization algorithms that iteratively refine model predictions. The optimized models undergo clinical/physiological validation against an external unlabeled data

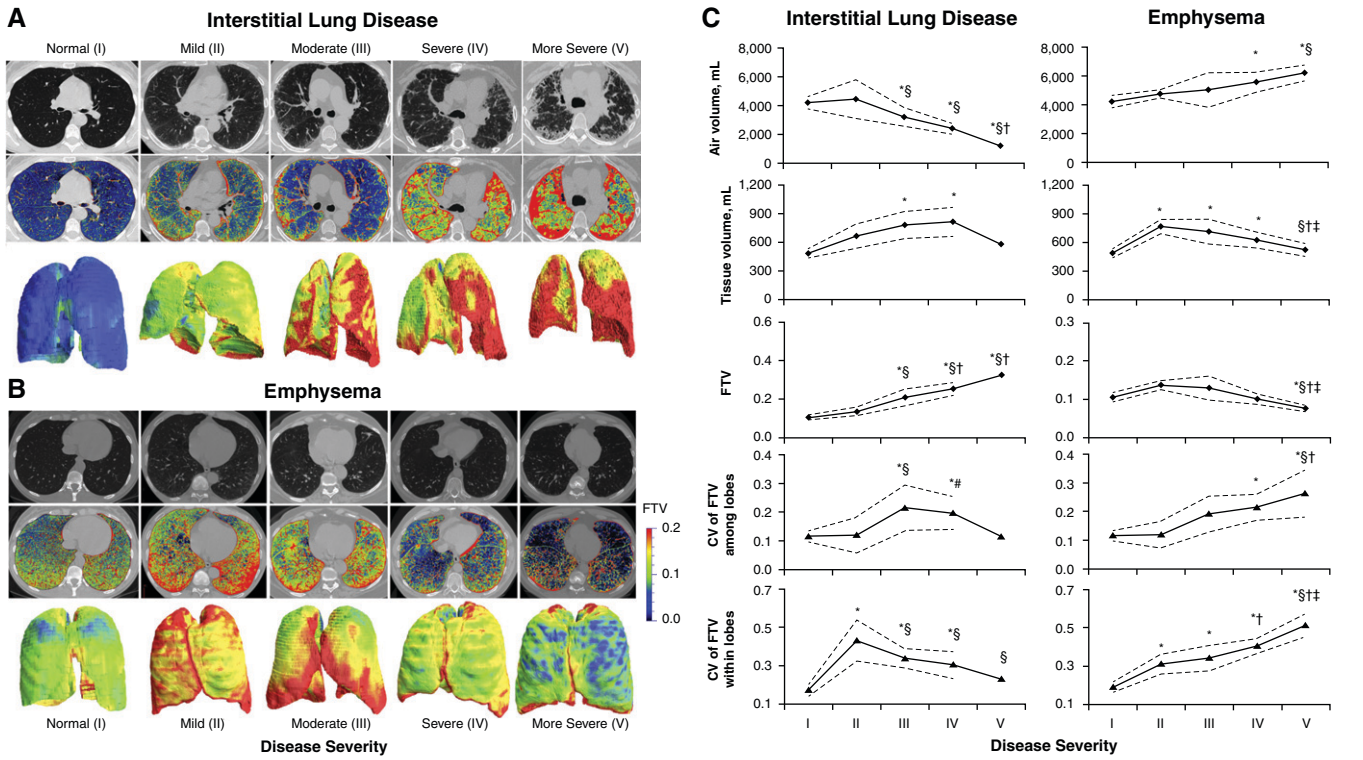

Figure 4. (*A* and *B*) Computed tomography (CT) quantification of disease severity in patients with (*A*) interstitial lung disease (ILD) (idiopathic pulmonary fibrosis) or (*B*) emphysema. In *A* and *B*, CT images (upper row), fractional tissue volume (FTV) color maps (middle row), and three-dimensional renderings (lower row) are shown for representative patients with different degrees of disease severity. (*C*) Side-by-side comparison between ILD and emphysema for whole-lung air volume, tissue volume, FTV, and CV of FTV among and within the lobes at prone end-inspiration. Data are mean ± 95% confidence interval. ILD severity was classified according to forced vital capacity (percentage predicted) as mild (stage II, ⩾80%), moderate (stage III, 50–80%), severe (stage IV, 30–50%), or more severe (stage V, <30%). Emphysema severity was classified according to forced expiratory volume in 1 second (percentage predicted) as mild (stage II, >75%), moderate (stage III, 51–75%), severe (stage IV, 21–50%), or more severe (stage V, ⩽20%). $^{*}P < 0.05$ versus stage I (normal), $^{\S}P < 0.05$ and $^{\#}P = 0.06$ versus stage II (mild), $^{\dagger}P < 0.05$ versus stage III (moderate), and $^{\ddagger}P < 0.05$ versus stage IV (severe) by analysis of variance. Reproduced by permission from References 53 and 54. CV = coefficient of variation.

set (104, 107, 113, 114). These approaches (Table 3) seek to standardize the classification of overlapping heterogeneous disease phenotypes and validate the utility of computational and statistical models for predicting outcome (93, 112).

Caveats: Algorithms for textural analysis rely on expert training and a fixed or a mixture of imaging protocols that may not be transferable to other cohorts that use a different mix of protocols and scanners. Standardization of proprietary image reconstruction algorithms poses challenges in multicenter investigations regardless of individual validation. Vendor-based differences in image generation and analysis must be accounted for, often handled as a statistical model in which covariates include the scanner and/or analysis source.

Figure 5 presents a composite of CT-based methods for assessing lung structure from which inferences about lung function may be made.

Assessing Lung Parenchyma: MRI-Derived Metrics

Conventional ^{1}H MRI measures tissue signal intensity using short–echo time and UTE methods (115–117) but with longer acquisition times and lower spatial resolution than CT (comparisons are provided in Table 4). MRI is advantageous when radiation exposure is to be avoided or iodinated contrast is contraindicated (e.g., in pediatrics, pregnancy, or serial assessment of disease progression). Inhalation of an HP noble gas with MRI provides spatial information about ventilation and perfusion heterogeneity with higher resolution than PET and nuclear imaging techniques, with unique capabilities for measuring alveolar–capillary gas diffusion and lung microstructure.

In hyperpolarization, nuclear spins of gas atoms are aligned in a small magnetic field outside of the scanner (118). When inhaled, spatial distribution of the magnetized exogenous gas can be tracked using specialized receiver coils. The first report of ^{129}Xe MRI in a mouse heart–lung preparation (119) was followed by patient studies using HP ^{3}He. Hyperpolarization enhances ^{129}Xe and ^{3}He MRI signal by $\sim 10^{5}$. The subject inhales up to 1 L of gas (for adults) from functional residual capacity, and scanning occurs during a breath hold (5–15 s). The doses (mixed with nitrogen) typically contain no oxygen, as it shortens the ~1-hour "half-life" of

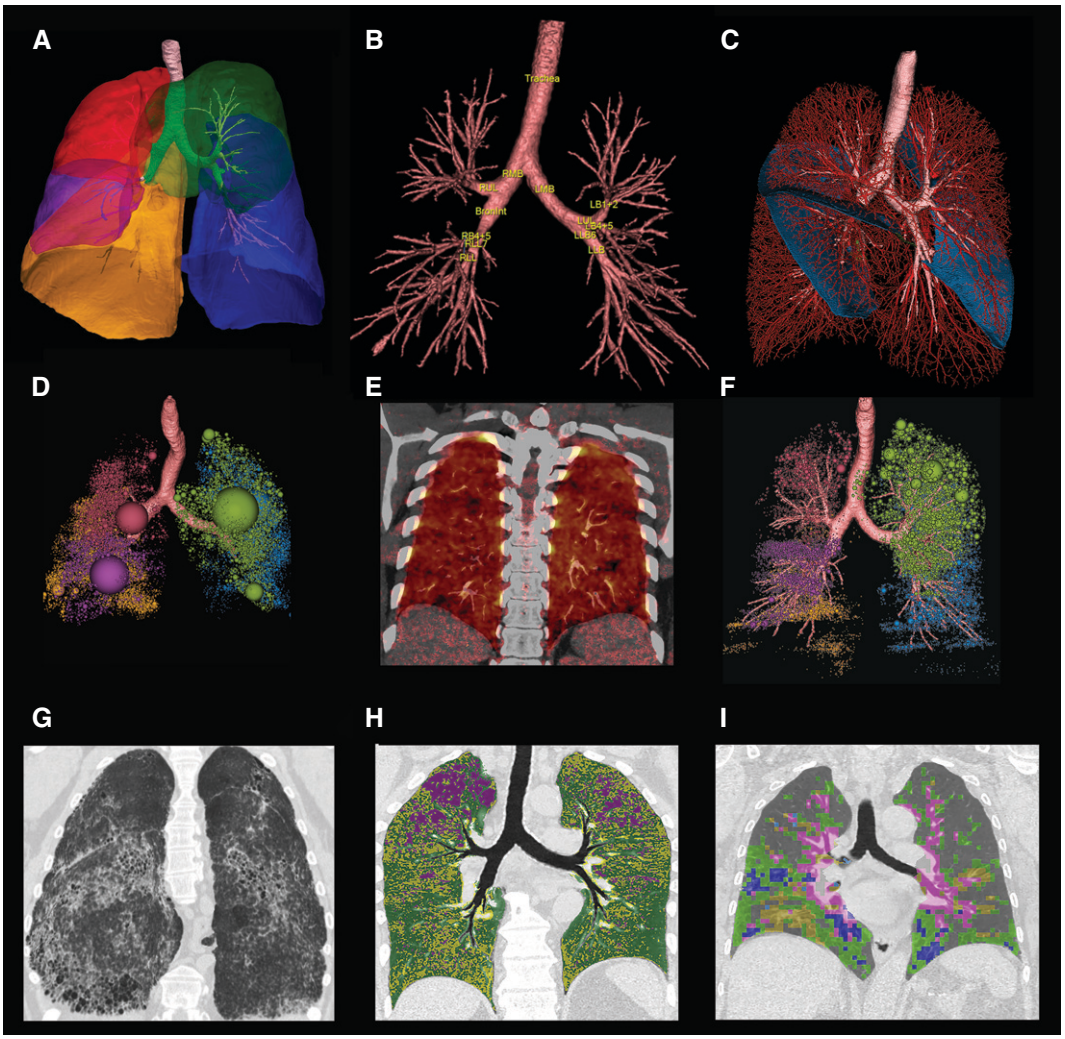

Figure 5. Composite of methods using computed tomography (CT) to visualize and assess lung structure and function. (*A*) Segmentation of whole lung, left and right lung, and individual lobes down to the sublobar segments, as described in Reference 369. (*B*) Airway segmentation with automated naming down to the sublobar segment. (*C*) Segmentation of pulmonary vascular tree with lobar fissures. Fissure completeness report is important for endobronchial lung volume reduction approaches in chronic obstructive pulmonary disease. (*D*) Voxels <-856 Hounsfield units (HU) at residual volume (or functional residual capacity) have been designated as air trapped. Spheres showing regions of air trapping concentration are color coded for lobar location. (*E*) Heated object map of pulmonary blood volume distribution derived using dual-energy CT (47-year-old female smoker). (*F*) Voxels below -950 HU at total lung capacity (spheres) are designated as "emphysema-like." (*G*) Subpleural view. First, the isosurface 2 mm beneath the pleural surface (i.e., lung mask boundary) is computed. A subpleural rendering uses the posterior-facing portion of the lung isosurface to orthogonally project the density values and render the final topographic multiplanar reformatted (tMPR) image (patient with idiopathic pulmonary fibrosis). (*H*) Through matched inspiratory and expiratory images, the ventilation defect probability map demonstrates regions of functional small airway disease (yellow), emphysema (purple), and normal lung (green) mapped onto a tMPR image in which the airways and their associated parenchyma are projected onto a flat surface. (*I*) Adaptive multiple feature method–defined texture map (370) of ground-glass opacities (green), ground-glass reticular (blue), honeycombing (yellow), emphysema (light blue), bronchovascular (pink), and normal (gray) (patient with interstitial pulmonary fibrosis). Courtesy of E.A. Hoffman.

hyperpolarization (120). Supplemental oxygen is administered before and after scanning as required.

Using inhaled HP ^{3}He or ^{129}Xe, subvoxel resolution ($\sim$300 μm) measurements can be made (121–124) that exploit the Brownian motion of these gases and the restriction to gas movement by alveolar walls and terminal airspaces (125). MRI-derived apparent diffusion coefficients (126) are highly sensitive to airspace enlargement and alveolar recruitment (127), may be abnormal in the absence of CT and/or spirometric abnormalities (128), and correlate highly with histology (122–124, 129–131).

MRI has also been used to quantify lung cancer (132, 133). Conventional ^{1}H MRI is useful in differentiating inflammation from fibrosis (134, 135). Alveolitis presents as high signal intensity on T2-weighted sequences and early enhancement on contrast-enhanced magnetic resonance (MR) sequences, whereas fibrotic lesions present as low signal with late

Table 4. Comparison of magnetic resonance imaging and computed tomography in the assessment of diffuse lung disease (emphysema, interstitial lung disease, acute respiratory distress syndrome)

	Strengths	Limitations
CT	Rapid (<10 s) acquisition High spatial resolution Excellent contrast among emphysema, normal lung, and fibrotic lung Can quantify regional structural features down to 1–2 mm	Exposure to ionizing radiation Most acquisitions provide structural rather than functional information
MRI	Sensitive to many aspects of function Sensitive to alveolar geometry (*in vivo* morphometry) Estimates acinar airspace size and alveolar wall thickness Can evaluate perfusion and gas diffusion	May require specialized hardware More complex image analysis UTE sequence requires signal averaging Structural imaging generally lower resolution than CT Low proton density of aerated lung tissue Air–tissue interfaces degrade MR signal properties and reduce SNR Long acquisition time increases cardiorespiratory motion artifacts

Definition of abbreviations: CT = computed tomography; MR = magnetic resonance; MRI = magnetic resonance imaging; SNR = signal-to-noise ratio; UTE = ultrashort–echo time.

enhancement (136). Lung deformation evaluated by coregistration of paired inspiratory/expiratory UTE MRI identifies regional fibrosis with acceptable correspondence with CT (137). For assessing ILD, UTE MRI protocols typically include noncontrast breath hold, steady-state free precession, and contrast-enhanced examinations providing complementary (138) data to high-resolution thin-slice CT, providing both functional and structural information in one examination (134, 139).

^{129}Xe "dissolved phase" MRI exploits the relatively high tissue solubility of xenon that results in its transmembrane diffusion through the alveolar wall into the bloodstream (140), where it binds transiently to hemoglobin in a manner similar to oxygen (140, 141, 142). Whole-lung spectroscopy (143, 144) has shown distinct resonance frequencies of xenon in gas, tissue, and blood compartments so that alveolar tissue density maps may be acquired to directly and regionally characterize fibrosis (145).

Caveats: MRI, particularly HP gas MRI, is expensive; the latter requires specialized hardware. Proton MRI using low-field scanners may reduce cost, and advanced image reconstruction with motion compensation during free breathing is rapidly evolving; reproducibility and validation studies are currently limited.

Assessing Airway Structure and Function

The human airway tree has >23 branching generations and exhibits 3D hierarchical heterogeneity in dimension, composition, and physiology; variations also exist with respect to sex and body and lung sizes. The first six or seven airway generations are readily visualized on inspiratory CT (the trachea is usually generation 0). The hierarchy must be considered when sampling airways for analysis and inferring airway structure and function. Selection of airways on the basis of a structural property (e.g., luminal diameter) or at random may result in comparison of airways from different hierarchical levels if the disease under study differentially alters airway structure or loss (e.g., COPD) (146). Table 5 shows some objective approaches to selecting hierarchically "similar" airways. No approach is perfect, as anatomical variations within and between individuals can introduce errors in selection. Multiple approaches may increase the robustness of airway structure–function inferences. Automatic labeling of the airway tree on the basis of segmental nomenclature has been used (147). Measurement of spatially matched airways has revealed that airway walls are generally thinner rather than thicker in COPD (146).

Common airway metrics include cross-sectional luminal diameter and area, wall thickness, wall area as a percentage of total airway area, and an estimated perimeter of a hypothetical "normalized" airway with an internal perimeter of, for example, 10 or 15 mm (148–152) derived from regression equations between the square root of airway wall area and its internal perimeter on the basis of certain assumptions (Table 5). Airway centerlines may be segmented and a branch-growing algorithm applied to generate distal lobe-filling airways (153). The resulting airway geometry, CT-derived tissue density, lung volumes, and pulmonary function test results may be combined in a full-scale airway network flow model to simulate whole-lung ventilation (154), correlated with *in vivo* HP ^{129}Xe MRI and ^{99m}technetium-labeled diethylenetriamine pentaacetate (DTPA) aerosol SPECT ventilation imaging in COPD (155).

The thinner airway walls in COPD (146, 156, 157) are collapsible (158). Expiratory central airway collapse may be measured on paired inspiratory–expiratory scans from the minor-axis diameter or cross-sectional area at selected anatomical levels. There is normally a wide range of age- and sex-dependent expiratory tracheal collapse (159, 160). Airway segmental mucus plugs have been visually counted, correlating with pulmonary function, oxygen saturation, MRI-derived ventilation heterogeneity (161–163), and locally reduced ^{3}He MRI signal (164).

Caveats: Static imaging may underestimate tracheobronchial collapse and not predict dynamic expiratory collapse (158–160, 165). CT-derived metrics for lung densitometry and airway structure may be influenced by age, height, TLC, gender, and smoking (82, 150, 166, 167). Sufficient airways should be measured to ensure an acceptable range of error (168).

Assessing the Vasculature

The human pulmonary vasculature comprises >23 branching generations from main pulmonary artery (PA) to alveolar capillaries, with only the first few generations being routinely visible. Standard CT using energy-integrating detectors (in-plane pixel dimension ~0.4 mm) limits the ability to accurately evaluate spatial properties of vessels that approach the voxel size (e.g., ~1 mm) (169). A 0.2-mm in-plane

Table 5. Common approaches in matching airways for comparative analysis

Selection Criteria	Example of Metric	Considerations
Anatomical property	Designation of "Terminal bronchiole"	Pathology may alter airway status (e.g., if the distalmost conducting airways are destroyed, the airway labeled as terminal bronchiole may appear to "migrate" centrally)
Branching hierarchy	Designating a generation number for each airway	There are anatomical variations in branching pattern; certain nomenclature systems do not cover the entire airway tree
Distance from landmark	Path distance (e.g., 5 cm from carina or pleura)	Body and lung size variations
Airway dimension	Lumen size (e.g., 2-mm-diameter airways)	Risk of bias when pathology alters airway dimension (e.g., COPD may narrow airway lumens; therefore, 2-mm airways may occur at a different generation compared with subjects without COPD)
Airways of a stipulated inner perimeter (Pi*X*)	Wall thickness of airways with inner perimeter of 10 mm (Pi10)	Regression assumptions should be confirmed in the condition(s) under study; potential effects of outliers on regression equation should be assessed

Definition of abbreviations: COPD = chronic obstructive pulmonary disease; Pi*X* = predicted wall thickness of airways with inner perimeter of *X*; Pi10 = predicted wall thickness of airways with inner perimeter of 10 mm.

pixel dimension has been obtained using a photon-counting scanner with ultrahigh-resolution matrix (170); even with this, most of the vasculature is not directly imaged. Micro-CT uses a small-bore compact scanner to image only a small volume of tissue (typical field of view ~16 mm vs. ~36 cm for conventional CT), yielding a spatial resolution of <0.01 mm, commonly used for *ex vivo* studies (42, 43, 171) and for *in vivo* studies in small animals (172).

Vessel Density, Tortuosity, and Fractal Dimension

Extraction of pulmonary vascular data from imaging data sets can be automated or semiautomated (cf. Reference 173). Arteries and veins may be automatically mapped, peripherally matched, and classified (174). Loss of pulmonary vascular density or distal PA blood volume is associated with right heart failure indices in smokers (175), emphysema progression (176), and asthma severity (177).

Besides density, vascular branching pattern is an important determinant of regional perfusion and function. Vessel tortuosity can be determined by comparing the linear distance between two points on a vessel with the actual 3D path length. This "distance metric" is increased in patients with pulmonary arterial hypertension (PAH) (178) and is correlated with mean PA pressure, pulmonary vascular resistance, and arterial and venous oxygen content and saturation. The fractal dimension, an index of the complexity of iteratively branching space-filling structures, may be determined by dividing the lung into cubes of equal size, whereupon all cubes containing a vessel are noted; the process is repeated using cubes of varying sizes down to a voxel. The number of vessel-containing cubes is related to cube size on a double logarithmic plot; fractal dimension is the slope of the linear portion of the plot (178). Alternately, fractal dimension can be estimated from CT or MRI perfusion scans (179) by calculating the relative dispersion (standard deviation/mean) of the image in progressively smaller blocks and evaluating the slope of the relationship between log relative dispersion versus log number of voxels averaged. *See* References (179 and 180) for details.

Pulmonary Artery (PA) Size and Distensibility

Central PA enlargement measured by CT (181) is commonly associated with, but not necessarily predictive of, PAH (182–184). There are insufficient data showing the clinical significance of PA dilation or whether PA size decreases with PAH treatment or if a decrease improves outcome (184). MRI can image PAs at specific times throughout the cardiac cycle; vessel cross-sectional area will change because of differential systole-to-diastole pressures; this change yields a measure of mean PA distensibility (mPAD), which can be determined without direct pressure measurements. mPAD can differentiate PAH from normal (185) and therapeutic responders from nonresponders (186) and can predict mortality among individuals with PAH (187).

Large-Vessel Blood Flow

Specific velocity-sensitive MRI sequences can characterize PA forward flow, retrograde flow, average flow velocity, and peak flow velocity. These metrics correlate with invasive measures of arterial pressure and vascular resistance (188).

Caveats: Quantification may be limited by ability to resolve distal lung structure (e.g., capillaries from larger vessels) (189). The spatial resolution of MRI is less than that of CT; thus, imaging of vascular trees is limited to visualized larger vessels.

Assessing the Pleura

Imaging metrics of pleural disease (190) include pleural thickness, percentage circumferential pleural involvement, and the number of foci of rounded atelectasis at anatomically defined levels (191). The presence and volume of pleural plaques quantified by CT have not shown significant association with indices of functional impairment (192, 193). Ultrasound (194) and transesophageal echocardiography (195) have been used to semiquantitatively assess pleural effusion volume (191).

Potential Caveats: It may be challenging to delineate indistinct pleural boundaries or reliably distinguish pleural fluid from thickening or fibrosis.

Assessing Regional Lung Mechanics

General Considerations

Metrics of lung mechanics reflect gas or blood transport into or through a structural compartment, calculated from the ratios of two primary measurements: *1*) *elastance* (or *stiffness*), the ratio of an applied pressure to a resulting increase in volume, ($\Delta P/\Delta V$), and *2*) *resistance*, the ratio of a pressure difference to the gas or blood flow between two points ($\Delta P/\Delta \dot{Q}$). Elastance and resistance are combined into a general function of *impedance* when the lung can be approximated as a linear dynamic system and into multiterm descriptions when linearity assumption is not applicable.

Whole-lung mechanics may be assessed from the pressure drop across the lung from the airway opening (trachea or mouth) to the pleural surface (often approximated by esophageal pressure). Inaccessibility of individual lung compartments impedes the determination of regional lung mechanics, but advanced imaging modalities can provide estimates of regional gas volumes and flows during ventilation; if regional pressures are also known, then local stiffness and resistance can be calculated (although not always possible to match rapid changes in local parameters under dynamic conditions). The difficulty of directly measuring local gas or blood pressures hinders validation of imaging-derived regional mechanics when these local pressure must be inferred from mathematical models on the basis of remote pressure measurements (196).

Measurement Principles and Methods

Imaging coupled with dynamic pressure, flow, and volume measurements enhances information yield about regional lung elastance, resistance, impedance, linear strain, and shear. Most approaches are based on relationships between gas flow and pressure at an appropriate entry point (197). The retrograde catheter technique (198) allows measurement of the *resistance of an airway segment* distal to a wedged catheter. An equivalent approach, wedging the tip of a bronchoscope into the lung, has been used in human subjects (199). Acinar-scale regional lung mechanics have been measured in animals by applying flow oscillations through an alveolar capsule to determine *input impedance* at the pleural surface (200). Invasive tracking of 3D movements of implanted radiopaque markers in the lung as inflation pressure changes has determined variations in *regional lung compliance* at centimeter resolution (201). Nonrigid coregistration of landmarks in paired CT or MR images obtained at different lung volumes allows quantitative mapping of regional *parenchymal deformation* (*strain*, *shear*) (202–204) (Figure 6). *Elastography* quantifies parenchymal stiffness by shear-wave propagation through the lung and tracking landmarks within high-resolution 3D images. This approach assumes a uniform pressure field; this limitation can be partially avoided by measuring regional pressures using miniature catheter-tip pressure transducers. ^{1}H MR elastography noninvasively measures shear stiffness during respiration in human lung (205) and in ILD (206). Ultrasound surface elastography could quantify subpleural shear stiffness as a marker of fibrosis and in staging ILD (207). Dynamic (four-dimensional) CT-based lung deformation analysis and elastography have mapped lung elasticity distribution in patients with COPD and lung cancer (208). Even without regional pleural or elastic recoil pressure, it is possible to estimate local air pressures using an anatomically accurate imaging-derived computational model of the lung on the basis of the laws of physics. For example, one can model gas pressures at any point in the airway tree assuming a standard flow regime along a network of cylindrical conduits (209, 210) or by applying computational fluid dynamics (211).

Caveats: Validation of imaging-based assessment of regional lung mechanics is challenging because the resolution of imaging modalities far exceeds that of physical transducers for measuring local pressures, flow, and volumes. Validating regional volumes and flow determined by imaging methods requires invasive measurement of these volumes and flow. Acinar-scale regional lung mechanics have been measured by applying broadband flow oscillations through an alveolar capsule (200); measurements are limited to pleural surface, and data from deep lung remain elusive.

Complicated image analysis algorithms are used to derive structural and functional information. There is often more than one useful way to extract information from an image, with limited understanding of which algorithm is best for a given application. The warping algorithms for transforming one image into another (e.g., at different lung volumes) (212) have been adapted from their application in other organs (e.g., brain) but remain unvalidated for the much greater deformation experienced by the breathing lung.

Without experimental gold standards for measuring regional lung mechanics independent of imaging, validation relies on predictions from computational models grounded in physics (See section "Applying Imaging Metrics in Computational Modeling to Predict Lung Function"); such models can be structurally accurate down to a submillimeter scale (213). Fluid dynamics enables pressure estimation throughout the airway tree, while well-studied empirical equations can estimate how parenchyma structures affect pressures. Nevertheless, using models to validate imaging-derived physiological conclusions is inferential and remains an open issue.

Assessing Ventilation and Inhaled Gas Distribution

General Principles

Alveolar ventilation, $\dot{V}_A$, is the rate of fresh gas delivery to the alveolar space (the dot denotes a rate). The term "specific ventilation" is used differently between methodologies, with some including a time component and some not. Thus, units of measurement should be stated. In MRI and nitrogen washout studies, specific ventilation (SV) is defined as the fraction of the original regional lung gas volume at end-expiration (V_r) that is replaced by a volume of fresh air or tracer gas (V_f) with each breath:

$$SV = \frac{V_f}{V_r} \quad (1)$$

SV is used to describe overall ventilation heterogeneity (214) in multiple-breath washout studies; this principle is also used in some imaging techniques (215, 216). Alternatively, fractional ventilation, a related volume measure, is sometimes used to measure the fraction of end-inspiratory lung volume that is made up of fresh air (or tracer gas):

$$\text{Fractional ventilation} = \frac{V_f}{V_r + V_f} = \frac{SV}{1+SV} \quad (2)$$

$\dot{V}_A$ is a metric of primary importance for gas exchange. SV and fractional

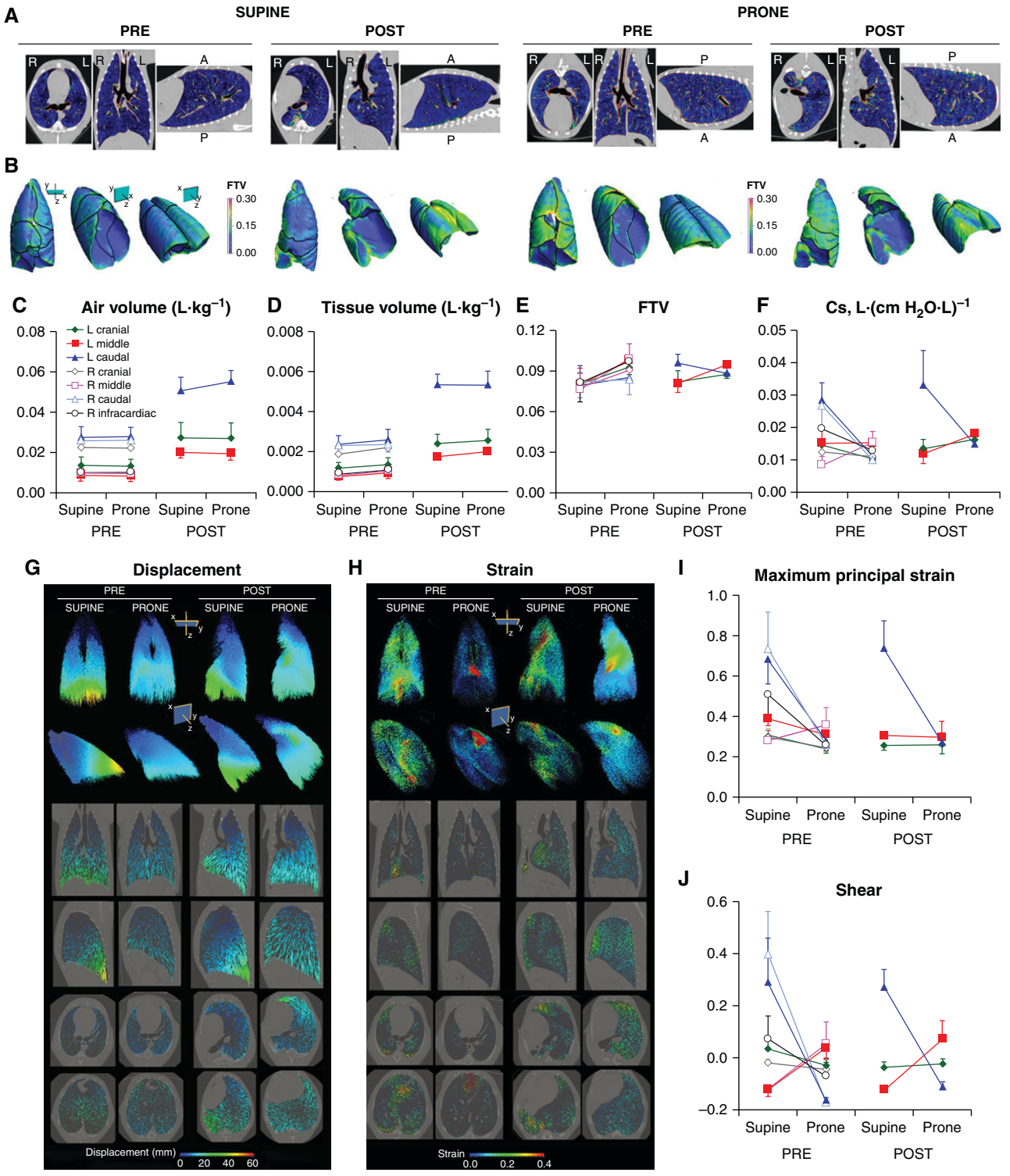

Figure 6. Computed tomography–derived metrics of regional parenchymal mechanics obtained during lung inflation in an adult canine model illustrate the use of quantitative imaging to evaluate the effects of posture and compensatory lung growth and remodeling before (PRE) and 4 months after (POST) right pneumonectomy (PNX, removing ~58% of lung units). (*A*) Two-dimensional images. (*B*) Three-dimensional rendering of lungs. Color scale shows lung tissue density (fractional tissue volume [FTV]). (*C–E*) Air volume (*C*), tissue volume (*D*), and FTV measured at a transpulmonary pressure (Ptp) of 30 cm H_2O (*E*). (*F*) Specific compliance (Cs) of individual lobes (seven PRE-PNX, three POST-PNX) calculated between Ptp values of 10 and 30 cm H_2O. (*G* and *H*) Displacement (*G*) and linear strain (*H*) vector maps were derived via coregistration of images obtained at the two values of Ptp, shown in three-dimensional renderings (upper) and two-dimensional (lower) images.

ventilation can be converted to $\dot{V}_A$ using respiratory rate and lung density to estimate V_r.

PET

Assessment of regional ventilation by PET uses the kinetics of nitrogen-13–labeled nitrogen (^{13}NN) (217, 218), neon-19 (^{19}Ne) (219), or gallium-68 (^{68}Ga)–labeled nanoparticles ("Galligas") (220). Production and optimization of radiolabels for ventilation and perfusion in PET and CT are reviewed elsewhere (221). Measurements are based on the time constant of washout curves after intravenous tracer injection or gas equilibration, providing regional specific ventilation, $s\dot{V}$, which combined with measurement of alveolar volume (resident gas) yields absolute $\dot{V}_A$ (222). Exploration of the multiexponential composition of washout curves allows assessment of ventilation heterogeneities below the voxel resolution that are key to quantifying ventilation dysfunction during severe bronchoconstriction (223) and mechanical ventilation (224).

CT, PET–CT, and SPECT–CT have documented heterogeneous deposition of inhaled aerosols and particulates (225–229), validated experimentally against fluorescent microspheres (230). Imaging data may be combined with theoretical modeling (231) to simulate physiological conditions, examine the factors causing variability, and predict *in vivo* response.

MRI

Distribution of ventilation may be assessed using proton-based ^{1}H MRI and direct imaging of exogenous gases using multinuclear MRI and spectroscopy (Table 6, including comparison with PET).

Imaging regional lung expansion. Using ^{1}H MRI with UTE (echo times $\leq$0.2 ms) or fast gradient-echo techniques (echo times $\sim$1 ms), lung density can be quantified and normalized to nearby tissue with similar T1 and/or T2 characteristics (e.g., muscle [232–234]), using reference phantoms (235), very low flip angles, or some combination of these. This allows measurement of changes in macroscopic density during the respiratory cycle using deformable image registration techniques. Density changes provide a proxy measure of regional ventilation, with modest correlations to fractional ventilation measured by HP gas inhalation (236, 237). ^{1}H MRI measurements are relatively simple using standard hardware, without any need for tracer gas and with potential for 3D acquisitions.

HP gas techniques. Using inhaled HP ^{129}Xe or ^{3}He MRI, gas distribution abnormalities during static breath-hold imaging can be assessed by the ventilation defect percentage (VDP). VDP is the total volume of lung with signal intensity below a threshold (typically a small percentage of average signal intensity) normalized to thoracic cavity volume (238). VDP derived from ^{3}He or ^{129}Xe is a safe and reproducible measure correlating with clinical disease measures (239–241). In COPD, ^{3}He VDP correlates with spirometry (242), symptoms, exercise capacity (128), CT-based measures of emphysema, and clinical exacerbations (243, 244). ^{129}Xe MRI has also demonstrated similar correlations with spirometry (245). Ventilation defects are spatially related to gas trapping and emphysema measured using CT (246). Bias between VDP measured with ^{3}He and ^{129}Xe (242, 247, 248) MRI are likely due to the density and viscosity of each gas, resulting in different flow dynamics in different caliber airways (249), but both demonstrate higher sensitivity to mild obstruction than spirometry (250, 251).

Oxygen-enhanced MRI, Fourier decomposition, and fluorine imaging. Oxygen-enhanced (OE) MRI and Fourier decomposition (FD) MRI are performed during tidal breathing. FD MRI (252) depends on the periodic ^{1}H MRI signal intensity fluctuations that accompany changes in local lung parenchymal density with respiration and pulsatile blood flow. OE MRI (253, 254) exploits the paramagnetic effect of molecular oxygen: as O_2 diffuses into tissues and blood, local MR signals are altered because local T1 (longitudinal relaxation time) shortens as local dissolved oxygen concentration rises (255). SV imaging (SVI) (215, 256) is an OE method that uses the *rate of change* in T1, which depends on the rate of wash-in/washout of inhaled oxygen to a region to directly measure regional SV. Recent advances in OE MRI (257–260) have improved the spatial resolution and repeatability of semiquantitative estimates of VDP (258) and quantitative regional SV maps (215, 216), supporting translation in a wide range of lung diseases. OE MRI and SVI metrics are strongly correlated with pulmonary function standards (e.g., multibreath nitrogen washout [256]) and with HP ^{3}He MRI (261, 262).

Alternative approaches using tracers (e.g., perfluorinated gases) allow direct measurement of MR signal from multiple ^{19}F nuclei in each atom of tracer gas (263). This approach can capture dynamic airspace filling during tidal breathing (263–265), providing voxel-wise measures of SV (Equation 1). Relative to HP ^{3}He MRI, ^{19}F imaging is inexpensive because the technique does not use hyperpolarization.

Caveats: Signal-to-noise ratio and spatio-temporal resolution are limited. Most methods depict the distribution of an inhaled tracer gas that is proportional to SV (acquired during a breath hold) or reflect information averaged over multiple respiratory cycles (e.g., steady-state tidal breathing). In single-breath tracer inhalation techniques, a "ventilation defect" does not necessarily represent absent ventilation, as low-signal regions may reflect poorly ventilated regions (slow time constants) that receive less inhaled gas but are not true ventilation defects. Imaging a tracer (oxygen or ^{19}F) over multiple breaths requires long scan times ($\sim$10–20 min) and increased postprocessing complexity.

Figure 6. (*Continued*). (*I* and *J*) Maximum principal strain (MPS) (*I*) and shear (in the sagittal plane) (*J*) of each lobe. Data are mean ± standard deviation. With respect to postural effects, at PRE-PNX baseline, prone posture is associated with higher FTV in dependent regions (*B*), lower Cs, displacement, and strain magnitudes in most lobes, especially the caudal lobes (*F–I*), and lower interlobar heterogeneity in Cs (*F*), MPS (*I*), and shear (*J*) but selectively increased lung strain in a small region under the heart (*H*) compared with prone posture. With respect to PNX effects, POST-PNX mediastinal shift and expansion of the remaining lobes (*A* and *B*) stimulated acinar tissue growth and doubled air and tissue volumes (*C* and *D*) without altering FTV (*E*), increased parenchymal excursion (*G*), and altered intralobar regional strain distribution (*H*) during lung inflation compared with the corresponding PRE-PNX baseline. Compensatory lung growth and concurrent parenchymal remodeling nearly normalized average lobar Cs (*F*), MPS (*I*), and shear (*J*) and preserved the normal postural response patterns. Adapted by permission from Reference 203. A = anterior; L = left; P = posterior; R = right.

Table 6. Comparison of different techniques to measure ventilation and its heterogeneity

	HP ^{3}He MRI	HP ^{129}Xe MRI	^{19}F MRI	OE MRI	^{13}NN PET
Signal-to-noise ratio	Higher	Higher	Lower	Lower	Higher
Breath hold vs. free breathing	Breath hold	Breath hold	Both	Free or controlled breathing	Free breathing
Relative cost	Very high	Medium	Medium	Low	High
Hardware requirement	High	High	Medium	Low	High
IND exemption required	Yes	Yes	Yes	No	Yes
Scan length	Seconds	Seconds	Seconds to minutes	10–20 min	Minutes
Major metrics	Ventilated volume, VDP	Ventilated volume, VDP	VDP, fractional ventilation	Percentage signal enhancement, VDP, specific ventilation, DP_{O_2}	Ventilated volume, VDP, specific ventilation
Multicenter repeatability established	Yes	No	No	No	No
Advantages	Regional measures of emphysema/gas trapping and airway occlusion have high sensitivity for longitudinal and interventional assessments	Regional measures of emphysema/gas trapping and airway occlusion have high sensitivity for longitudinal and interventional assessments Ability to image gaseous and dissolved phases enables assessment of gas exchange	Regional measures of emphysema/gas trapping and airway occlusion	Can be performed using conventional coils without additional gas preparation/handling hardware measures of heterogeneity validated against multiple breath washout, and against HP ^{3}He MRI	Regional measure of gas trapping Provides direct assessment of regional alveolar ventilation Validated in conjunction with perfusion against arterial blood gases
Disadvantages	Requires multinuclear, dedicated transmit/receive coil, specialized sequences, and ^{3}He hyperpolarizer	Requires multinuclear, dedicated transmit/receive coil, specialized sequences, and ^{129}Xe hyperpolarizer	Requires multinuclear, dedicated transmit/receive coil and specialized sequences	Typically long acquisition times	Radiation exposure Requires several breaths to estimate subvoxel ventilation heterogeneity from ^{13}NN-washout curve

Definition of abbreviations: DP_{O_2} = change in partial pressure of oxygen; HP = hyperpolarized; IND = investigational new device; MRI = magnetic resonance imaging; OE = oxygen-enhanced; PET = positron emission tomography; VDP = ventilation defect percentage.

Techniques that rely on imaging of lung expansion to infer ventilation are critically dependent on accurate registration. Regional lung expansion rather than true ventilation is measured (e.g., gas-trapped regions may expand with inspiration, reducing local density even in the absence of any gas influx, introducing error).

Assessing Pulmonary Perfusion

Perfusion ($\dot{Q}$) is the process of delivering blood to the capillary bed, which, coupled with $\dot{V}_A$, determines pulmonary gas exchange. Different techniques are shown in Table 7.

CT

Intravenously injected iodine is used in conventional CT to measure regional PBV as a proxy for perfusion by subtracting unenhanced precontrast images from corresponding postcontrast images (266, 267). Motion correction is applied to minimize potential errors in coregistering paired images; this technique clearly visualizes regional defects (268). Alternatively, DECT evaluates PBV after iodinated contrast injection (269–271) using two X-ray beams of different energies or spectral detectors and material decomposition to visualize iodine distribution that exhibits differential attenuation properties at different energies (272, 273). DECT correlates well with first-pass kinetics (274) and detects regional defects with higher sensitivity than conventional angiography (68, 275). A lower dose dynamic CT technique that measures pulmonary perfusion using only two serial scans has been validated against fluorescent microspheres in animals (276).

PET

PET assessment of regional perfusion is based on the kinetics of tracers: ^{13}NN, oxygen-15–labeled water (^{15}O-H_2O), or gallium-68 (^{68}Ga)–labeled particles/compounds. Because of its low blood–gas partition coefficient, intravenously injected ^{13}NN reaching lung capillaries mostly diffuses into alveoli, allowing assessment of true capillary perfusion (222, 277). Main ^{13}NN-based approaches are as follows:

1. Continuous ^{13}NN infusion, where perfusion is derived as

$$\dot{Q} = \frac{\dot{V}_A}{\dot{V}_A/\dot{Q}} \quad (3)$$

   while ventilation is computed from inhalation of neon-19 gas (278), and
2. ^{13}NN-saline bolus: perfusion is computed from the distribution of an injected bolus of ^{13}NN-saline during a breath hold (218, 277), where the end–of–breath hold activity characterizes capillary perfusion specific to aerated regions.

The ^{15}O-H_2O–based method measures perfusion from local kinetics of injected ^{15}O-H_2O, accounting for the input function into pulmonary circulation and water extraction

Table 7. Comparison of different techniques to measure perfusion and its heterogeneity

	CT	^{13}NN PET	SPECT	ASL MRI	Bolus Contrast Enhancement MRI
Spatial resolution	Highest	Moderate	Low	High	High
Cost	Relatively low	Relatively high	Low	Relatively high	Less than ASL
Breath hold vs. free breathing	Breath hold	Breath hold	Both	Free or controlled breathing	Breath hold
Scan length	Seconds	Few minutes	Several minutes	Minutes	Seconds
Major metrics	Perfused blood volume Perfusion defects	Regional shunt (for early peak in kinetics) Perfusion (ml/min/ml) Relative dispersion Length-scale perfusion heterogeneity Noise-free estimate of perfusion heterogeneity	Relative perfusion, perfusion defects	Perfusion (ml/min/ml) Perfusion (ml/min/g) Relative dispersion, fractal dimension Gravitational gradients	Time to peak contrast enhancement (transit time), blood volume, perfusion defects, relative perfusion
Validation	Validated against microspheres in animal model	Combined with ventilation to give $\dot{V}_A/Q$ validated against systemic experimentally assessed arterial blood gases and MIGET	Combined with ventilation to give $\dot{V}_A/Q$ validated against MIGET	Validated in phantoms and against microspheres Combined with ventilation to give $\dot{V}_A/Q$ validated against MIGET	Limited validation in cerebrum and in phantoms
Advantages	High spatial resolution Widely available and in use	Highly sensitive Allows quantification of gases directly involved in pulmonary gas exchange Coregistration with other tracers allows relevant association of molecular and functional information Short tracer half-life allows sequential acquisition of measurements Enables quantification of heterogeneity underlying the imaging resolution	Widely available, used clinically	Noninvasive and no "dose" Combined with density imaging, provides insight into effects of lung deformation Temporal imaging possible Sensitive to modest physiological interventions and lung disease (e.g., PAH) Uses a standard 1.5-T clinical scanner without hardware modification	Uses a standard 1.5-T clinical scanner without hardware modification Widely available
Disadvantages	Relatively high exposure to ionizing radiation Requires injection of iodinated contrast Relationship between perfused blood volume and perfusion not established Conduit vessel signal requires removal or separation to assess true perfusion	Exposure to ionizing radiation May require a stable breathing pattern, which may not be easily followed by spontaneously breathing subjects Requires cyclotron to be immediately available Requires kinetics analysis (for improved accuracy) and does not identify the location of heterogeneity within the voxel Low temporal resolution may underestimate perfusion Quality of segmentation is important, as it cannot uncouple shunt from large blood vessels Requires several breaths for estimation of alveolar ventilation and $\dot{V}_A/Q$ ratios as derived from washout curve	Exposure to ionizing radiation Semiquantitative as typically implemented	Low proton density and short T2* make SNR an issue Currently single slice, making whole-lung imaging more time consuming Absolute calibration of signal possible but requires postprocessing and reference phantoms Conduit vessel signal requires removal or separation Requires cardiac gating and reliable lung volume control (or postprocessing for registration) Translation to 3-T is challenging (but possible) Data processing is cumbersome	Requires contrast injection, not suitable for some subjects (e.g., impaired renal function) Indirect measure of perfusion Semiquantitative as typically implemented Accurate estimation requires arterial input function, which is rarely available Conduit vessel signal requires removal or separation to assess true perfusion

Definition of abbreviations: ASL = arterial spin labeling; CT = computed tomography; MIGET = multiple–inert gas elimination technique; MRI = magnetic resonance imaging; PAH = pulmonary arterial hypertension; PET = positron emission tomography; SNR = signal-to-noise ratio; SPECT = single-photon emission computed tomography; $\dot{V}_A/\dot{Q}$ = ventilation-perfusion ratio.

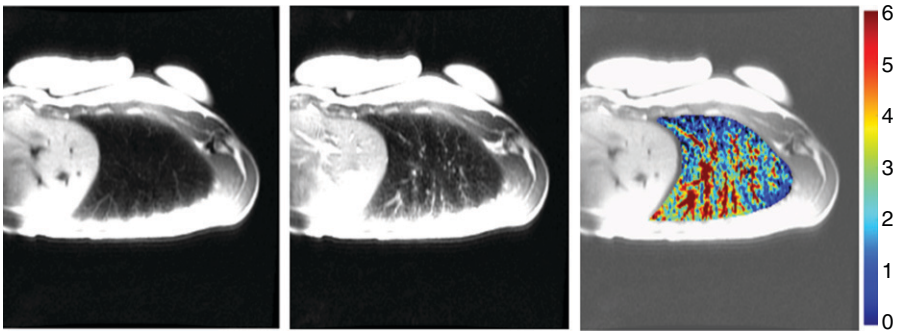

Figure 7. Sagittal images showing an arterial spin labeling experiment in the lung to quantify pulmonary perfusion in a normal subject. Images are shown in the orientation of acquisition to visualize the large-scale effects of gravity on the lung. In the left-hand "tag" image, a nonselective inversion pulse has been applied, and the intravascular signal is largely nulled. In the middle "control" image, a selective inversion pulse has resulted in intravascular signal appearing bright; lobar fissures can be faintly seen because vessels do not cross lobar boundaries. Subtraction of the tag and control images results in a map of delivery of one systolic ejection of blood after quantification (right), showing greater perfusion in the gravitationally dependent lung. The color scale is blood delivered (ml/min/cm^3). The bright structures on the anterior chest wall are phantoms used in quantification. Courtesy of S.R. Hopkins.

by the lung (279–281). In addition, pulmonary perfusion has been measured with intravenously injected positron-emitting ^{68}Ga microspheres (282, 283) that lodge in pulmonary capillaries in proportion to local perfusion. ^{68}Ga-chelated 1,4,7,10-tetraazacyclododecane-1,4,7,10-tetraacetic acid (DOTA)–measured perfusion agrees reasonably with measurements using fluorescent microspheres (284).

Surrogate PET-based methods using intravenous fluorine-18–labeled fluorodeoxyglucose (^{18}F-FDG) can assess pulmonary perfusion in regions of interest larger than a pixel. The fraction of blood obtained from ^{18}F-FDG kinetics approximates ^{15}O-H_2O perfusion measurements in normal and post–acute lung injury large animals (285). Relative perfusion is estimated by accounting for delays in ^{18}F-FDG transport between plasma sampling site and lung regions of interest; this method correlates highly with previously validated ^{13}NN perfusion measurements (286). These positive results match previous good correlations found between PBV measured using labeled carbon monoxide and lung perfusion (287).

Single-photon Emission Computed Tomography (SPECT)

SPECT measures pulmonary perfusion using injected ^{99m}technetium- or ^{113m}indium-labeled macroaggregated albumin (MAA) (288–290) (*See* section "Metrics for Assessing Regional Rentilation-perfusion Mismatch").

MRI

Two major MRI methods are used to evaluate lung perfusion. *1*) A bolus of gadolinium, an injectable contrast agent, is used to enhance MR signal during its passage. Indicator dilution techniques are applied (291) to derive perfusion from the time to peak signal intensity (reflecting transit time) and the area under the time–activity curve (reflecting blood volume) (291, 292), using the central volume principle (293). *2*) The 2D arterial spin labeling (ASL) flow-sensitive alternating inversion recovery sequence (FAIRER) (294–297) uses magnetic field gradients and radiofrequency pulses to manipulate the signal of blood delivered to an imaged slice in different ways: one image with delivered blood generating a strong signal and one in which the signal is largely nulled (Figure 7). Two electrocardiogram-gated images of each slice are taken ~5 seconds apart. The signal in a voxel of the subtracted image is proportional to the amount of blood delivered during the previous cardiac cycle; multiple slices are acquired sequentially to cover the entire lung. These techniques have been validated in animal models (298) and phantoms (299, 300) or against the multiple inert gas elimination technique (MIGET) (301).

Perfusion Metrics

Perfusion measurements may be expressed as *relative perfusion* (i.e., a fraction of total perfusion) or *absolute perfusion* (i.e., the volume of blood delivered per unit volume or mass per unit time); the metric used should be clearly stated. Perfusion heterogeneity is affected by gravity, vascular branching structure, active regulation (e.g., hypoxic pulmonary vasoconstriction), and disease (302). The simplest measure of spatial heterogeneity is the relative dispersion (RD, or coefficient of variation) of an image (standard deviation divided by average signal intensity). RD is independent of absolute signal quantification, simple to calculate, and sensitive to physiological interventions (179, 303–306). Descriptors that account for signal distribution (e.g., log normality) may require absolute quantification, adding complexity (295). Additional metrics include vertical perfusion gradients (12, 307, 308), the *noise-free* estimate of perfusion heterogeneity (309), and the contribution of specific ranges of length scales to perfusion heterogeneity (310, 311) and the fractal dimension (179, 180). Studies using ASL measures of perfusion or contrast enhancement were used to show increased perfusion heterogeneity in hypoxia, suggesting uneven hypoxic pulmonary vasoconstriction (312, 313), in individuals with a history of high-altitude pulmonary edema. RD is also elevated in patients with Fontan circulation and PAH (314). Another example is the finding that the length scale of perfusion heterogeneity differs between normal subjects and patients with COPD (310) and between patients with exercise-induced PAH and control subjects at rest (308).

Pulmonary ASL is well suited for studying temporal perfusion variations; the technique does not use injected contrast or ionizing radiation allowing serial image acquisition. Using a free-breathing scanning protocol consisting of a series of electrocardiogram-gated scans (315), an ASL series can be acquired and registered and temporal perfusion fluctuations calculated (316, 317). Results demonstrate active normal control of pulmonary perfusion (316–318) and marked alterations in PAH (319).

Caveats: Tissue deformation with gravity creates an apparent gradient in alveolar–capillary perfusion per unit volume even when perfusion per alveolus is uniform (5). Lung volume during image acquisition affects quantification (11, 320, 321) and perfusion distribution. Depending on the study, it is important to distinguish between perfusion per unit lung volume and perfusion per alveolus. Density measure provides a surrogate for local deformation, and

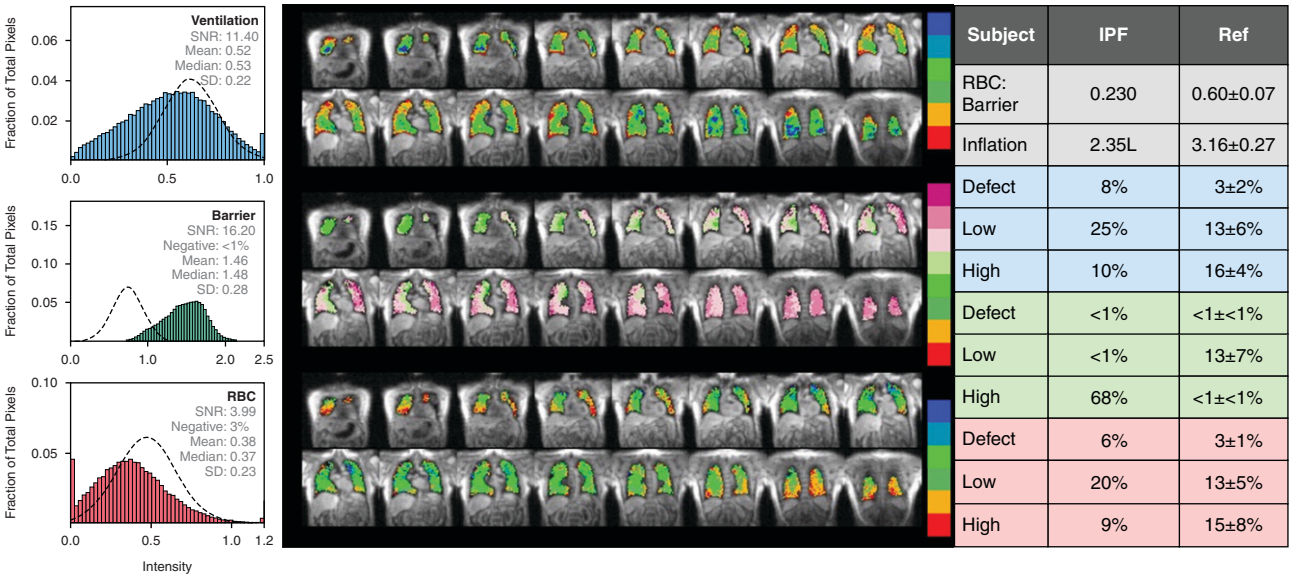

Subject	IPF	Ref
RBC: Barrier	0.230	0.60±0.07
Inflation	2.35L	3.16±0.27
Defect	8%	3±2%
Low	25%	13±6%
High	10%	16±4%
Defect	<1%	<1±<1%
Low	<1%	13±7%
High	68%	<1±<1%
Defect	6%	3±1%
Low	20%	13±5%
High	9%	15±8%

Figure 8. Representative report showing the use of ^{129}Xe magnetic resonance imaging to evaluate single-breath gas distribution and gas exchange in a patient with idiopathic pulmonary fibrosis (IPF). The report provides histograms (left), color-coded maps (middle), and quantitative metrics (right) related to ventilation, interstitial barrier status, and gas transfer to capillary red blood cells (RBC). The quantitative maps assign each voxel a color code depending on how its intensity deviates from the healthy reference population means (histograms on the left). Red pixels indicate "defects" (pixel intensities more than 2 standard deviations [SDs] below the mean), while green voxels are those falling within 1 SD, and blue represent intensities 2 SDs above the mean (for ventilation and RBC transfer maps). Uniquely, the barrier maps have at their upper scale pink and purple to denote voxels with ^{129}Xe uptake more than 2 SDs above healthy reference, which has been associated with interstitial thickening. For each map, the percentage of the thoracic cavity falling within the defect, low, and high ranges is provided, together with reference values from a young, healthy reference population (Ref, gray cells in the table, dotted curves in histograms). Courtesy of B. Driehuys. SNR = signal-to-noise ratio.

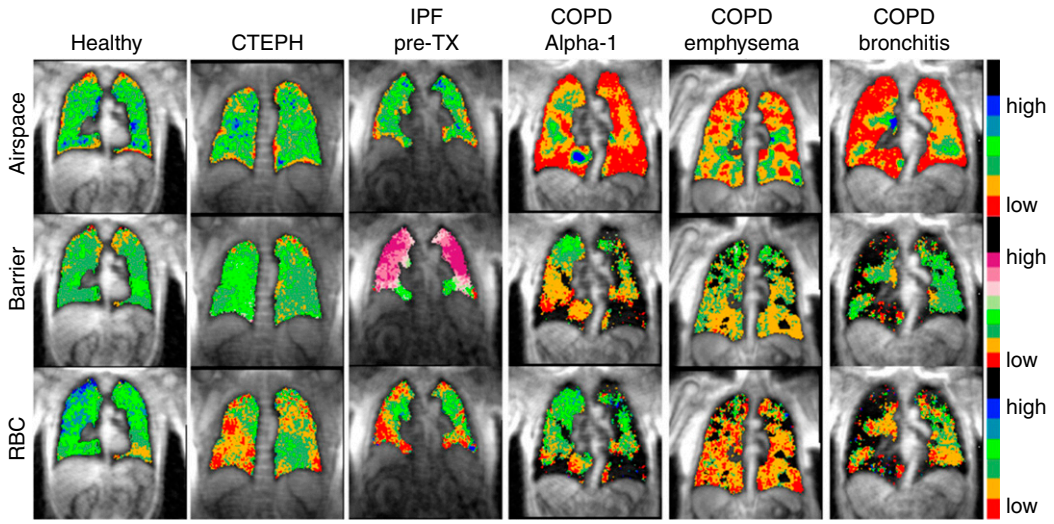

Figure 9. Representative ^{129}Xe ventilation and gas exchange magnetic resonance imaging maps from a range of disease conditions. Note that the healthy volunteer is characterized by maps falling in the green range of the healthy reference cohort values. The patient with CTEPH exhibits primarily defects in red blood cell (RBC) transfer. The subject with IPF exhibits high barrier uptake (interpreted as a thickened diffusion barrier), with basilar and peripheral loss of RBC transfer. Patients with COPD all exhibit significant ventilation defects, while two exhibit low barrier uptake (interpreted as emphysema), and all exhibit low RBC transfer. Courtesy of B. Driehuys. COPD = chronic obstructive pulmonary disease; CTEPH = chronic thromboembolic pulmonary hypertension; IPF = idiopathic pulmonary fibrosis; TX = treatment.

correction for regional density provides a useful first-order means to convert between the two measurements (5).

As the lung normally receives the entire cardiac output, it is more important to assess regional distribution of perfusion than total flow. For evaluation of gas exchange, the perfusion signal should come from sources that represent capillary perfusion in the voxel of interest.

Many so-called perfusion scans actually reflect blood volume, particularly in larger vessels; the relationship between blood volume and flow is not fully established, particularly in disease. DECT or subtraction CT perfusion measures yield only a snapshot of iodine enhancement; perfusion quantification requires rapid sequential four-dimensional CT to assess temporal changes (56, 321, 322), producing high radiation exposure and lower image resolution.

Although ^{13}NN PET and SPECT provide signal specific to blood in pulmonary capillaries, other techniques (ASL MRI, CT) comprise signal from both capillaries and conduit vessels carrying blood destined for elsewhere. Removal of conduit vessel signals (323–325) is essential to quantify capillary perfusion participating in gas exchange.

Perfusion heterogeneity can occur at a large spatial scale (e.g., gravity dependent) (5, 179, 180, 326) and smaller scales. The metrics are scale dependent; scale information should be stated when reporting results (180).

Additional metrics are evolving for specific situations and direct between-technique comparisons of the magnitude and spatial distribution of perfusion. Hybrid cameras (e.g., PET–CT and PET–MRI) advance accurate quantification and comparisons, as they incorporate inherent image coregistration. Because of distinct physical principles of measurement, different techniques are not equivalent; specific applications for each method remain to be determined.

Assessing Ventilation and Acinar Air–Tissue–Blood Diffusion

HP ^{129}Xe MRI permits breath-hold imaging of inhaled gas distribution in airspaces (discussed previously) and its uptake in interstitial tissues and plasma and transfer to pulmonary capillary RBCs. This capability provides unique windows into obstructive conditions such as asthma (327, 328), cystic fibrosis (329), and COPD (330), while the ability to probe air–tissue–blood diffusion is suited for studying interstitial (145) and pulmonary vascular (331) disease.

HP ^{129}Xe MRI can image acinar diffusion, driven by xenon's solubility and diffusion across alveolar septal tissue and plasma and into capillary RBCs (332). Each of these compartments is associated with unique ^{129}Xe resonant frequencies (333), which combined with novel MR acquisition strategies allow ^{129}Xe distribution in each to be 3D encoded during a breath-hold (334); signal is constrained to arise primarily from the alveolar–capillary gas exchange interface, and not larger vessels (142). ^{129}Xe thus reports on structure and function at much smaller length scales (micrometers) than the resolution of the images (3–5 mm isotropic). Additional ^{129}Xe spectroscopic sampling of the alveolar–capillary unit every 15 ms provides metrics of blood oxygenation and hemodynamics (335).

HP ^{129}Xe MRI is fast and well tolerated (239, 336), allowing visualization of gas distribution and yielding information on ventilation, alveolar barrier integrity, and capillary RBC transfer. Its noninvasive nature

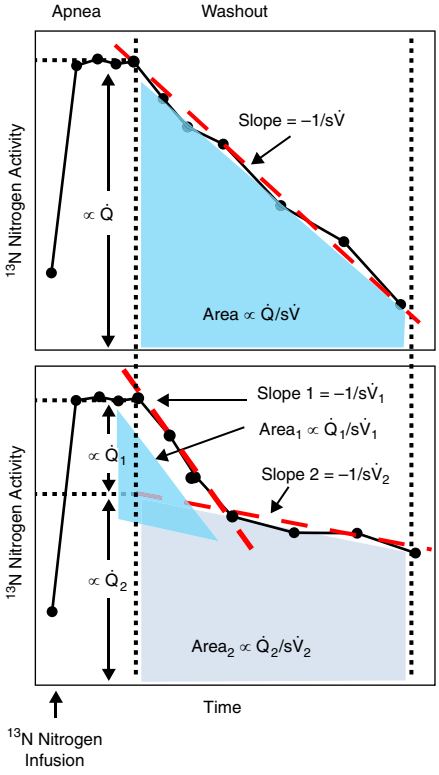

Figure 10. ^{13}N-nitrogen tracer kinetics showing the derivation of quantitative measures of specific ventilation (sV̇ in PET) and perfusion (Q̇). Top: Washout of ^{13}N-nitrogen plotted on a log scale showing activity versus time in a voxel exhibiting uniform behavior modeled as a single compartment. ^{13}N-nitrogen is injected during apnea and delivered to the alveolus in proportion to regional blood flow; thus, the plateau in activity at the time of the first appearance is proportional to regional perfusion in a given voxel. Then, as the subject begins breathing, the tracer in the alveolus will wash out proportional to regional sV̇, and the slope of washout is equal to $-1/sV̇$. The area under the curve (light blue) is proportional to the Q̇/sV̇ ratio. Bottom: ^{13}N-nitrogen washout plotted on a log scale showing activity versus time in a voxel exhibiting two-compartment behavior, with compartment 1 having high sV̇ (rapidly clearing) and compartment 2 having low sV̇. During washout, compartment 1 clears tracer rapidly, with a steep initial slope (slope 1) of activity versus time. Total blood flow in the voxel ($\dot{Q}_1 + \dot{Q}_2$) is again reflected in the plateau but apportioned between the two compartments on the basis of the back-extrapolated point to the onset of washout in compartment 2. The Q̇/sV̇ for compartment 1 is shown in light blue and for compartment 2 is shown in gray. Reproduced with permission from Reference 371.

permits repeated scanning. Ongoing methodological innovation (e.g., novel coils and polarizer technology) seeks to accelerate image acquisition (337) and identify new contrast mechanisms (26).

Metrics

Figure 8 illustrates a typical HP ^{129}Xe MRI study (338) reporting on gas distribution in airspaces, barrier tissues and plasma and transfer to RBCs, and ability to characterize abnormalities. Figure 9 shows images from patients with lung diseases. Dynamic ^{129}Xe spectroscopic sampling of alveolar–capillary unit is used to characterize RBC frequency shift and its cardiogenic oscillations, which are believed to reflect capillary oxygenation and capillary blood volume, which may be used to assess pulmonary hypertension (331).

Caveats: HP ^{129}Xe is a drug/device combination regulated by federal guidelines. Implementation remains expensive, requiring an MRI scanner with multinuclear capabilities, specific pulse sequences (339), and custom software (340). The field is just coming to agreement on the most useful types of image acquisition or analysis (332, 341). HP ^{129}Xe signal is transient; imaging is time sensitive and with some exceptions (342) is limited to single-breath scans. These factors demand excellent patient coaching and gas delivery practices to ensure well-defined lung volumes (343), adequate inhaled ^{129}Xe, and maintenance of breath hold during imaging. Reproducibility and validation studies are limited.

Assessing Regional Ventilation–Perfusion Mismatch

Matching regional $\dot{V}_A/\dot{Q}$, a primary determinant of pulmonary gas exchange efficiency, may be assessed using MRI and nuclear medicine techniques.

PET

Estimates of $\dot{V}_A/\dot{Q}$ distributions using PET are based mainly on intravenously administered ^{13}NN tracer kinetics (222, 277) (*See* section "Assessing Pulmonary Perfusion") (Figure 10). Continuous infusion measurements require estimates of mixed venous ^{13}NN content and alveolar gas (217, 344). In the bolus technique during apnea, regional $\dot{V}_A/\dot{Q}$ is computed from the area under the activity–time curve as steady-state ventilation begins after a breath hold (218, 279). Because ^{13}NN diffuses only into aerated lung units, local ^{13}NN kinetics allow the estimation of not only regional $\dot{V}_A/\dot{Q}$ ratio but also right-to-left shunt (222, 345, 346).

SPECT

SPECT measures ventilation or perfusion and reconstructs a 3D image (288, 289) after injecting or inhaling a γ-emitting compound; the photons emitted during decay are imaged. Pulmonary perfusion measurements with SPECT typically involve injection of ^{99m}Tc-MAA, ^{133m}In-MAA (288–290) particles distributed in proportion to local blood flow and lodged in small pulmonary arterioles and capillaries. Ventilation is measured by inhaled aerosolized particles (^{133}xenon or ^{99m}technetium-labeled diethylenetriamine pentaacetate) or ^{99m}technetium-labeled nanoparticles (347).

MRI

The most developed technique to quantify regional $\dot{V}_A/\dot{Q}$ matching combines three proton MRI sequences (Figure 11): *1*) SVI (*See* section "Assessing Ventilation and Inhaled Gas Distribution" above), *2*) perfusionmeasured using ASL (*See* section "Assessing Pulmonary Perfusion" above), and *3*) proton density. Proton density is used to assess the air compartment of the voxel as (1 − density). When multiplied by local SV, this gives the volume of fresh gas/breath and is used to calculate regional $\dot{V}_A$ (301, 348).

Alternately, regional partial pressure of oxygen (P_{O_2}) can be quantified from HP ^{3}He MRI by acquiring a back-to-back image series (349–351) and evaluating regional changes in signal intensity with time (352); regional $\dot{V}_A/\dot{Q}$ ratio is estimated from the measured P_{O_2} using mass balance equations for respiratory gases (353).

Metrics

Regional $\dot{V}_A/\dot{Q}$ heterogeneity can be described with simple functional models corresponding to a few compartments and a narrow unimodal $\dot{V}_A/\dot{Q}$ distribution (354). Small-length scale heterogeneity develops in disease (222, 223, 355) and under mechanical ventilation (224), resulting in heterogeneous $\dot{V}_A/\dot{Q}$ distributions (356, 357) (Figure 12). Metrics of $\dot{V}_A/\dot{Q}$ matching include global heterogeneity, the second moments (log scale) of ventilation (LogSD$\dot{V}$) and perfusion (LogSD$\dot{Q}$) versus $\dot{V}_A/\dot{Q}$ ratio distributions, calculated in a 50-compartment

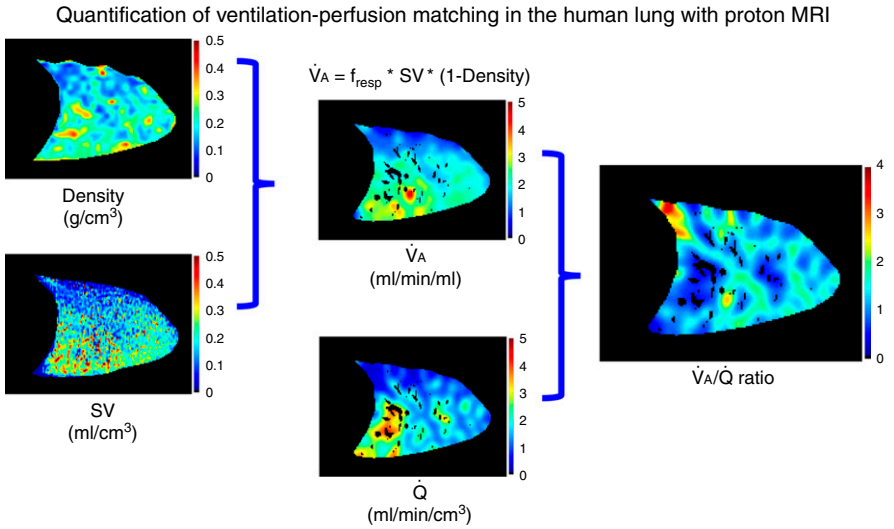

Figure 11. Analysis pathway for the quantification of regional alveolar ventilation/perfusion ($\dot{V}_A/\dot{Q}$) ratio from proton MRI proton density, specific ventilation (SV), and $\dot{Q}$ (arterial spin labeling) images. Quantified density images are used as a measure of regional gas content and combined with SV images (representing delivery of fresh gas/resident gas) to provide an estimate of regional $\dot{V}_A$. The smoothed ventilation image is then divided by the quantified and smoothed $\dot{Q}$ image to give a map of regional $\dot{V}_A/\dot{Q}$ ratio. The dark tubular structures in the ventilation, $\dot{Q}$, and $\dot{V}_A/\dot{Q}$ ratio images represent voxels that have signal characteristics consistent with large conduit vessels, which are masked out for calculations because they do not represent local $\dot{Q}$ (301, 348). Courtesy of Rui Carlos Sá. f_{resp} = respiratory frequency; MRI = magnetic resonance imaging.

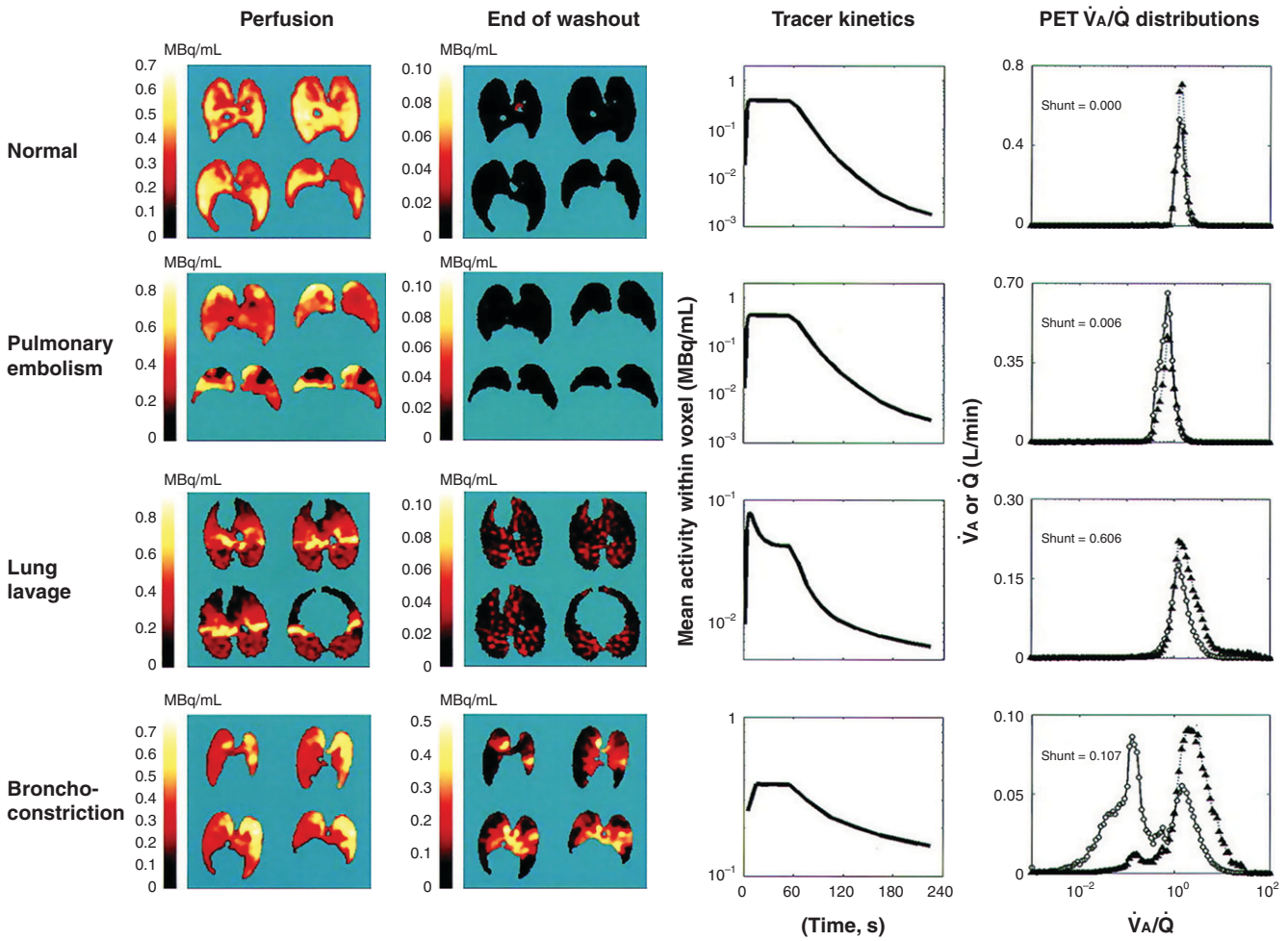

Figure 12. Regional perfusion and end-of-washout lung images, tracer kinetics of whole-lung field, and PET–derived $\dot{V}_A/\dot{Q}$ distributions for single examples of a normal sheep and a sheep after pulmonary embolism, saline lung lavage, and bronchoconstriction. Images are tomographic sections viewed in craniocaudal direction from top to bottom. Animals were prone for normal, bronchoconstriction, and pulmonary embolism studies and supine for lung lavage study. In supine position, left side in image corresponds to left side in animal. Note different scales for images. Regions of unperfused lung are seen after embolism. After lung lavage, there is redistribution of perfusion and increase in residual tracer at end of washout. Early peak and fast drop to plateau in lung lavage tracer kinetics indicate the presence of intrapulmonary shunt. There is significant retention of tracer in large areas after bronchoconstriction. Reproduced by permission from Reference 222. PET = positron emission tomography; $\dot{Q}$ = perfusion; $\dot{V}_A$ = alveolar ventilation.

model (301, 348, 354) (from a cumulative plot of $\dot{V}$ or $\dot{Q}$ vs. $\dot{V}_A/\dot{Q}$ ratio) binned in 50 equally spaced (log scale) compartments. $\dot{V}_A/\dot{Q}$ ratios <0.005 (shunt) and >100 (dead space) are separately calculated. Relative dispersion and gravitational gradients (348) may also be assessed.

Validation Approaches

Arterial O_2 and CO_2 tensions calculated from ^{13}NN PET–measured $\dot{V}_A/\dot{Q}$ distributions are highly correlated with arterial blood gases (222) and are consistent with data from the MIGET technique in normal, bronchoconstricted, pulmonary embolism, and pulmonary edema conditions (222, 223). MRI and SPECT measurements have been validated against MIGET (288, 301).

Caveats: Because estimates of $\dot{V}_A/\dot{Q}$ ratio in the ^{13}NN-saline bolus technique are specific to aerated and perfused regions, estimates of ventilation could be inaccurate in regions of alveolar dead space (e.g., pulmonary embolism). This can be addressed either by implementing a ^{13}NN-gas inhalation technique (358–360) or introducing additional terms to the model of ^{13}NN-saline bolus kinetics. Absolute ventilation at the voxel level can be computed from the product of regional (ventilation × gas volume) assessed by transmission scan or equilibration of inhaled ^{13}NN (222, 359). As SPECT quantifies relative $\dot{V}_A$ and relative perfusion, total $\dot{V}_A$ and perfusion must be separately measured for full quantification (288).

^{1}H MRI–derived regional $\dot{V}_A/\dot{Q}$ ratio is time consuming, requiring complex post-processing. The relationship between alveolar P_{O_2} and $\dot{V}_A/\dot{Q}$ ratio from HP ^{3}He MRI is insensitive at both high and low $\dot{V}_A/\dot{Q}$ ratios: large changes in local $\dot{V}_A/\dot{Q}$ ratio result in minimal changes in P_{O_2} in these regions, thereby limiting utility.

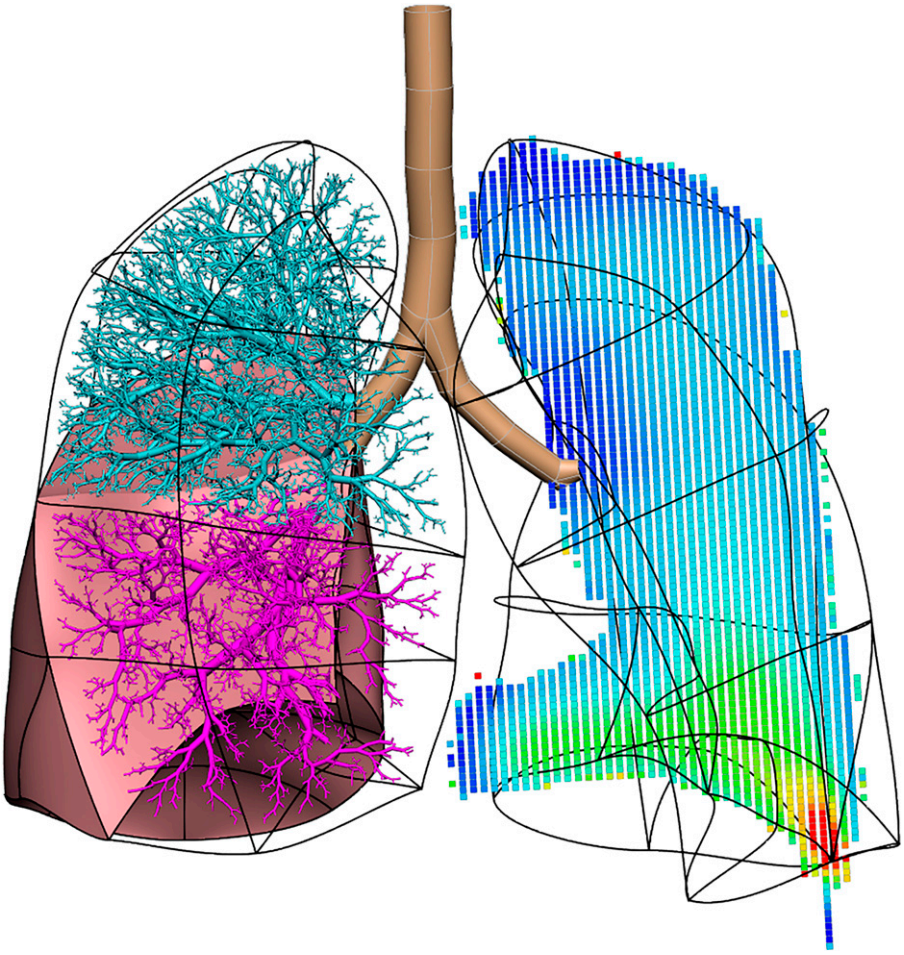

Figure 13. Illustration of computational models of lung structure and function. The right lung shows an imaging-based model of the human airway tree, reconstructed from volumetric computed tomography and a branch-filling tree generation method, placed within a finite element mesh. The left lung model is overlaid with a Jacobian (vector function) map showing regional parenchymal deformation calculated by coregistering paired images obtained at two lung volumes. Colors (from blue to green to red) in the left lung indicate increasing magnitudes of deformation from apex to the costophrenic sulcus. Courtesy of M. Tawhai.

Applying Imaging Metrics in Computational Modeling to Predict Lung Function

Modeling supports the acquisition, analysis, and interpretation of images while providing data to aid in the development and refinement of physiological models. Although imaging modalities provide information on regional ventilation, blood volumes, perfusion, $\dot{V}_A/\dot{Q}$ matching, and blood gas uptake, no method captures all the information simultaneously. The goal is to integrate data from different modalities, together with physiological measurements, to comprehensively characterize how structure determines function. Quantitative linking of structure and function in an intricate organ such as the lung can be done only through computational modeling on the basis of the laws of physics.

Respiratory diseases are complex and multifactorial, involving remodeling of tissue, airway, and vessel. This complicates interpretation of imaging-based metrics and limits the clinical utility of imaging biomarkers. Structure-based models (Figure 13) that include interactions among tissue, airway, and circulation can facilitate analysis and interpretation of how intersubject differences, imaging protocols, and normal or abnormal physiology contribute to imaging-based metrics. Carefully constructed models can be used to examine contributions of different factors (361) and provide mechanistic understanding far beyond that derived using statistical methods alone.

General Principles

Biophysical computational models can be used for forward simulations of function or inverse identification of system structure and parameters. Forward models are useful for sensitivity analyses (e.g., evaluating the contribution of normal subject variability to imaging metrics to define a threshold for abnormal) (362). Forward models can also predict emergent behavior in response to a parameter change at the cellular/tissue level (363). Inverse models are useful for deriving information that cannot be measured directly (e.g., distributions of airway or vascular obstruction that give rise to specific $\dot{V}_A/\dot{Q}$ patterns) (364). Both forward and inverse models can be used to analyze, interpret, and predict,

constrained by physical laws and physiological variables (e.g., cardiac output or respiratory rate).

The intimate structure–function relationships among tissue, airway, and circulation means that applications of modeling to imaging require models that include at least two of these components and their interactions. Models can be made more specific by using imaging and physiological data from individual patients. However, there is a limit to which the exact topology of airway and vasculature can be determined, and physiological parameters such as elasticity of the lung tissue or airway wall can only be estimated. It is critically important to understand the appropriate model to use for specific imaging analyses and their limitations (362).

Applications of Modeling to Imaging-Based Metrics

Conventional approaches to unifying data from different modalities use image registration to provide one-to-one voxel mapping and calculation of spatial correlation. Registration can be challenging when images are acquired in different anatomical planes, lung volumes, resolutions, or slice thicknesses. Statistical methods used to associate imaging with physiological and/or anthropometric data are limited in the mechanistic understanding they provide. Data can also be integrated by using a single unifying biophysical model to relate physiological measurements to imaging, as shown in studies that combine forward and inverse approaches to predict oscillatory lung mechanics in an airway tree model that is matched to images of ventilation defects (364–366). A realistic model of pulmonary perfusion has been used to duplicate an ASL MRI experiment for acquisition of pulmonary perfusion data to guide selection of thresholds for removing large-vessel signals that do not represent capillary perfusion (323).

Imaging-based metrics rely on assumptions underlying each imaging method, analysis, and interpretation. For example, ^{1}H MR–based SVI uses O_2 as a contrast agent, assuming that local lung tissue is in equilibrium with the surrounding alveolar P_{O_2}. The potential contribution of signal from O_2 carried in pulmonary vessels to SVI may be assessed (367) using a model that includes tissue mechanics, ventilation, perfusion, and gas exchange, to simulate the distribution and exchange of O_2 during SVI. By controlling the presence of signal from vessels, its impact on heterogeneity and perfusion gradient could be assessed. This model provides a simulated "ground truth" where the exact O_2 signal distribution in the circulation and tissue are both known. The model-generated image can be "voxelized" and postprocessed as virtual image data. Assumptions in imaging or analysis methods can be tested by comparing derived metrics with the model ground truth.

Imaging-based biomarkers based on statistical relationships between imaging features and clinical outcomes are insufficient to understand the complexity of interactions that underlie measurable or imageable function. For example, several imaging-based vascular metrics (ratio of PA to ascending aorta diameter, diameter and volume of proximal arteries, volume of small arteries, and microvascular blood flow and heterogeneity) are emerging as potential biomarkers for disease severity. Although these metrics are interrelated, it is difficult to examine their physiological interrelationships from imaging alone; this represents a prime example in which image-based model analysis plays a central role. Biophysical models can be time consuming to construct and execute, but when well-designed and appropriately used, they provide a sophisticated tool to complement imaging.

Conclusions

QI continues to evolve with advances in hardware and software capabilities. The major imaging modalities described above offer complementary structure–function data. Despite high-precision measurements, effective use of QI to enhance understanding of respiratory (patho)physiology critically depends on following robust study design and unbiased sampling. This ensures accurate representation of the structures and selection of validated meaningful metrics, facilitating understanding of the capabilities and limitations of each modality and analytical approach and aiding appropriate interpretation of the results in correlation with anatomical and clinicophysiological biomarkers. As *in vivo* validation of imaging-derived metrics remains empirical, computational modeling plays an important role in elucidating the mechanisms underlying the imaged perturbations. ■

This official document was developed by an *ad hoc* subcommittee of the ATS and the Fleischner Society.

Members of the subcommittee are as follows:

Connie C. W. Hsia, M.D. (*Co-Chair*)[1]
Susan R. Hopkins, M.D., Ph.D. (*Co-Chair*)[2]
Jason H. T. Bates, Ph.D.[3]*
Bastiaan Driehuys, Ph.D.[4]*
Sean B. Fain, Ph.D.[5]*
Jonathan G. Goldin, M.D.[6]
Eric A. Hoffman, Ph.D.[5]*
James C. Hogg, M.D., Ph.D.[7]
David L. Levin, M.D., Ph.D[8]*
David A. Lynch, M.D.[9]*
Matthias Ochs, M.D.[10]*
Grace Parraga, Ph.D.[11]*
G. Kim Prisk, Ph.D.[2]*
Benjamin M. Smith, M.D.[12,13]*
Merryn Tawhai, Ph.D.[14]*
Marcos F. Vidal Melo, M.D., Ph.D.[13]*
Jason C. Woods, Ph.D.[15]*

[1]University of Texas Southwestern Medical Center, Dallas, Texas; [2]University of California, San Diego, San Diego, California; [3]University of Vermont, Burlington, Vermont; [4]School of Medicine, Duke University, Durham, North Carolina; [5]University of Iowa, Iowa City, Iowa; [6]University of California, Los Angeles, Los Angeles, California; [7]University of British Columbia, Vancouver, British Columbia, Canada; [8]Mayo Clinic, Rochester, Minnesota; [9]National Jewish Health, Denver, Colorado; [10]Charité – Universitätsmedizin Berlin, Berlin, Germany; [11]Western University, London, Ontario, Canada; [12]McGill University, Montreal, Quebec, Canada; [13]Columbia University, New York, New York; [14]University of Auckland, Auckland, New Zealand; and [15]Cincinnati Children's Medical Center, Cincinnati, Ohio

*Writing committee.

Author Disclosures: C.C.W.H. served as a consultant for Ono Pharmaceutical; served as a consultant (spouse/partner) for Allena Pharmaceuticals, Alnylam, Applied Therapeutics, Dicerna, Tricida; holds patent #10912791 and patent #11491115; received research support from ATyr Pharmaceutical, Kinevant Sciences, Mallinckrodt Pharmaceuticals, NIH-NHLBI, and Department of Defense. J.H.T.B. served on advisory committee and has financial stakes in Oscillavent; served as a consultant for Oscillavent, Healthy Design, Johnson & Johnson, Respiratory Sciences, Chiesi; employed by Healthy Design; received research support from NHLBI. B.D. holds unsold intellectual property, royalties, stock/stock options, leadership or fiduciary role, and served as a consultant for Polarean Imaging; received research support from Astra Zeneca, Boehringer Ingelheim, Genentech, NHLBI, United Therapeutics. S.B.F served on advisory committee for GE Healthcare; served as consultant for COPD Gene, Polarean, Sanofi/Regneron; served as co-chair for QIBA RSNA; received research support from GE Healthcare, Siemens; was a speaker for Genentech, Polarean, Sanofi/Regeneron.

J.G.G. served as a consultant for Boehringer Ingelheim; has financial stake in and is founder of MedQIA, LLC. E.A.H. served on a photon counting advisory committee for Siemens Healthineers; founder and shareholder of VIDA Diagnostics; received research support from NIH. D.L.L. served on advisory committee for Imagen Technologies, Inc. D.A.L. served on advisory committee, as speaker, and as consultant for Boehringer Ingelheim; served on advisory committee for Bristol Myers Squibb and Polarean; served as a consultant for Acceleron, Astra Zeneca, Calyx Imaging, Daiichi Sankyo, Parexel, Siemens, and Veracyte; holds patent #10706533, System and method for automatic detection and quantification of pathology using dynamic feature classification; received research support from NHLBI. G.K.P. is associate editor with American Physiological Society; holds patent #9750427; received research support from NIH. B.M.S. received research support from Canadian Institutes of Health Research, Canadian Lung Association, McGill Health Centre Foundation, NIH, and Quebec Health Research Fund. M.T. received research support from NIH. M.F.V.M. received research support from NIH-NHLBI. J.C.W. served as a consultant for Polarean; served as a consultant and received research support from Vertex. S.R.H. is employee (spouse/partner) of Thermofisher; has ownership or investment interests in General Electric; holds patent #9750427; received research support from NIH-NHLBI. J.C.H., M.O., G.P. reported no commercial or relevant non-commercial interests from ineligible companies.

References

1 Kim GHJ, Goldin JG, Hayes W, Oh A, Soule B, Du S. The value of imaging and clinical outcomes in a phase II clinical trial of a lysophosphatidic acid receptor antagonist in idiopathic pulmonary fibrosis. *Ther Adv Respir Dis* 2021;15:17534666211004238.

2 Raghu G, Scholand MB, de Andrade J, Lancaster L, Mageto Y, Goldin J, *et al.* FG-3019 anti-connective tissue growth factor monoclonal antibody: results of an open-label clinical trial in idiopathic pulmonary fibrosis. *Eur Respir J* 2016;47:1481–1491.

3 Chen-Mayer HH, Fuld MK, Hoppel B, Judy PF, Sieren JP, Guo J, *et al.* Standardizing CT lung density measure across scanner manufacturers. *Med Phys* 2017;44:974–985.

4 Berta L, Rizzetto F, De Mattia C, Lizio D, Felisi M, Colombo PE, *et al.*; Niguarda COVID-19 Working Group. Automatic lung segmentation in COVID-19 patients: impact on quantitative computed tomography analysis. *Phys Med* 2021;87:115–122.

5 Hopkins SR, Henderson AC, Levin DL, Yamada K, Arai T, Buxton RB, *et al.* Vertical gradients in regional lung density and perfusion in the supine human lung: the Slinky effect. *J Appl Physiol (1985)* 2007;103: 240–248.

6 Glazier JB, Hughes JM, Maloney JE, Pain MC, West JB. Vertical gradient of alveolar size in dog lungs frozen in situ. *J Physiol* 1966; 186:114P–115P.

7 Glazier JB, Hughes JM, Maloney JE, Pain MC, West JB. Decreasing alveolar size from apex to base in the upright lung. *Lancet* 1966;2: 203–204.

8 Glazier JB, Hughes JM, Maloney JE, West JB. Vertical gradient of alveolar size in lungs of dogs frozen intact. *J Appl Physiol* 1967;23: 694–705.

9 West JB, Glazier JB, Hughes JM, Maloney JE. Effect of gravity on the morphology of pulmonary capillaries and alveoli. *Aspen Emphysema Conf* 1968;11:135–137.

10 Hoffman EA. Effect of body orientation on regional lung expansion: a computed tomographic approach. *J Appl Physiol (1985)* 1985;59: 468–480.

11 Hopkins SR, Arai TJ, Henderson AC, Levin DL, Buxton RB, Kim Prisk G. Lung volume does not alter the distribution of pulmonary perfusion in dependent lung in supine humans. *J Physiol* 2010;588:4759–4768.

12 Musch G, Layfield JD, Harris RS, Melo MF, Winkler T, Callahan RJ, *et al.* Topographical distribution of pulmonary perfusion and ventilation, assessed by PET in supine and prone humans. *J Appl Physiol (1985)* 2002;93:1841–1851.

13 Tawhai MH, Nash MP, Lin C-L, Hoffman EA. Supine and prone differences in regional lung density and pleural pressure gradients in the human lung with constant shape. *J Appl Physiol (1985)* 2009;107:912–920.

14 Gattinoni L, Taccone P, Carlesso E, Marini JJ. Prone position in acute respiratory distress syndrome. Rationale, indications, and limits. *Am J Respir Crit Care Med* 2013;188:1286–1293.

15 Moreno F, Lyons HA. Effect of body posture on lung volumes. *J Appl Physiol* 1961;16:27–29.

16 Whitfield A, Waterhouse J, Arnott WM. The total lung volume and its subdivisions: II. The effect of posture. *Br J Soc Med* 1950;4:86.

17 Gefter WB, Lee KS, Schiebler ML, Parraga G, Seo JB, Ohno Y, *et al.* Pulmonary functional imaging: part 2—state-of-the-art clinical applications and opportunities for improved patient care. *Radiology* 2021;299:524–538.

18 Hatabu H, Ohno Y, Gefter WB, Parraga G, Madore B, Lee KS, *et al.*; Fleischner Society. Expanding applications of pulmonary MRI in the clinical evaluation of lung disorders: Fleischner Society position paper. *Radiology* 2020;297:286–301.

19 Bluemke DA, Moy L, Bredella MA, Ertl-Wagner BB, Fowler KJ, Goh VJ, *et al.* Assessing radiology research on artificial intelligence: a brief guide for authors, reviewers, and readers—from the *Radiology* editorial board. *Radiology* 2020;294:487–489.

20 Hsia CC, Hyde DM, Ochs M, Weibel ER; ATS/ERS Joint Task Force on Quantitative Assessment of Lung Structure. An official research policy statement of the American Thoracic Society/European Respiratory Society: standards for quantitative assessment of lung structure. *Am J Respir Crit Care Med* 2010;181:394–418.

21 Ochs M, Schipke J. A short primer on lung stereology. *Respir Res* 2021; 22:305.

22 Cruz-Orive LM, Weibel ER. Recent stereological methods for cell biology: a brief survey. *Am J Physiol* 1990;258:L148–L156.

23 Bolender RP, Hyde DM, Dehoff RT. Lung morphometry: a new generation of tools and experiments for organ, tissue, cell, and molecular biology. *Am J Physiol* 1993;265:L521–L548.

24 Mühlfeld C, Knudsen L, Ochs M. Stereology and morphometry of lung tissue. *Methods Mol Biol* 2013;931:367–390.

25 Ochs M, Mühlfeld C. Quantitative microscopy of the lung: a problem-based approach. Part 1: basic principles of lung stereology. *Am J Physiol Lung Cell Mol Physiol* 2013;305:L15–L22.

26 Yablonskiy DA, Sukstanskii AL, Quirk JD. Diffusion lung imaging with hyperpolarized gas MRI. *NMR Biomed* 2017;30:10.1002/nbm.3448.

27 Sills RC, Johnson GA, Anderson RJ, Johnson CL, Staup M, Brown DL, *et al.* Qualitative and quantitative neuropathology approaches using magnetic resonance microscopy (diffusion tensor imaging) and stereology in a hexachlorophene model of myelinopathy in Sprague-Dawley rats. *Toxicol Pathol* 2020;48:965–980.

28 Defres S, Keller SS, Das K, Vidyasagar R, Parkes LM, Burnside G, *et al.*; ENCEPH UK study group. A feasibility study of quantifying longitudinal brain changes in herpes simplex virus (HSV) encephalitis using magnetic resonance imaging (MRI) and stereology. *PLoS ONE* 2017;12:e0170215.

29 Ekinci N, Acer N, Akkaya A, Sankur S, Kabadayi T, Sahin B. Volumetric evaluation of the relations among the cerebrum, cerebellum and brain stem in young subjects: a combination of stereology and magnetic resonance imaging. *Surg Radiol Anat* 2008;30:489–494.

30 Doherty CP, Fitzsimons M, Holohan T, Mohamed HB, Farrell M, Meredith GE, *et al.* Accuracy and validity of stereology as a quantitative method for assessment of human temporal lobe volumes acquired by magnetic resonance imaging. *Magn Reson Imaging* 2000;18:1017–1025.

31 Mazonakis M, Pagonidis K, Damilakis J. Right ventricular volumes and ejection fraction by MR imaging and stereology: comparison with standard image analysis method. *Clin Anat* 2011;24:868–873.

32 Kizhakke Puliyakote AS, Vasilescu DM, Newell JD Jr, Wang G, Weibel ER, Hoffman EA. Morphometric differences between central vs. surface acini in A/J mice using high-resolution micro-computed tomography. *J Appl Physiol (1985)* 2016;121:115–122.

33 Vasilescu DM, Martinez FJ, Marchetti N, Galbán CJ, Hatt C, Meldrum CA, *et al.* Noninvasive imaging biomarker identifies small airway damage in severe chronic obstructive pulmonary disease. *Am J Respir Crit Care Med* 2019;200:575–581.
34 van Stralen KJ, Stel VS, Reitsma JB, Dekker FW, Zoccali C, Jager KJ. Diagnostic methods I: sensitivity, specificity, and other measures of accuracy. *Kidney Int* 2009;75:1257–1263.
35 Mayhew TM. Taking tissue samples from the placenta: an illustration of principles and strategies. *Placenta* 2008;29:1–14.
36 Gundersen HJ, Osterby R. Optimizing sampling efficiency of stereological studies in biology: or 'do more less well!' *J Microsc* 1981;121:65–73.
37 Weibel ER, Hsia CC, Ochs M. How much is there really? Why stereology is essential in lung morphometry. *J Appl Physiol (1985)* 2007;102:459–467.
38 Gardi JE, Nyengaard JR, Gundersen HJ. Automatic sampling for unbiased and efficient stereological estimation using the proportionator in biological studies. *J Microsc* 2008;230:108–120.
39 Hsia CC, Hyde DM, Ochs M, Weibel ER. How to measure lung structure—what for? On the "Standards for the quantitative assessment of lung structure." *Respir Physiol Neurobiol* 2010;171: 72–74.
40 Braendgaard H, Gundersen HJ. The impact of recent stereological advances on quantitative studies of the nervous system. *J Neurosci Methods* 1986;18:39–78.
41 Yan X, Polo Carbayo JJ, Weibel ER, Hsia CC. Variation of lung volume after fixation when measured by immersion or Cavalieri method. *Am J Physiol Lung Cell Mol Physiol* 2003;284:L242–L245.
42 Vasilescu DM, Klinge C, Knudsen L, Yin L, Wang G, Weibel ER, *et al.* Stereological assessment of mouse lung parenchyma via nondestructive, multiscale micro-CT imaging validated by light microscopic histology. *J Appl Physiol (1985)* 2013;114:716–724.
43 Vasilescu DM, Gao Z, Saha PK, Yin L, Wang G, Haefeli-Bleuer B, *et al.* Assessment of morphometry of pulmonary acini in mouse lungs by nondestructive imaging using multiscale microcomputed tomography. *Proc Natl Acad Sci U S A* 2012;109:17105–17110.
44 Bontzos G, Mazonakis M, Papadaki E, Maris TG, Blazaki S, Drakonaki EE, *et al.* Ex vivo orbital volumetry using stereology and CT imaging: a comparison with manual planimetry. *Eur Radiol* 2019; 29:1365–1374.
45 Manios GE, Mazonakis M, Voulgaris C, Karantanas A, Damilakis J. Abdominal fat volume estimation by stereology on CT: a comparison with manual planimetry. *Eur Radiol* 2016;26:706–713.
46 Mayhew TM, Mühlfeld C, Vanhecke D, Ochs M. A review of recent methods for efficiently quantifying immunogold and other nanoparticles using TEM sections through cells, tissues and organs. *Ann Anat* 2009;191:153–170.
47 Mascalchi M, Camiciottoli G, Diciotti S. Lung densitometry: why, how and when. *J Thorac Dis* 2017;9:3319–3345.
48 Sieren JP, Newell JD, Judy PF, Lynch DA, Chan KS, Guo J, *et al.* Reference standard and statistical model for intersite and temporal comparisons of CT attenuation in a multicenter quantitative lung study. *Med Phys* 2012;39:5757–5767.
49 Quantitative Imaging Biomarkers Alliance. QIBA profile: computed tomography: lung densitometry. Oak Brook, IL: Radiological Society of North America; 2019 [updated 2020; accessed 2022 July 1]. Available from: https://qibawiki.rsna.org/images/a/a8/QIBA_CT_Lung_Density_Profile_090420-clean.pdf.
50 Hoffman EA, Sinak LJ, Robb RA, Ritman EL. Noninvasive quantitative imaging of shape and volume of lungs. *J Appl Physiol* 1983;54: 1414–1421.
51 Ukil S, Reinhardt JM. Anatomy-guided lung lobe segmentation in X-ray CT images. *IEEE Trans Med Imaging* 2009;28:202–214.
52 Coxson HO, Mayo JR, Behzad H, Moore BJ, Verburgt LM, Staples CA, *et al.* Measurement of lung expansion with computed tomography and comparison with quantitative histology. *J Appl Physiol (1985)* 1995; 79:1525–1530.
53 Yilmaz C, Dane DM, Patel NC, Hsia CC. Quantifying heterogeneity in emphysema from high-resolution computed tomography: a lung tissue research consortium study. *Acad Radiol* 2013;20:181–193.
54 Yilmaz C, Watharkar SS, Diaz de Leon A, Garcia CK, Patel NC, Jordan KG, *et al.* Quantification of regional interstitial lung disease from CT-derived fractional tissue volume: a lung tissue research consortium study. *Acad Radiol* 2011;18:1014–1023.
55 Ravikumar P, Yilmaz C, Dane DM, Johnson RL Jr, Estrera AS, Hsia CC. Regional lung growth following pneumonectomy assessed by computed tomography. *J Appl Physiol (1985)* 2004;97:1567–1574. [Discussion, p. 1549].
56 Won C, Chon D, Tajik J, Tran BQ, Robinswood GB, Beck KC, *et al.* CT-based assessment of regional pulmonary microvascular blood flow parameters. *J Appl Physiol (1985)* 2003;94:2483–2493.
57 Wielpütz MO, Bardarova D, Weinheimer O, Kauczor HU, Eichinger M, Jobst BJ, *et al.* Variation of densitometry on computed tomography in COPD—influence of different software tools. *PLoS ONE* 2014;9: e112898.
58 Gerard SE, Patton TJ, Christensen GE, Bayouth JE, Reinhardt JM. FissureNet: a deep learning approach for pulmonary fissure detection in CT images. *IEEE Trans Med Imaging* 2019;38:156–166.
59 Konietzke P, Weinheimer O, Wielpütz MO, Savage D, Ziyeh T, Tu C, *et al.* Validation of automated lobe segmentation on paired inspiratory-expiratory chest CT in 8-14 year-old children with cystic fibrosis. *PLoS ONE* 2018;13:e0194557.
60 Madani A, Van Muylem A, Gevenois PA. Pulmonary emphysema: effect of lung volume on objective quantification at thin-section CT. *Radiology* 2010;257:260–268.
61 Rienmüller RK, Behr J, Kalender WA, Schätzl M, Altmann I, Merin M, *et al.* Standardized quantitative high resolution CT in lung diseases. *J Comput Assist Tomogr* 1991;15:742–749.
62 Kalender WA, Rienmüller R, Seissler W, Behr J, Welke M, Fichte H. Measurement of pulmonary parenchymal attenuation: use of spirometric gating with quantitative CT. *Radiology* 1990;175:265–268.
63 Fuld MK, Grout RW, Guo J, Morgan JH, Hoffman EA. Systems for lung volume standardization during static and dynamic MDCT-based quantitative assessment of pulmonary structure and function. *Acad Radiol* 2012;19:930–940.
64 Iyer KS, Grout RW, Zamba GK, Hoffman EA. Repeatability and sample size assessment associated with computed tomography-based lung density metrics. *Chronic Obstr Pulm Dis (Miami)* 2014;1: 97–104.
65 Kaminsky DA, Irvin CG, Lundblad LK, Thompson-Figueroa J, Klein J, Sullivan MJ, *et al.* Heterogeneity of bronchoconstriction does not distinguish mild asthmatic subjects from healthy controls when supine. *J Appl Physiol (1985)* 2008;104:10–19.
66 Clukers J, Lanclus M, Mignot B, Van Holsbeke C, Roseman J, Porter S, *et al.* Quantitative CT analysis using functional imaging is superior in describing disease progression in idiopathic pulmonary fibrosis compared to forced vital capacity. *Respir Res* 2018;19:213.
67 Iyer KS, Newell JD Jr, Jin D, Fuld MK, Saha PK, Hansdottir S, *et al.* Quantitative dual-energy computed tomography supports a vascular etiology of smoking-induced inflammatory lung disease. *Am J Respir Crit Care Med* 2016;193:652–661.
68 Pontana F, Faivre JB, Remy-Jardin M, Flohr T, Schmidt B, Tacelli N, *et al.* Lung perfusion with dual-energy multidetector-row CT (MDCT): feasibility for the evaluation of acute pulmonary embolism in 117 consecutive patients. *Acad Radiol* 2008;15:1494–1504.
69 Jahani N, Choi S, Choi J, Iyer K, Hoffman EA, Lin CL. Assessment of regional ventilation and deformation using 4D-CT imaging for healthy human lungs during tidal breathing. *J Appl Physiol (1985)* 2015;119: 1064–1074.
70 Camiciottoli G, Bigazzi F, Bartolucci M, Cestelli L, Paoletti M, Diciotti S, *et al.* BODE-index, modified BODE-index and ADO-score in chronic obstructive pulmonary disease: relationship with COPD phenotypes and CT lung density changes. *COPD* 2012;9:297–304.
71 Müller NL, Staples CA, Miller RR, Abboud RT. "Density mask": an objective method to quantitate emphysema using computed tomography. *Chest* 1988;94:782–787.
72 Gevenois PA, De Vuyst P, de Maertelaer V, Zanen J, Jacobovitz D, Cosio MG, *et al.* Comparison of computed density and microscopic morphometry in pulmonary emphysema. *Am J Respir Crit Care Med* 1996;154:187–192.
73 Gevenois PA, de Maertelaer V, De Vuyst P, Zanen J, Yernault JC. Comparison of computed density and macroscopic morphometry in pulmonary emphysema. *Am J Respir Crit Care Med* 1995;152: 653–657.

74 Madani A, Zanen J, de Maertelaer V, Gevenois PA. Pulmonary emphysema: objective quantification at multi-detector row CT—comparison with macroscopic and microscopic morphometry. *Radiology* 2006;238:1036–1043.
75 Wang Z, Gu S, Leader JK, Kundu S, Tedrow JR, Sciurba FC, *et al.* Optimal threshold in CT quantification of emphysema. *Eur Radiol* 2013;23:975–984.
76 den Harder AM, de Boer E, Lagerweij SJ, Boomsma MF, Schilham AMR, Willemink MJ, *et al.* Emphysema quantification using chest CT: influence of radiation dose reduction and reconstruction technique. *Eur Radiol Exp* 2018;2:30.
77 Ashraf H, Lo P, Shaker SB, de Bruijne M, Dirksen A, Tønnesen P, *et al.* Short-term effect of changes in smoking behaviour on emphysema quantification by CT. *Thorax* 2011;66:55–60.
78 Coxson HO, Dirksen A, Edwards LD, Yates JC, Agusti A, Bakke P, *et al.*; Evaluation of COPD Longitudinally to Identify Predictive Surrogate Endpoints (ECLIPSE) Investigators. The presence and progression of emphysema in COPD as determined by CT scanning and biomarker expression: a prospective analysis from the ECLIPSE study. *Lancet Respir Med* 2013;1:129–136.
79 Dirksen A, Piitulainen E, Parr DG, Deng C, Wencker M, Shaker SB, *et al.* Exploring the role of CT densitometry: a randomised study of augmentation therapy in alpha1-antitrypsin deficiency. *Eur Respir J* 2009;33:1345–1353.
80 Konheim JA, Kon ZN, Pasrija C, Luo Q, Sanchez PG, Garcia JP, *et al.* Predictive equations for lung volumes from computed tomography for size matching in pulmonary transplantation. *J Thorac Cardiovasc Surg* 2016;151:1163–1169.e1.
81 Robbie H, Wells AU, Jacob J, Walsh SLF, Nair A, Srikanthan A, *et al.* Visual and automated CT measurements of lung volume loss in idiopathic pulmonary fibrosis. *AJR Am J Roentgenol* 2019;213:318–324.
82 Walsdorff M, Van Muylem A, Gevenois PA. Effect of total lung capacity and gender on CT densitometry indexes. *Br J Radiol* 2016;89: 20150631.
83 Hersh CP, Washko GR, Estépar RS, Lutz S, Friedman PJ, Han MK, *et al.*; COPDGene Investigators. Paired inspiratory-expiratory chest CT scans to assess for small airways disease in COPD. *Respir Res* 2013;14:42.
84 Gu S, Leader J, Zheng B, Chen Q, Sciurba F, Kminski N, *et al.* Direct assessment of lung function in COPD using CT densitometric measures. *Physiol Meas* 2014;35:833–845.
85 Schroeder JD, McKenzie AS, Zach JA, Wilson CG, Curran-Everett D, Stinson DS, *et al.* Relationships between airflow obstruction and quantitative CT measurements of emphysema, air trapping, and airways in subjects with and without chronic obstructive pulmonary disease. *AJR Am J Roentgenol* 2013;201:W460–W470.
86 Garfield JL, Marchetti N, Gaughan JP, Steiner RM, Criner GJ. Total lung capacity by plethysmography and high-resolution computed tomography in COPD. *Int J Chron Obstruct Pulmon Dis* 2012;7:119–126.
87 O'Donnell CR, Bankier AA, Stiebellehner L, Reilly JJ, Brown R, Loring SH. Comparison of plethysmographic and helium dilution lung volumes: which is best for COPD? *Chest* 2010;137:1108–1115.
88 Brown R, Ingram RH Jr, McFadden ER Jr. Problems in the plethysmographic assessment of changes in total lung capacity in asthma. *Am Rev Respir Dis* 1978;118:685–692.
89 Rodenstein DO, Stănescu DC, Francis C. Demonstration of failure of body plethysmography in airway obstruction. *J Appl Physiol* 1982;52: 949–954.
90 Hansell DM. Small airways diseases: detection and insights with computed tomography. *Eur Respir J* 2001;17:1294–1313.
91 Abbott GF, Rosado-de-Christenson ML, Rossi SE, Suster S. Imaging of small airways disease. *J Thorac Imaging* 2009;24:285–298.
92 Kirby M, Yin Y, Tschirren J, Tan WC, Leipsic J, Hague CJ, *et al.*; CanCOLD Collaborative Research Group and the Canadian Respiratory Research Network. A novel method of estimating small airway disease using inspiratory-to-expiratory computed tomography. *Respiration* 2017;94:336–345.
93 Chen A, Karwoski RA, Gierada DS, Bartholmai BJ, Koo CW. Quantitative CT analysis of diffuse lung disease. *Radiographics* 2020; 40:28–43.
94 Belloli EA, Degtiar I, Wang X, Yanik GA, Stuckey LJ, Verleden SE, *et al.* Parametric response mapping as an imaging biomarker in lung transplant recipients. *Am J Respir Crit Care Med* 2017;195: 942–952.
95 Pompe E, Galbán CJ, Ross BD, Koenderman L, Ten Hacken NH, Postma DS, *et al.* Parametric response mapping on chest computed tomography associates with clinical and functional parameters in chronic obstructive pulmonary disease. *Respir Med* 2017;123:48–55.
96 Labaki WW, Gu T, Murray S, Hatt CR, Galbán CJ, Ross BD, *et al.* Reprint of: Voxel-wise longitudinal parametric response mapping analysis of chest computed tomography in smokers. *Acad Radiol* 2019;26:306–312.
97 Hwang HJ, Seo JB, Lee SM, Kim N, Yi J, Lee JS, *et al.* New method for combined quantitative assessment of air-trapping and emphysema on chest computed tomography in chronic obstructive pulmonary disease: comparison with parametric response mapping. *Korean J Radiol* 2021;22:1719–1729.
98 Criner RN, Hatt CR, Galbán CJ, Kazerooni EA, Lynch DA, McCormack MC, *et al.* Relationship between diffusion capacity and small airway abnormality in COPDGene. *Respir Res* 2019;20:269.
99 Galbán CJ, Han MK, Boes JL, Chughtai KA, Meyer CR, Johnson TD, *et al.* Computed tomography-based biomarker provides unique signature for diagnosis of COPD phenotypes and disease progression. *Nat Med* 2012;18:1711–1715.
100 Ostridge K, Gove K, Paas KHW, Burke H, Freeman A, Harden S, *et al.* Using novel computed tomography analysis to describe the contribution and distribution of emphysema and small airways disease in chronic obstructive pulmonary disease. *Ann Am Thorac Soc* 2019;16:990–997.
101 Hansell DM, Goldin JG, King TE Jr, Lynch DA, Richeldi L, Wells AU. CT staging and monitoring of fibrotic interstitial lung diseases in clinical practice and treatment trials: a position paper from the Fleischner Society. *Lancet Respir Med* 2015;3:483–496.
102 Lederer DJ, Enright PL, Kawut SM, Hoffman EA, Hunninghake G, van Beek EJ, *et al.* Cigarette smoking is associated with subclinical parenchymal lung disease: the Multi-Ethnic Study of Atherosclerosis (MESA)–Lung study. *Am J Respir Crit Care Med* 2009;180:407–414.
103 Humphries SM, Swigris JJ, Brown KK, Strand M, Gong Q, Sundy JS, *et al.* Quantitative high-resolution computed tomography fibrosis score: performance characteristics in idiopathic pulmonary fibrosis. *Eur Respir J* 2018;52:1801384.
104 Kim HJ, Brown MS, Chong D, Gjertson DW, Lu P, Kim HJ, *et al.* Comparison of the quantitative CT imaging biomarkers of idiopathic pulmonary fibrosis at baseline and early change with an interval of 7 months. *Acad Radiol* 2015;22:70–80.
105 Diaz de Leon A, Cronkhite JT, Yilmaz C, Brewington C, Wang R, Xing C, *et al.* Subclinical lung disease, macrocytosis, and premature graying in kindreds with telomerase (TERT) mutations. *Chest* 2011; 140:753–763.
106 Lubner MG, Smith AD, Sandrasegaran K, Sahani DV, Pickhardt PJ. CT texture analysis: definitions, applications, biologic correlates, and challenges. *Radiographics* 2017;37:1483–1503.
107 Goldin JG, Kim GHJ, Tseng CH, Volkmann E, Furst D, Clements P, *et al.* Longitudinal changes in quantitative interstitial lung disease on computed tomography after immunosuppression in the Scleroderma Lung Study II. *Ann Am Thorac Soc* 2018;15:1286–1295.
108 Sørensen L, Nielsen M, Lo P, Ashraf H, Pedersen JH, de Bruijne M. Texture-based analysis of COPD: a data-driven approach. *IEEE Trans Med Imaging* 2012;31:70–78.
109 Uppaluri R, Hoffman EA, Sonka M, Hartley PG, Hunninghake GW, McLennan G. Computer recognition of regional lung disease patterns. *Am J Respir Crit Care Med* 1999;160:648–654.
110 Uppaluri R, Hoffman EA, Sonka M, Hunninghake GW, McLennan G. Interstitial lung disease: a quantitative study using the adaptive multiple feature method. *Am J Respir Crit Care Med* 1999;159:519–525.
111 Xu Y, van Beek EJ, Hwanjo Y, Guo J, McLennan G, Hoffman EA. Computer-aided classification of interstitial lung diseases via MDCT: 3D adaptive multiple feature method (3D AMFM). *Acad Radiol* 2006; 13:969–978.
112 Wu X, Kim GH, Salisbury ML, Barber D, Bartholmai BJ, Brown KK, *et al.* Computed tomographic biomarkers in idiopathic pulmonary fibrosis: the future of quantitative analysis. *Am J Respir Crit Care Med* 2019; 199:12–21.

113 Humphries SM, Yagihashi K, Huckleberry J, Rho BH, Schroeder JD, Strand M, *et al.* Idiopathic pulmonary fibrosis: data-driven textural analysis of extent of fibrosis at baseline and 15-month follow-up. *Radiology* 2017;285:270–278.

114 Park HJ, Lee SM, Song JW, Lee SM, Oh SY, Kim N, *et al.* Texture-based automated quantitative assessment of regional patterns on initial CT in patients with idiopathic pulmonary fibrosis: relationship to decline in forced vital capacity. *AJR Am J Roentgenol* 2016;207: 976–983.

115 Bell LC, Johnson KM, Fain SB, Wentland A, Drees R, Johnson RA, *et al.* Simultaneous MRI of lung structure and perfusion in a single breathhold. *J Magn Reson Imaging* 2015;41:52–59.

116 Johnson KM, Fain SB, Schiebler ML, Nagle S. Optimized 3D ultrashort echo time pulmonary MRI. *Magn Reson Med* 2013;70: 1241–1250.

117 Torres L, Kammerman J, Hahn AD, Zha W, Nagle SK, Johnson K, *et al.* Structure-function imaging of lung disease using ultrashort echo time MRI. *Acad Radiol* 2019;26:431–441.

118 Leawoods JC, Yablonsky DA, Saam B, Gierada DS, Conradi MS. Hyperpolarized ^{3}He gas production and MR imaging of the lung. *Concepts Magn Reson* 2001;13:277–293.

119 Albert MS, Cates GD, Driehuys B, Happer W, Saam B, Springer CS Jr, *et al.* Biological magnetic resonance imaging using laser-polarized ^{129}Xe. *Nature* 1994;370:199–201.

120 Saam B. T1 relaxation of ^{129}Xe and how to keep it long. In: Meersmann T, Brunner E, editors. Hyperpolarized xenon-129 magnetic resonance: concepts, production, techniques and applications. London: The Royal Society of Chemistry; 2015. pp. 122–141.

121 Gierada DS, Woods JC, Bierhals AJ, Bartel ST, Ritter JH, Choong CK, *et al.* Effects of diffusion time on short-range hyperpolarized ^{3}He diffusivity measurements in emphysema. *J Magn Reson Imaging* 2009;30:801–808.

122 Hajari AJ, Yablonskiy DA, Quirk JD, Sukstanskii AL, Pierce RA, Deslée G, *et al.* Imaging alveolar-duct geometry during expiration via ^{3}He lung morphometry. *J Appl Physiol (1985)* 2011;110:1448–1454.

123 Hajari AJ, Yablonskiy DA, Sukstanskii AL, Quirk JD, Conradi MS, Woods JC. Morphometric changes in the human pulmonary acinus during inflation. *J Appl Physiol (1985)* 2012;112:937–943.

124 Quirk JD, Lutey BA, Gierada DS, Woods JC, Senior RM, Lefrak SS, *et al.* In vivo detection of acinar microstructural changes in early emphysema with ^{3}He lung morphometry. *Radiology* 2011;260: 866–874.

125 Yablonskiy DA, Sukstanskii AL, Woods JC, Gierada DS, Quirk JD, Hogg JC, *et al.* Quantification of lung microstructure with hyperpolarized ^{3}He diffusion MRI. *J Appl Physiol (1985)* 2009;107:1258–1265.

126 Emami K, Stephen M, Kadlecek S, Cadman RV, Ishii M, Rizi RR. Quantitative assessment of lung using hyperpolarized magnetic resonance imaging. *Proc Am Thorac Soc* 2009;6:431–438.

127 Cereda M, Emami K, Kadlecek S, Xin Y, Mongkolwisetwara P, Profka H, *et al.* Quantitative imaging of alveolar recruitment with hyperpolarized gas MRI during mechanical ventilation. *J Appl Physiol (1985)* 2011; 110:499–511.

128 Kirby M, Owrangi A, Svenningsen S, Wheatley A, Coxson HO, Paterson NA, *et al.* On the role of abnormal DL(CO) in ex-smokers without airflow limitation: symptoms, exercise capacity and hyperpolarised helium-3 MRI. *Thorax* 2013;68:752–759.

129 Yablonskiy DA, Sukstanskii AL, Quirk JD, Woods JC, Conradi MS. Probing lung microstructure with hyperpolarized noble gas diffusion MRI: theoretical models and experimental results. *Magn Reson Med* 2014;71:486–505.

130 Wang W, Nguyen NM, Guo J, Woods JC. Longitudinal, noninvasive monitoring of compensatory lung growth in mice after pneumonectomy via ^{3}He and ^{1}H magnetic resonance imaging. *Am J Respir Cell Mol Biol* 2013;49:697–703.

131 Wang W, Nguyen NM, Agapov E, Holtzman MJ, Woods JC. Monitoring in vivo changes in lung microstructure with ^{3}He MRI in Sendai virus-infected mice. *J Appl Physiol (1985)* 2012;112:1593–1599.

132 Wang YX, Lo GG, Yuan J, Larson PE, Zhang X. Magnetic resonance imaging for lung cancer screen. *J Thorac Dis* 2014;6: 1340–1348.

133 Burris NS, Johnson KM, Larson PE, Hope MD, Nagle SK, Behr SC, *et al.* Detection of small pulmonary nodules with ultrashort echo time sequences in oncology patients by using a PET/MR system. *Radiology* 2016;278:239–246.

134 Yi CA, Lee KS, Han J, Chung MP, Chung MJ, Shin KM. 3-T MRI for differentiating inflammation- and fibrosis-predominant lesions of usual and nonspecific interstitial pneumonia: comparison study with pathologic correlation. *AJR Am J Roentgenol* 2008;190: 878–885.

135 Lonzetti L, Zanon M, Pacini GS, Altmayer S, Martins de Oliveira D, Rubin AS, *et al.* Magnetic resonance imaging of interstitial lung diseases: a state-of-the-art review. *Respir Med* 2019;155:79–85.

136 Mirsadraee S, Tse M, Kershaw L, Semple S, Schembri N, Chin C, *et al.* T1 characteristics of interstitial pulmonary fibrosis on 3T MRI—a predictor of early interstitial change? *Quant Imaging Med Surg* 2016; 6:42–49.

137 Chassagnon G, Martin C, Marini R, Vakalopolou M, Régent A, Mouthon L, *et al.* Use of elastic registration in pulmonary MRI for the assessment of pulmonary fibrosis in patients with systemic sclerosis. *Radiology* 2019;291:487–492.

138 Ohno Y, Koyama H, Yoshikawa T, Seki S, Takenaka D, Yui M, *et al.* Pulmonary high-resolution ultrashort TE MR imaging: comparison with thin-section standard- and low-dose computed tomography for the assessment of pulmonary parenchyma diseases. *J Magn Reson Imaging* 2016;43:512–532.

139 Barreto MM, Rafful PP, Rodrigues RS, Zanetti G, Hochhegger B, Souza AS Jr, *et al.* Correlation between computed tomographic and magnetic resonance imaging findings of parenchymal lung diseases. *Eur J Radiol* 2013;82:e492–e501.

140 Chen RY, Fan FC, Kim S, Jan KM, Usami S, Chien S. Tissue-blood partition coefficient for xenon: temperature and hematocrit dependence. *J Appl Physiol* 1980;49:178–183.

141 Yeh S-Y, Peterson RE. Solubility of krypton and xenon in blood, protein solutions, and tissue homogenates. *J Appl Physiol* 1965;20: 1041–1047.

142 Cleveland ZI, Cofer GP, Metz G, Beaver D, Nouls J, Kaushik SS, *et al.* Hyperpolarized Xe MR imaging of alveolar gas uptake in humans. *PLoS ONE* 2010;5:e12192.

143 Sakai K, Bilek AM, Oteiza E, Walsworth RL, Balamore D, Jolesz FA, *et al.* Temporal dynamics of hyperpolarized ^{129}Xe resonances in living rats. *J Magn Reson B* 1996;111:300–304.

144 Wagshul ME, Button TM, Li HF, Liang Z, Springer CS, Zhong K, *et al.* In vivo MR imaging and spectroscopy using hyperpolarized ^{129}Xe. *Magn Reson Med* 1996;36:183–191.

145 Wang JM, Robertson SH, Wang Z, He M, Virgincar RS, Schrank GM, *et al.* Using hyperpolarized ^{129}Xe MRI to quantify regional gas transfer in idiopathic pulmonary fibrosis. *Thorax* 2018;73:21–28.

146 Smith BM, Hoffman EA, Rabinowitz D, Bleecker E, Christenson S, Couper D, *et al.*; The Multi-Ethnic Study of Atherosclerosis (MESA) COPD Study and the Subpopulations and Intermediate Outcomes in COPD Study (SPIROMICS). Comparison of spatially matched airways reveals thinner airway walls in COPD. *Thorax* 2014;69: 987–996.

147 Tschirren J, McLennan G, Palágyi K, Hoffman EA, Sonka M. Matching and anatomical labeling of human airway tree. *IEEE Trans Med Imaging* 2005;24:1540–1547.

148 Bodduluri S, Reinhardt JM, Hoffman EA, Newell JD Jr, Bhatt SP. Recent advances in computed tomography imaging in chronic obstructive pulmonary disease. *Ann Am Thorac Soc* 2018;15:281–289.

149 Grydeland TB, Dirksen A, Coxson HO, Eagan TM, Thorsen E, Pillai SG, *et al.* Quantitative computed tomography measures of emphysema and airway wall thickness are related to respiratory symptoms. *Am J Respir Crit Care Med* 2010;181:353–359.

150 Grydeland TB, Dirksen A, Coxson HO, Pillai SG, Sharma S, Eide GE, *et al.* Quantitative computed tomography: emphysema and airway wall thickness by sex, age and smoking. *Eur Respir J* 2009;34: 858–865.

151 Kim V, Davey A, Comellas AP, Han MK, Washko G, Martinez CH, *et al.*; COPDGene® Investigators. Clinical and computed tomographic predictors of chronic bronchitis in COPD: a cross sectional analysis of the COPDGene study. *Respir Res* 2014;15:52.

152 Mair G, Maclay J, Miller JJ, McAllister D, Connell M, Murchison JT, *et al.* Airway dimensions in COPD: relationships with clinical variables. *Respir Med* 2010;104:1683–1690.

153 Bordas R, Lefevre C, Veeckmans B, Pitt-Francis J, Fetita C, Brightling CE, *et al.* Development and analysis of patient-based complete conducting airways models. *PLoS ONE* 2015;10:e0144105.
154 Kim M, Bordas R, Vos W, Hartley RA, Brightling CE, Kay D, *et al.* Dynamic flow characteristics in normal and asthmatic lungs. *Int J Numer Methods Biomed Eng* 2015;31:e02730.
155 Kim M, Doganay O, Matin TN, Povey T, Gleeson FV. CT-based airway flow model to assess ventilation in chronic obstructive pulmonary disease: a pilot study. *Radiology* 2019;293:666–673.
156 Washko GR, Diaz AA, Kim V, Barr RG, Dransfield MT, Schroeder J, *et al.* Computed tomographic measures of airway morphology in smokers and never-smoking normals. *J Appl Physiol (1985)* 2014; 116:668–673.
157 Washko GR, Dransfield MT, Estépar RS, Diaz A, Matsuoka S, Yamashiro T, *et al.* Airway wall attenuation: a biomarker of airway disease in subjects with COPD. *J Appl Physiol (1985)* 2009;107: 185–191.
158 Bhatt SP, Terry NL, Nath H, Zach JA, Tschirren J, Bolding MS, *et al.* Genetic epidemiology of CI: association between expiratory central airway collapse and respiratory outcomes among smokers. *JAMA* 2016;315:498–505.
159 O'Donnell CR, Litmanovich D, Loring SH, Boiselle PM. Age and sex dependence of forced expiratory central airway collapse in healthy volunteers. *Chest* 2012;142:168–174.
160 Boiselle PM, O'Donnell CR, Bankier AA, Ernst A, Millet ME, Potemkin A, *et al.* Tracheal collapsibility in healthy volunteers during forced expiration: assessment with multidetector CT. *Radiology* 2009;252: 255–262.
161 Dunican EM, Elicker BM, Gierada DS, Nagle SK, Schiebler ML, Newell JD, *et al.*; National Heart Lung and Blood Institute (NHLBI) Severe Asthma Research Program (SARP). Mucus plugs in patients with asthma linked to eosinophilia and airflow obstruction. *J Clin Invest* 2018;128:997–1009.
162 Svenningsen S, Haider E, Boylan C, Mukherjee M, Eddy RL, Capaldi DPI, *et al.* CT and functional MRI to evaluate airway mucus in severe asthma. *Chest* 2019;155:1178–1189.
163 Dunican EM, Elicker BM, Henry T, Gierada DS, Schiebler ML, Anderson W, *et al.* Mucus plugs and emphysema in the pathophysiology of airflow obstruction and hypoxemia in smokers. *Am J Respir Crit Care Med* 2021;203:957–968.
164 Mummy DG, Dunican EM, Carey KJ, Evans MD, Elicker BM, Newell JD Jr, *et al.* Mucus plugs in asthma at CT associated with regional ventilation defects at ^{3}He MRI. *Radiology* 2022;303:184–190.
165 O'Donnell CR, Bankier AA, O'Donnell DH, Loring SH, Boiselle PM. Static end-expiratory and dynamic forced expiratory tracheal collapse in COPD. *Clin Radiol* 2014;69:357–362.
166 Zach JA, Newell JD Jr, Schroeder J, Murphy JR, Curran-Everett D, Hoffman EA, *et al.*; COPDGene Investigators. Quantitative computed tomography of the lungs and airways in healthy nonsmoking adults. *Invest Radiol* 2012;47:596–602.
167 Hackx M, Francotte D, Garcia TS, Van Muylem A, Walsdorff M, Gevenois PA. Effect of total lung capacity, gender and height on CT airway measurements. *Br J Radiol* 2017;90:20160898.
168 Hackx M, Gyssels E, Severo Garcia T, De Meulder I, Alard S, Bruyneel M, *et al.* Chronic obstructive pulmonary disease: CT quantification of airway dimensions, numbers of airways to measure, and effect of bronchodilation. *Radiology* 2015;277:853–862.
169 Aaron CP, Hoffman EA, Lima JAC, Kawut SM, Bertoni AG, Vogel-Claussen J, *et al.* Pulmonary vascular volume, impaired left ventricular filling and dyspnea: the MESA Lung study. *PLoS ONE* 2017;12:e0176180.
170 Leng S, Yu Z, Halaweish A, Kappler S, Hahn K, Henning A, *et al.* A high-resolution imaging technique using a whole-body, research photon counting detector CT system. *Proc SPIE Int Soc Opt Eng* 2016;9783:97831I.
171 Umetani K, Okamoto T, Saito K, Kawata Y, Niki N. 36M-pixel synchrotron radiation micro-CT for whole secondary pulmonary lobule visualization from a large human lung specimen. *Eur J Radiol Open* 2020;7:100262.
172 Preissner M, Murrie RP, Bresee C, Carnibella RP, Fouras A, Weir EK, *et al.* Application of a novel in vivo imaging approach to measure pulmonary vascular responses in mice. *Physiol Rep* 2018;6:e13875.
173 Jin D, Guo J, Dougherty TM, Iyer KS, Hoffman EA, Saha PK. A semi-automatic framework of measuring pulmonary arterial metrics at anatomic airway locations using CT imaging. *Proc SPIE Int Soc Opt Eng* 2016;9788:978816.
174 Charbonnier JP, Brink M, Ciompi F, Scholten ET, Schaefer-Prokop CM, van Rikxoort EM. Automatic pulmonary artery-vein separation and classification in computed tomography using tree partitioning and peripheral vessel matching. *IEEE Trans Med Imaging* 2016;35: 882–892.
175 Washko GR, Nardelli P, Ash SY, Vegas Sanchez-Ferrero G, Rahaghi FN, Come CE, *et al.* Arterial vascular pruning, right ventricular size, and clinical outcomes in chronic obstructive pulmonary disease: a longitudinal observational study. *Am J Respir Crit Care Med* 2019;200:454–461.
176 Pistenmaa CL, Nardelli P, Ash SY, Come CE, Diaz AA, Rahaghi FN, *et al.*; COPDGene Investigators. Pulmonary arterial pruning and longitudinal change in percent emphysema and lung function: the Genetic Epidemiology of COPD study. *Chest* 2021;160:470–480.
177 Ash SY, Rahaghi FN, Come CE, Ross JC, Colon AG, Cardet-Guisasola JC, *et al.*; SARP Investigators. Pruning of the pulmonary vasculature in asthma: the Severe Asthma Research Program (SARP) cohort. *Am J Respir Crit Care Med* 2018;198:39–50.
178 Helmberger M, Pienn M, Urschler M, Kullnig P, Stollberger R, Kovacs G, *et al.* Quantification of tortuosity and fractal dimension of the lung vessels in pulmonary hypertension patients. *PLoS ONE* 2014;9: e87515.
179 Levin DL, Buxton RB, Spiess JP, Arai T, Balouch J, Hopkins SR. Effects of age on pulmonary perfusion heterogeneity measured by magnetic resonance imaging. *J Appl Physiol (1985)* 2007;102: 2064–2070.
180 Glenny RW. Heterogeneity in the lung: concepts and measures. In: Hlastala MP, Robertson HT, editors. Complexity in structure and function in the lung. New York: Marcel Dekker; 1998. pp. 571–609.
181 Truong QA, Massaro JM, Rogers IS, Mahabadi AA, Kriegel MF, Fox CS, *et al.* Reference values for normal pulmonary artery dimensions by noncontrast cardiac computed tomography: the Framingham Heart Study. *Circ Cardiovasc Imaging* 2012;5:147–154.
182 Kuriyama K, Gamsu G, Stern RG, Cann CE, Herfkens RJ, Brundage BH. CT-determined pulmonary artery diameters in predicting pulmonary hypertension. *Invest Radiol* 1984;19:16–22.
183 Tan RT, Kuzo R, Goodman LR, Siegel R, Haasler GB, Presberg KW; Medical College of Wisconsin Lung Transplant Group. Utility of CT scan evaluation for predicting pulmonary hypertension in patients with parenchymal lung disease. *Chest* 1998;113:1250–1256.
184 Raymond TE, Khabbaza JE, Yadav R, Tonelli AR. Significance of main pulmonary artery dilation on imaging studies. *Ann Am Thorac Soc* 2014;11:1623–1632.
185 Bogren HG, Klipstein RH, Mohiaddin RH, Firmin DN, Underwood SR, Rees RS, *et al.* Pulmonary artery distensibility and blood flow patterns: a magnetic resonance study of normal subjects and of patients with pulmonary arterial hypertension. *Am Heart J* 1989;118: 990–999.
186 Jardim C, Rochitte CE, Humbert M, Rubenfeld G, Jasinowodolinski D, Carvalho CR, *et al.* Pulmonary artery distensibility in pulmonary arterial hypertension: an MRI pilot study. *Eur Respir J* 2007;29: 476–481.
187 Gan CT, Lankhaar JW, Westerhof N, Marcus JT, Becker A, Twisk JW, *et al.* Noninvasively assessed pulmonary artery stiffness predicts mortality in pulmonary arterial hypertension. *Chest* 2007;132: 1906–1912.
188 Swift AJ, Wild JM, Nagle SK, Roldán-Alzate A, François CJ, Fain S, *et al.* Quantitative magnetic resonance imaging of pulmonary hypertension: a practical approach to the current state of the art. *J Thorac Imaging* 2014;29:68–79.
189 Chadwick EA, Suzuki T, George MG, Romero DA, Amon C, Waddell TK, *et al.* Vessel network extraction and analysis of mouse pulmonary vasculature via X-ray micro-computed tomographic imaging. *PLoS Comput Biol* 2021;17:e1008930.
190 Hallifax RJ, Talwar A, Wrightson JM, Edey A, Gleeson FV. State-of-the-art: radiological investigation of pleural disease. *Respir Med* 2017;124:88–99.
191 Helm EJ, Matin TN, Gleeson FV. Imaging of the pleura. *J Magn Reson Imaging* 2010;32:1275–1286.

192 Cha YK, Kim JS, Kwon JH. Quantification of pleural plaques by computed tomography and correlations with pulmonary function: preliminary study. *J Thorac Dis* 2018;10:2118–2124.

193 Clark KA, Flynn JJ III, Karmaus WJJ, Mohr LC. The effects of pleural plaques on longitudinal lung function in vermiculite miners of Libby, Montana. *Am J Med Sci* 2017;353:533–542.

194 Remérand F, Dellamonica J, Mao Z, Ferrari F, Bouhemad B, Jianxin Y, *et al.* Multiplane ultrasound approach to quantify pleural effusion at the bedside. *Intensive Care Med* 2010;36:656–664.

195 Capper SJ, Ross JJ, Sandström E, Braidley PC, Morgan-Hughes NJ. Transoesophageal echocardiography for the detection and quantification of pleural fluid in cardiac surgical patients. *Br J Anaesth* 2007;98:442–446.

196 Similowski T, Bates JH. Two-compartment modelling of respiratory system mechanics at low frequencies: gas redistribution or tissue rheology? *Eur Respir J* 1991;4:353–358.

197 Bates JHT. Lung mechanics: an inverse modeling approach. Cambridge: Cambridge University Press; 2009.

198 Macklem PT, Mead J. Resistance of central and peripheral airways measured by a retrograde catheter. *J Appl Physiol* 1967;22:395–401.

199 Kaminsky DA, Irvin CG, Lundblad L, Moriya HT, Lang S, Allen J, *et al.* Oscillation mechanics of the human lung periphery in asthma. *J Appl Physiol (1985)* 2004;97:1849–1858.

200 Mishima M, Balassy Z, Bates JH. Acute pulmonary response to intravenous histamine using forced oscillations through alveolar capsules in dogs. *J Appl Physiol (1985)* 1994;77: 2140–2148.

201 Chevalier PA, Rodarte JR, Harris LD. Regional lung expansion at total lung capacity in intact vs. excised canine lungs. *J Appl Physiol* 1978; 45:363–369.

202 Yilmaz C, Tustison NJ, Dane DM, Ravikumar P, Takahashi M, Gee JC, *et al.* Progressive adaptation in regional parenchyma mechanics following extensive lung resection assessed by functional computed tomography. *J Appl Physiol (1985)* 2011;111:1150–1158.

203 Yilmaz C, Dane DM, Tustison NJ, Song G, Gee JC, Hsia CCW. In vivo imaging of canine lung deformation: effects of posture, pneumonectomy, and inhaled erythropoietin. *J Appl Physiol (1985)* 2020;128:1093–1105.

204 Motta-Ribeiro GC, Hashimoto S, Winkler T, Baron RM, Grogg K, Paula LFSC, *et al.* Deterioration of regional lung strain and inflammation during early lung injury. *Am J Respir Crit Care Med* 2018;198:891–902.

205 Mariappan YK, Glaser KJ, Hubmayr RD, Manduca A, Ehman RL, McGee KP. MR elastography of human lung parenchyma: technical development, theoretical modeling and in vivo validation. *J Magn Reson Imaging* 2011;33:1351–1361.

206 Marinelli JP, Levin DL, Vassallo R, Carter RE, Hubmayr RD, Ehman RL, *et al.* Quantitative assessment of lung stiffness in patients with interstitial lung disease using MR elastography. *J Magn Reson Imaging* 2017;46:365–374.

207 Zhou B, Bartholmai BJ, Kalra S, Osborn TG, Zhang X. Lung US surface wave elastography in interstitial lung disease staging. *Radiology* 2019;291:479–484.

208 Hasse K, Neylon J, Min Y, O'Connell D, Lee P, Low DA, *et al.* Feasibility of deriving a novel imaging biomarker based on patient-specific lung elasticity for characterizing the degree of COPD in lung SBRT patients. *Br J Radiol* 2019;92:20180296.

209 Thorpe CW, Bates JH. Effect of stochastic heterogeneity on lung impedance during acute bronchoconstriction: a model analysis. *J Appl Physiol (1985)* 1997;82:1616–1625.

210 Gillis HL, Lutchen KR. How heterogeneous bronchoconstriction affects ventilation distribution in human lungs: a morphometric model. *Ann Biomed Eng* 1999;27:14–22.

211 Miyawaki S, Tawhai MH, Hoffman EA, Lin CL. Effect of carrier gas properties on aerosol distribution in a CT-based human airway numerical model. *Ann Biomed Eng* 2012;40:1495–1507.

212 Kaczka DW, Cao K, Christensen GE, Bates JH, Simon BA. Analysis of regional mechanics in canine lung injury using forced oscillations and 3D image registration. *Ann Biomed Eng* 2011;39: 1112–1124.

213 Tawhai MH, Hunter P, Tschirren J, Reinhardt J, McLennan G, Hoffman EA. CT-based geometry analysis and finite element models of the human and ovine bronchial tree. *J Appl Physiol (1985)* 2004; 97:2310–2321.

214 Lewis SM, Evans JW, Jalowayski AA. Continuous distributions of specific ventilation recovered from inert gas washout. *J Appl Physiol* 1978;44:416–423.

215 Sá RC, Cronin MV, Henderson AC, Holverda S, Theilmann RJ, Arai TJ, *et al.* Vertical distribution of specific ventilation in normal supine humans measured by oxygen-enhanced proton MRI. *J Appl Physiol (1985)* 2010;109:1950–1959.

216 Geier ET, Neuhart I, Theilmann RJ, Prisk GK, Sá RC. Spatial persistence of reduced specific ventilation following methacholine challenge in the healthy human lung. *J Appl Physiol (1985)* 2018;124: 1222–1232.

217 Rhodes CG, Valind SO, Brudin LH, Wollmer PE, Jones T, Hughes JM. Quantification of regional V/Q ratios in humans by use of PET. I. Theory. *J Appl Physiol (1985)* 1989;66:1896–1904.

218 Treppo S, Mijailovich SM, Venegas JG. Contributions of pulmonary perfusion and ventilation to heterogeneity in V_A/Q measured by PET. *J Appl Physiol (1985)* 1997;82:1163–1176.

219 Valind SO, Rhodes CG, Brudin LH, Jones T. Measurements of regional ventilation pulmonary gas volume: theory and error analysis with special reference to positron emission tomography. *J Nucl Med* 1991; 32:1937–1944.

220 Hofman MS, Beauregard JM, Barber TW, Neels OC, Eu P, Hicks RJ. ^{68}Ga PET/CT ventilation-perfusion imaging for pulmonary embolism: a pilot study with comparison to conventional scintigraphy. *J Nucl Med* 2011;52:1513–1519.

221 Blanc-Béguin F, Hennebicq S, Robin P, Tripier R, Salaün P-Y, Le Roux P-Y. Radiopharmaceutical labelling for lung ventilation/perfusion PET/CT imaging: a review of production and optimization processes for clinical use. *Pharmaceuticals (Basel)* 2022;15:518.

222 Vidal Melo MF, Layfield D, Harris RS, O'Neill K, Musch G, Richter T, *et al.* Quantification of regional ventilation-perfusion ratios with PET. *J Nucl Med* 2003;44:1982–1991.

223 Melo MF, Harris RS, Layfield JDH, Venegas JG. Topographic basis of bimodal ventilation-perfusion distributions during bronchoconstriction in sheep. *Am J Respir Crit Care Med* 2005;171:714–721.

224 Wellman TJ, Winkler T, Costa EL, Musch G, Harris RS, Venegas JG, *et al.* Effect of regional lung inflation on ventilation heterogeneity at different length scales during mechanical ventilation of normal sheep lungs. *J Appl Physiol (1985)* 2012;113:947–957.

225 Dabisch PA, Xu Z, Boydston JA, Solomon J, Bohannon JK, Yeager JJ, *et al.* Quantification of regional aerosol deposition patterns as a function of aerodynamic particle size in rhesus macaques using PET/CT imaging. *Inhal Toxicol* 2017;29:506–515.

226 Greenblatt EE, Winkler T, Harris RS, Kelly VJ, Kone M, Katz I, *et al.* What causes uneven aerosol deposition in the bronchoconstricted lung? A quantitative imaging study. *J Aerosol Med Pulm Drug Deliv* 2016;29:57–75.

227 Fleming J, Conway J, Majoral C, Katz I, Caillibotte G, Pichelin M, *et al.* Controlled, parametric, individualized, 2-D and 3-D imaging measurements of aerosol deposition in the respiratory tract of asthmatic human subjects for model validation. *J Aerosol Med Pulm Drug Deliv* 2015;28:432–451.

228 Majoral C, Fleming J, Conway J, Katz I, Tossici-Bolt L, Pichelin M, *et al.* Controlled, parametric, individualized, 2D and 3D imaging measurements of aerosol deposition in the respiratory tract of healthy human volunteers: in vivo data analysis. *J Aerosol Med Pulm Drug Deliv* 2014;27:349–362.

229 Cedillo-Pozos A, Ternovoy SK, Roldan-Valadez E. Imaging methods used in the assessment of environmental disease networks: a brief review for clinicians. *Insights Imaging* 2020;11:18.

230 Jacob RE, Lamm WJ, Einstein DR, Krueger MA, Glenny RW, Corley RA. Comparison of CT-derived ventilation maps with deposition patterns of inhaled microspheres in rats. *Exp Lung Res* 2015;41:135–145.

231 Rostami AA. Computational modeling of aerosol deposition in respiratory tract: a review. *Inhal Toxicol* 2009;21:262–290.

232 Higano NS, Fleck RJ, Spielberg DR, Walkup LL, Hahn AD, Thomen RP, *et al.* Quantification of neonatal lung parenchymal density via ultrashort echo time MRI with comparison to CT. *J Magn Reson Imaging* 2017;46:992–1000.

233 Hahn AD, Malkus A, Kammerman J, Higano N, Walkup L, Woods J, *et al.* Characterization of R_2^* and tissue density in the human lung: application to neonatal imaging in the intensive care unit. *Magn Reson Med* 2020;84:920–927.

234 Lederlin M, Crémillieux Y. Three-dimensional assessment of lung tissue density using a clinical ultrashort echo time at 3 tesla: a feasibility study in healthy subjects. *J Magn Reson Imaging* 2014;40: 839–847.

235 Theilmann RJ, Arai TJ, Samiee A, Dubowitz DJ, Hopkins SR, Buxton RB, *et al.* Quantitative MRI measurement of lung density must account for the change in T_2^* with lung inflation. *J Magn Reson Imaging* 2009;30:527–534.

236 Pennati F, Quirk JD, Yablonskiy DA, Castro M, Aliverti A, Woods JC. Assessment of regional lung function with multivolume ^{1}H MR imaging in health and obstructive lung disease: comparison with ^{3}He MR imaging. *Radiology* 2014;273:580–590.

237 Voskrebenzev A, Gutberlet M, Klimeš F, Kaireit TF, Schönfeld C, Rotärmel A, *et al.* Feasibility of quantitative regional ventilation and perfusion mapping with phase-resolved functional lung (PREFUL) MRI in healthy volunteers and COPD, CTEPH, and CF patients. *Magn Reson Med* 2018;79:2306–2314.

238 Kirby M, Heydarian M, Svenningsen S, Wheatley A, McCormack DG, Etemad-Rezai R, *et al.* Hyperpolarized ^{3}He magnetic resonance functional imaging semiautomated segmentation. *Acad Radiol* 2012; 19:141–152.

239 Shukla Y, Wheatley A, Kirby M, Svenningsen S, Farag A, Santyr GE, *et al.* Hyperpolarized ^{129}Xe magnetic resonance imaging: tolerability in healthy volunteers and subjects with pulmonary disease. *Acad Radiol* 2012;19:941–951.

240 Mathew L, Evans A, Ouriadov A, Etemad-Rezai R, Fogel R, Santyr G, *et al.* Hyperpolarized ^{3}He magnetic resonance imaging of chronic obstructive pulmonary disease: reproducibility at 3.0 tesla. *Acad Radiol* 2008;15:1298–1311.

241 Driehuys B, Martinez-Jimenez S, Cleveland ZI, Metz GM, Beaver DM, Nouls JC, *et al.* Chronic obstructive pulmonary disease: safety and tolerability of hyperpolarized ^{129}Xe MR imaging in healthy volunteers and patients. *Radiology* 2012;262:279–289.

242 Kirby M, Svenningsen S, Owrangi A, Wheatley A, Farag A, Ouriadov A, *et al.* Hyperpolarized ^{3}He and ^{129}Xe MR imaging in healthy volunteers and patients with chronic obstructive pulmonary disease. *Radiology* 2012;265:600–610.

243 Kirby M, Pike D, Coxson HO, McCormack DG, Parraga G. Hyperpolarized ^{3}He ventilation defects used to predict pulmonary exacerbations in mild to moderate chronic obstructive pulmonary disease. *Radiology* 2014;273:887–896.

244 Kirby M, Kanhere N, Etemad-Rezai R, McCormack DG, Parraga G. Hyperpolarized helium-3 magnetic resonance imaging of chronic obstructive pulmonary disease exacerbation. *J Magn Reson Imaging* 2013;37:1223–1227.

245 Virgincar RS, Cleveland ZI, Kaushik SS, Freeman MS, Nouls J, Cofer GP, *et al.* Quantitative analysis of hyperpolarized ^{129}Xe ventilation imaging in healthy volunteers and subjects with chronic obstructive pulmonary disease. *NMR Biomed* 2013;26: 424–435.

246 Capaldi DP, Zha N, Guo F, Pike D, McCormack DG, Kirby M, *et al.* Pulmonary imaging biomarkers of gas trapping and emphysema in COPD: ^{3}He MR imaging and CT parametric response maps. *Radiology* 2016;279:597–608.

247 Kirby M, Ouriadov A, Svenningsen S, Owrangi A, Wheatley A, Etemad-Rezai R, *et al.* Hyperpolarized ^{3}He and ^{129}Xe magnetic resonance imaging apparent diffusion coefficients: physiological relevance in older never- and ex-smokers. *Physiol Rep* 2014;2:e12068.

248 Stewart NJ, Chan HF, Hughes PJC, Horn FC, Norquay G, Rao M, *et al.* Comparison of ^{3} He and ^{129} Xe MRI for evaluation of lung microstructure and ventilation at 1.5T. *J Magn Reson Imaging* 2018; 48:632–642.

249 Hamedani H, Kadlecek S, Ruppert K, Xin Y, Duncan I, Rizi RR. Ventilation heterogeneity imaged by multibreath wash-ins of hyperpolarized ^{3} He and ^{129} Xe in healthy rabbits. *J Physiol* 2021;599: 4197–4223.

250 Marshall H, Horsley A, Taylor CJ, Smith L, Hughes D, Horn FC, *et al.* Detection of early subclinical lung disease in children with cystic fibrosis by lung ventilation imaging with hyperpolarised gas MRI. *Thorax* 2017;72:760–762.

251 Thomen RP, Walkup LL, Roach DJ, Cleveland ZI, Clancy JP, Woods JC. Hyperpolarized ^{129}Xe for investigation of mild cystic fibrosis lung disease in pediatric patients. *J Cyst Fibros* 2017;16:275–282.

252 Bauman G, Puderbach M, Deimling M, Jellus V, Chefd'hotel C, Dinkel J, *et al.* Non-contrast-enhanced perfusion and ventilation assessment of the human lung by means of fourier decomposition in proton MRI. *Magn Reson Med* 2009;62:656–664.

253 Edelman RR, Hatabu H, Tadamura E, Li W, Prasad PV. Noninvasive assessment of regional ventilation in the human lung using oxygen-enhanced magnetic resonance imaging. *Nat Med* 1996;2:1236–1239.

254 Ohno Y, Hatabu H. Basics concepts and clinical applications of oxygen-enhanced MR imaging. *Eur J Radiol* 2007;64:320–328.

255 Hatabu H, Tadamura E, Chen Q, Stock KW, Li W, Prasad PV, *et al.* Pulmonary ventilation: dynamic MRI with inhalation of molecular oxygen. *Eur J Radiol* 2001;37:172–178.

256 Sá RC, Asadi AK, Theilmann RJ, Hopkins SR, Prisk GK, Darquenne C. Validating the distribution of specific ventilation in healthy humans measured using proton MR imaging. *J Appl Physiol (1985)* 2014;116: 1048–1056.

257 Naish JH, Parker GJ, Beatty PC, Jackson A, Young SS, Waterton JC, *et al.* Improved quantitative dynamic regional oxygen-enhanced pulmonary imaging using image registration. *Magn Reson Med* 2005; 54:464–469.

258 Zha W, Kruger SJ, Johnson KM, Cadman RV, Bell LC, Liu F, *et al.* Pulmonary ventilation imaging in asthma and cystic fibrosis using oxygen-enhanced 3D radial ultrashort echo time MRI. *J Magn Reson Imaging* 2018;47:1287–1297.

259 Kruger SJ, Fain SB, Johnson KM, Cadman RV, Nagle SK. Oxygen-enhanced 3D radial ultrashort echo time magnetic resonance imaging in the healthy human lung. *NMR Biomed* 2014;27:1535–1541.

260 Sasaki T, Takahashi K, Obara M. Viability of oxygen-enhanced ventilation imaging of the lungs using ultra-short echo time MRI. *Magn Reson Med Sci* 2017;16:259–261.

261 Zha W, Nagle SK, Cadman RV, Schiebler ML, Fain SB. Three-dimensional isotropic functional imaging of cystic fibrosis using oxygen-enhanced MRI: comparison with hyperpolarized ^{3}He MRI. *Radiology* 2019;290:229–237.

262 Arai TJ, Horn FC, Sa RC, Rao MR, Collier GJ, Theilmann RJ, *et al.* Comparison of quantitative multiple-breath specific ventilation imaging using colocalized 2D oxygen-enhanced MRI and hyperpolarized ^{3}He MRI. *J Appl Physiol (1985)* 2018;125:1526–1535.

263 Halaweish AF, Moon RE, Foster WM, Soher BJ, McAdams HP, MacFall JR, *et al.* Perfluoropropane gas as a magnetic resonance lung imaging contrast agent in humans. *Chest* 2013;144: 1300–1310.

264 Schreiber WG, Eberle B, Laukemper-Ostendorf S, Markstaller K, Weiler N, Scholz A, *et al.* Dynamic ^{19}F-MRI of pulmonary ventilation using sulfur hexafluoride (SF_6) gas. *Magn Reson Med* 2001;45:605–613.

265 Gutberlet M, Kaireit TF, Voskrebenzev A, Lasch F, Freise J, Welte T, *et al.* Free-breathing dynamic ^{19}F gas MR imaging for mapping of regional lung ventilation in patients with COPD. *Radiology* 2018;286: 1040–1051.

266 Screaton NJ, Coxson HO, Kalloger SE, Baile EM, Nakano Y, Hiorns M, *et al.* Detection of lung perfusion abnormalities using computed tomography in a porcine model of pulmonary embolism. *J Thorac Imaging* 2003;18:14–20.

267 Wildberger JE, Klotz E, Ditt H, Spüntrup E, Mahnken AH, Günther RW. Multislice computed tomography perfusion imaging for visualization of acute pulmonary embolism: animal experience. *Eur Radiol* 2005;15: 1378–1386.

268 Grob D, Oostveen LJ, Prokop M, Schaefer-Prokop CM, Sechopoulos I, Brink M. Imaging of pulmonary perfusion using subtraction CT angiography is feasible in clinical practice. *Eur Radiol* 2019;29: 1408–1414.

269 Remy-Jardin M, Mastora I, Remy J. Pulmonary embolus imaging with multislice CT. *Radiol Clin North Am* 2003;41:507–519.

270 Patel S, Kazerooni EA. Helical CT for the evaluation of acute pulmonary embolism. *AJR Am J Roentgenol* 2005;185:135–149.

271 Schoepf UJ. Diagnosing pulmonary embolism: time to rewrite the textbooks. *Int J Cardiovasc Imaging* 2005;21:155–163.

272 Johnson TR, Krauss B, Sedlmair M, Grasruck M, Bruder H, Morhard D, *et al.* Material differentiation by dual energy CT: initial experience. *Eur Radiol* 2007;17:1510–1517.

273 Thieme SF, Johnson TR, Lee C, McWilliams J, Becker CR, Reiser MF, *et al.* Dual-energy CT for the assessment of contrast material distribution in the pulmonary parenchyma. *AJR Am J Roentgenol* 2009;193:144–149.

274 Fuld MK, Halaweish AF, Haynes SE, Divekar AA, Guo J, Hoffman EA. Pulmonary perfused blood volume with dual-energy CT as surrogate for pulmonary perfusion assessed with dynamic multidetector CT. *Radiology* 2013;267:747–756.

275 Okada M, Kunihiro Y, Nakashima Y, Nomura T, Kudomi S, Yonezawa T, *et al.* Added value of lung perfused blood volume images using dual-energy CT for assessment of acute pulmonary embolism. *Eur J Radiol* 2015;84:172–177.

276 Zhao Y, Hubbard L, Malkasian S, Abbona P, Molloi S. Dynamic pulmonary CT perfusion using first-pass analysis technique with only two volume scans: validation in a swine model. *PLoS ONE* 2020;15: e0228110.

277 Mijailovich SM, Treppo S, Venegas JG. Effects of lung motion and tracer kinetics corrections on PET imaging of pulmonary function. *J Appl Physiol (1985)* 1997;82:1154–1162.

278 Brudin LH, Rhodes CG, Valind SO, Buckingham PD, Jones T, Hughes JM. Regional structure-function correlations in chronic obstructive lung disease measured with positron emission tomography. *Thorax* 1992;47:914–921.

279 Mintun MA, Dennis DR, Welch MJ, Mathias CJ, Schuster DP. Measurements of pulmonary vascular permeability with PET and gallium-68 transferrin. *J Nucl Med* 1987;28:1704–1716.

280 Schuster DP, Kaplan JD, Gauvain K, Welch MJ, Markham J. Measurement of regional pulmonary blood flow with PET. *J Nucl Med* 1995;36:371–377.

281 Richard JC, Janier M, Decailliot F, Le Bars D, Lavenne F, Berthier V, *et al.* Comparison of PET with radioactive microspheres to assess pulmonary blood flow. *J Nucl Med* 2002;43:1063–1071.

282 Hayes RL, Carlton JE, Kuniyasu Y. A new method for labeling microspheres with ^{68}Ga. *Eur J Nucl Med* 1981;6:531–533.

283 Mintun MA, Ter-Pogossian MM, Green MA, Lich LL, Schuster DP. Quantitative measurement of regional pulmonary blood flow with positron emission tomography. *J Appl Physiol (1985)* 1986;60: 317–326.

284 Velasco C, Mateo J, Santos A, Mota-Cobian A, Herranz F, Pellico J, *et al.* Assessment of regional pulmonary blood flow using ^{68}Ga-DOTA PET. *EJNMMI Res* 2017;7:7.

285 Pouzot C, Richard JC, Gros A, Costes N, Lavenne F, Le Bars D, *et al.* Noninvasive quantitative assessment of pulmonary blood flow with ^{18}F-FDG PET. *J Nucl Med* 2013;54:1653–1660.

286 Wellman TJ, Winkler T, Vidal Melo MF. Modeling of tracer transport delays for improved quantification of regional pulmonary ^{18}F-FDG kinetics, vascular transit times, and perfusion. *Ann Biomed Eng* 2015; 43:2722–2734.

287 Brudin LH, Rhodes CG, Valind SO, Jones T, Hughes JMB. Interrelationships between regional blood flow, blood volume, and ventilation in supine humans. *J Appl Physiol (1985)* 1994;76: 1205–1210.

288 Petersson J, Sánchez-Crespo A, Rohdin M, Montmerle S, Nyrén S, Jacobsson H, *et al.* Physiological evaluation of a new quantitative SPECT method measuring regional ventilation and perfusion. *J Appl Physiol (1985)* 2004;96:1127–1136.

289 Petersson J, Sánchez-Crespo A, Larsson SA, Mure M. Physiological imaging of the lung: single-photon-emission computed tomography (SPECT). *J Appl Physiol (1985)* 2007;102:468–476.

290 Petersson J, Rohdin M, Sánchez-Crespo A, Nyrén S, Jacobsson H, Larsson SA, *et al.* Regional lung blood flow and ventilation in upright humans studied with quantitative SPECT. *Respir Physiol Neurobiol* 2009;166:54–60.

291 Thompson HK Jr, Starmer CF, Whalen RE, McIntosh HD. Indicator transit time considered as a gamma variate. *Circ Res* 1964;14: 502–515.

292 Wilke N, Jerosch-Herold M, Stillman AE, Kroll K, Tsekos N, Merkle H, *et al.* Concepts of myocardial perfusion imaging in magnetic resonance imaging. *Magn Reson Q* 1994;10:249–286.

293 Stewart GN. Researches on the circulation time in organs and on the influences which affect it. *J Physiol* 1893;15:1–89.

294 Bolar DS, Levin DL, Hopkins SR, Frank LF, Liu TT, Wong EC, *et al.* Quantification of regional pulmonary blood flow using ASL-FAIRER. *Magn Reson Med* 2006;55:1308–1317.

295 Henderson AC, Prisk GK, Levin DL, Hopkins SR, Buxton RB. Characterizing pulmonary blood flow distribution measured using arterial spin labeling. *NMR Biomed* 2009;22:1025–1035.

296 Mai VM, Berr SS. MR perfusion imaging of pulmonary parenchyma using pulsed arterial spin labeling techniques: FAIRER and FAIR. *J Magn Reson Imaging* 1999;9:483–487.

297 Mai VM, Hagspiel KD, Christopher JM, Do HM, Altes T, Knight-Scott J, *et al.* Perfusion imaging of the human lung using flow-sensitive alternating inversion recovery with an extra radiofrequency pulse (FAIRER). *Magn Reson Imaging* 1999;17:355–361.

298 Neeb D, Kunz RP, Ley S, Szábo G, Strauss LG, Kauczor HU, *et al.* Quantification of pulmonary blood flow (PBF): validation of perfusion MRI and nonlinear contrast agent (CA) dose correction with $H_2{}^{15}O$ positron emission tomography (PET). *Magn Reson Med* 2009;62: 476–487.

299 Hopkins SR, Prisk GK. Lung perfusion measured using magnetic resonance imaging: new tools for physiological insights into the pulmonary circulation. *J Magn Reson Imaging* 2010;32:1287–1301.

300 Bauman G, Johnson KM, Bell LC, Velikina JV, Samsonov AA, Nagle SK, *et al.* Three-dimensional pulmonary perfusion MRI with radial ultrashort echo time and spatial-temporal constrained reconstruction. *Magn Reson Med* 2015;73:555–564.

301 Sá RC, Henderson AC, Simonson T, Arai TJ, Wagner H, Theilmann RJ, *et al.* Measurement of the distribution of ventilation-perfusion ratios in the human lung with proton MRI: comparison with the multiple inert-gas elimination technique. *J Appl Physiol (1985)* 2017;123:136–146.

302 Glenny RW, Robertson HT. Spatial distribution of ventilation and perfusion: mechanisms and regulation. *Compr Physiol* 2011;1: 375–395.

303 Burnham KJ, Arai TJ, Dubowitz DJ, Henderson AC, Holverda S, Buxton RB, *et al.* Pulmonary perfusion heterogeneity is increased by sustained, heavy exercise in humans. *J Appl Physiol (1985)* 2009; 107:1559–1568.

304 Hall ET, Sá RC, Holverda S, Arai TJ, Dubowitz DJ, Theilmann RJ, *et al.* The effect of supine exercise on the distribution of regional pulmonary blood flow measured using proton MRI. *J Appl Physiol (1985)* 2014; 116:451–461.

305 Henderson AC, Levin DL, Hopkins SR, Olfert IM, Buxton RB, Prisk GK. Steep head-down tilt has persisting effects on the distribution of pulmonary blood flow. *J Appl Physiol (1985)* 2006;101:583–589.

306 Tedjasaputra V, Sá RC, Arai TJ, Holverda S, Theilmann RJ, Chen WT, *et al.* The heterogeneity of regional specific ventilation is unchanged following heavy exercise in athletes. *J Appl Physiol (1985)* 2013;115: 126–135.

307 Ball WC Jr, Stewart PB, Newsham LG, Bates DV. Regional pulmonary function studied with xenon 133. *J Clin Invest* 1962;41:519–531.

308 Kohli P, Kelly VJ, Kehl EG, Rodriguez-Lopez J, Hibbert KA, Kone M, *et al.* Perfusion imaging distinguishes exercise pulmonary arterial hypertension at rest. *Am J Respir Crit Care Med* 2019;199:1438–1441.

309 Winkler T, Melo MF, Degani-Costa LH, Harris RS, Correia JA, Musch G, *et al.* Estimation of noise-free variance to measure heterogeneity. *PLoS ONE* 2015;10:e0123417.

310 Vidal Melo MF, Winkler T, Harris RS, Musch G, Greene RE, Venegas JG. Spatial heterogeneity of lung perfusion assessed with ^{13}N PET as a vascular biomarker in chronic obstructive pulmonary disease. *J Nucl Med* 2010;51:57–65.

311 Glenny RW, Polissar NL, McKinney S, Robertson HT. Temporal heterogeneity of regional pulmonary perfusion is spatially clustered. *J Appl Physiol (1985)* 1995;79:986–1001.

312 Hopkins SR, Garg J, Bolar DS, Balouch J, Levin DL. Pulmonary blood flow heterogeneity during hypoxia and high-altitude pulmonary edema. *Am J Respir Crit Care Med* 2005;171:83–87.

313 Dehnert C, Risse F, Ley S, Kuder TA, Buhmann R, Puderbach M, *et al.* Magnetic resonance imaging of uneven pulmonary perfusion in hypoxia in humans. *Am J Respir Crit Care Med* 2006;174: 1132–1138.

314 Hopkins SR, Sá RC, Prisk GK, Elliott AR, Kim NH, Pazar BJ, *et al.* Abnormal pulmonary perfusion heterogeneity in patients with Fontan circulation and pulmonary arterial hypertension. *J Physiol* 2021;599: 343–356.

315 Arai T, Asadi A, Sá R. Deforminator. GitHub; 2016 [updated 2019 Apr 25; accessed 2022 April 1]. Available at: https://github.com/UCSDPulmonaryImaging/Deforminator/.

316 Asadi AK, Cronin MV, Sá RC, Theilmann RJ, Holverda S, Hopkins SR, *et al.* Spatial-temporal dynamics of pulmonary blood flow in the healthy human lung in response to altered FI(O_2). *J Appl Physiol (1985)* 2013;114:107–118.

317 Asadi AK, Sá RC, Arai TJ, Theilmann RJ, Hopkins SR, Buxton RB, *et al.* Regional pulmonary perfusion patterns in humans are not significantly altered by inspiratory hypercapnia. *J Appl Physiol (1985)* 2019;127: 365–375.

318 Asadi AK, Sá RC, Kim NH, Theilmann RJ, Hopkins SR, Buxton RB, *et al.* Inhaled nitric oxide alters the distribution of blood flow in the healthy human lung, suggesting active hypoxic pulmonary vasoconstriction in normoxia. *J Appl Physiol (1985)* 2015;118:331–343.

319 Prisk G, Elliott A, Bird E, Geier E, Moon Y, Kim N, *et al.* Spatial-temporal imaging of the pulmonary blood flow distribution correlates with severity of pulmonary arterial hypertension [abstract]. *Am J Respir Crit Care Med* 2017;195:A6523.

320 Arai TJ, Theilmann RJ, Sá RC, Villongco MT, Hopkins SR. The effect of lung deformation on the spatial distribution of pulmonary blood flow. *J Physiol* 2016;594:6333–6347.

321 Chon D, Beck KC, Larsen RL, Shikata H, Hoffman EA. Regional pulmonary blood flow in dogs by 4D-X-ray CT. *J Appl Physiol (1985)* 2006;101:1451–1465.

322 Alford SK, van Beek EJ, McLennan G, Hoffman EA. Heterogeneity of pulmonary perfusion as a mechanistic image-based phenotype in emphysema susceptible smokers. *Proc Natl Acad Sci U S A* 2010; 107:7485–7490.

323 Burrowes KS, Buxton RB, Prisk GK. Assessing potential errors of MRI-based measurements of pulmonary blood flow using a detailed network flow model. *J Appl Physiol (1985)* 2012;113:130–141.

324 Addo DA, Kang W, Prisk GK, Tawhai MH, Burrowes KS. Optimizing human pulmonary perfusion measurement using an in silico model of arterial spin labeling magnetic resonance imaging. *Physiol Rep* 2019; 7:e14077.

325 Walker SC, Asadi AK, Hopkins SR, Buxton RB, Prisk GK. A statistical clustering approach to discriminating perfusion from conduit vessel signal contributions in a pulmonary ASL MR image. *NMR Biomed* 2015;28:1117–1124.

326 West JB, Dollery CT, Naimark A. Distribution of blood flow in isolated lung; relation to vascular and alveolar pressures. *J Appl Physiol* 1964; 19:713–724.

327 Ebner L, He M, Virgincar RS, Heacock T, Kaushik SS, Freemann MS, *et al.* Hyperpolarized ^{129}xenon magnetic resonance imaging to quantify regional ventilation differences in mild to moderate asthma: a prospective comparison between semiautomated ventilation defect percentage calculation and pulmonary function tests. *Invest Radiol* 2017;52:120–127.

328 Kooner HK, McIntosh MJ, Desaigoudar V, Rayment JH, Eddy RL, Driehuys B, *et al.* Pulmonary functional MRI: detecting the structure-function pathologies that drive asthma symptoms and quality of life. *Respirology* 2022;27:114–133.

329 Rayment JH, Couch MJ, McDonald N, Kanhere N, Manson D, Santyr G, *et al.* Hyperpolarised ^{129}Xe magnetic resonance imaging to monitor treatment response in children with cystic fibrosis. *Eur Respir J* 2019; 53:1802188.

330 Matin TN, Rahman N, Nickol AH, Chen M, Xu X, Stewart NJ, *et al.* Chronic obstructive pulmonary disease: lobar analysis with hyperpolarized ^{129}Xe MR imaging. *Radiology* 2017;282:857–868.

331 Wang Z, Bier EA, Swaminathan A, Parikh K, Nouls J, He M, *et al.* Diverse cardiopulmonary diseases are associated with distinct xenon magnetic resonance imaging signatures. *Eur Respir J* 2019;54: 1900831.

332 Kern AL, Vogel-Claussen J. Hyperpolarized gas MRI in pulmonology. *Br J Radiol* 2018;91:20170647.

333 Cherubini A, Bifone A. Hyperpolarised xenon in biology. *Prog Nucl Magn Reson Spectrosc* 2003;42:1–30.

334 Qing K, Ruppert K, Jiang Y, Mata JF, Miller GW, Shim YM, *et al.* Regional mapping of gas uptake by blood and tissue in the human lung using hyperpolarized xenon-129 MRI. *J Magn Reson Imaging* 2014;39:346–359.

335 Bier EA, Robertson SH, Schrank GM, Rackley C, Mammarappallil JG, Rajagopal S, *et al.* A protocol for quantifying cardiogenic oscillations in dynamic ^{129} Xe gas exchange spectroscopy: the effects of idiopathic pulmonary fibrosis. *NMR Biomed* 2019;32:e4029.

336 Walkup LL, Thomen RP, Akinyi TG, Watters E, Ruppert K, Clancy JP, *et al.* Feasibility, tolerability and safety of pediatric hyperpolarized ^{129}Xe magnetic resonance imaging in healthy volunteers and children with cystic fibrosis. *Pediatr Radiol* 2016;46:1651–1662.

337 Collier GJ, Hughes PJC, Horn FC, Chan HF, Tahir B, Norquay G, *et al.* Single breath-held acquisition of coregistered 3D ^{129} Xe lung ventilation and anatomical proton images of the human lung with compressed sensing. *Magn Reson Med* 2019;82:342–347.

338 Wang Z, Robertson SH, Wang J, He M, Virgincar RS, Schrank GM, *et al.* Quantitative analysis of hyperpolarized ^{129} Xe gas transfer MRI. *Med Phys* 2017;44:2415–2428.

339 Mugler JP. MRI acquisition techniques. In: Albert MS, Hane FT, editors. Hyperpolarized and inert gas MRI: from technology to application in research and medicine. New York, NY: Elsevier; 2017. pp. 1–21.

340 He M, Zha W, Tan F, Rankine L, Fain S, Driehuys B. A comparison of two hyperpolarized ^{129}Xe MRI ventilation quantification pipelines: the effect of signal to noise ratio. *Acad Radiol* 2019;26:949–959.

341 Niedbalski P, Hall C, Eddy R, Rayment J, Svenningsen S, Parraga G, *et al.* Protocols for multi-site trials using hyperpolarized ^{129}Xe MRI for imaging of ventilation, alveolar-airspace size, and gas exchange: a position paper from the ^{129}Xe MRI Clinical Trials Consortium. *Magn Reson Med* 2021;86:2966–2986.

342 Horn FC, Rao M, Stewart NJ, Wild JM. Multiple breath washout of hyperpolarized ^{129} Xe and ^{3} He in human lungs with three-dimensional balanced steady-state free-precession imaging. *Magn Reson Med* 2017;77:2288–2295.

343 Hughes PJC, Smith L, Chan HF, Tahir BA, Norquay G, Collier GJ, *et al.* Assessment of the influence of lung inflation state on the quantitative parameters derived from hyperpolarized gas lung ventilation MRI in healthy volunteers. *J Appl Physiol (1985)* 2019;126:183–192.

344 Rhodes CG, Valind SO, Brudin LH, Wollmer PE, Jones T, Buckingham PD, *et al.* Quantification of regional V/Q ratios in humans by use of PET. II. Procedure and normal values. *J Appl Physiol (1985)* 1989;66: 1905–1913.

345 Galletti GG, Venegas JG. Tracer kinetic model of regional pulmonary function using positron emission tomography. *J Appl Physiol (1985)* 2002;93:1104–1114.

346 O'Neill K, Venegas JG, Richter T, Harris RS, Layfield JD, Musch G, *et al.* Modeling kinetics of infused ^{13}NN-saline in acute lung injury. *J Appl Physiol (1985)* 2003;95:2471–2484.

347 Bajc M, Neilly JB, Miniati M, Schuemichen C, Meignan M, Jonson B; EANM Committee. EANM guidelines for ventilation/perfusion scintigraphy: part 1. Pulmonary imaging with ventilation/perfusion single photon emission tomography. *Eur J Nucl Med Mol Imaging* 2009;36:1356–1370.

348 Henderson AC, Sá RC, Theilmann RJ, Buxton RB, Prisk GK, Hopkins SR. The gravitational distribution of ventilation-perfusion ratio is more uniform in prone than supine posture in the normal human lung. *J Appl Physiol (1985)* 2013;115:313–324.

349 Fischer MC, Spector ZZ, Ishii M, Yu J, Emami K, Itkin M, *et al.* Single-acquisition sequence for the measurement of oxygen partial pressure by hyperpolarized gas MRI. *Magn Reson Med* 2004;52: 766–773.

350 Deninger AJ, Eberle B, Bermuth J, Escat B, Markstaller K, Schmiedeskamp J, *et al.* Assessment of a single-acquisition imaging sequence for oxygen-sensitive ^{3}He-MRI. *Magn Reson Med* 2002;47:105–114.

351 Deninger AJ, Eberle B, Ebert M, Grossmann T, Heil W, Kauczor H, *et al.* Quantification of regional intrapulmonary oxygen partial pressure evolution during apnea by ^{3}He MRI. *J Magn Reson* 1999;141:207–216.

352 Hamedani H, Shaghaghi H, Kadlecek SJ, Xin Y, Han B, Siddiqui S, *et al.* Vertical gradients in regional alveolar oxygen tension in supine human lung imaged by hyperpolarized ^{3}He MRI. *NMR Biomed* 2014; 27:1439–1450.

353 Rizi RR, Baumgardner JE, Ishii M, Spector ZZ, Edvinsson JM, Jalali A, *et al.* Determination of regional Va/Q by hyperpolarized ^{3}He MRI. *Magn Reson Med* 2004;52:65–72.
354 Wagner PD, Laravuso RB, Uhl RR, West JB. Continuous distributions of ventilation-perfusion ratios in normal subjects breathing air and 100 per cent O_2. *J Clin Invest* 1974;54:54–68.
355 Venegas JG, Winkler T, Musch G, Vidal Melo MF, Layfield D, Tgavalekos N, *et al.* Self-organized patchiness in asthma as a prelude to catastrophic shifts. *Nature* 2005;434:777–782.
356 Wagner PD, Dantzker DR, Dueck R, Clausen JL, West JB. Ventilation-perfusion inequality in chronic obstructive pulmonary disease. *J Clin Invest* 1977;59:203–216.
357 Hopkins SR, Wagner PD. The multiple inert gas elimination technique (MIGET). Cham, Switzerland: Springer; 2017.
358 Vidal Melo MF, Harris RS, Layfield D, Musch G, Venegas JG. Changes in regional ventilation after autologous blood clot pulmonary embolism. *Anesthesiology* 2002;97:671–681.
359 Wellman TJ, Winkler T, Costa EL, Musch G, Harris RS, Venegas JG, *et al.* Measurement of regional specific lung volume change using respiratory-gated PET of inhaled ^{13}N-nitrogen. *J Nucl Med* 2010;51: 646–653.
360 Simon BA, Venegas JG. Analyzing ^{13}NN lung washout curves in the presence of intraregional nonuniformities. *J Appl Physiol (1985)* 1994; 76:956–964.
361 Kang W, Clark AR, Tawhai MH. Gravity outweighs the contribution of structure to passive ventilation-perfusion matching in the supine adult human lung. *J Appl Physiol (1985)* 2018;124:23–33.
362 Hedges KL, Clark AR, Tawhai MH. Comparison of generic and subject-specific models for simulation of pulmonary perfusion and forced expiration. *Interface Focus* 2015;5:20140090.
363 Donovan GM, Elliot JG, Boser SR, Green FHY, James AL, Noble PB. Patient-specific targeted bronchial thermoplasty: predictions of improved outcomes with structure-guided treatment. *J Appl Physiol (1985)* 2019;126:599–606.
364 Tgavalekos NT, Tawhai M, Harris RS, Musch G, Vidal-Melo M, Venegas JG, *et al.* Identifying airways responsible for heterogeneous ventilation and mechanical dysfunction in asthma: an image functional modeling approach. *J Appl Physiol (1985)* 2005;99: 2388–2397.
365 Mullally W, Betke M, Albert M, Lutchen K. Explaining clustered ventilation defects via a minimal number of airway closure locations. *Ann Biomed Eng* 2009;37:286–300.
366 Leary D, Svenningsen S, Guo F, Bhatawadekar S, Parraga G, Maksym GN. Hyperpolarized ^{3}He magnetic resonance imaging ventilation defects in asthma: relationship to airway mechanics. *Physiol Rep* 2016;4:e12761.
367 Kang W, Tawhai MH, Clark AR, Sá RC, Geier ET, Prisk GK, *et al.* In silico modeling of oxygen-enhanced MRI of specific ventilation. *Physiol Rep* 2018;6:e13659.
368 Parr DG, Dirksen A, Piitulainen E, Deng C, Wencker M, Stockley RA. Exploring the optimum approach to the use of CT densitometry in a randomised placebo-controlled study of augmentation therapy in alpha 1-antitrypsin deficiency. *Respir Res* 2009;10:75.
369 Gerard SE, Herrmann J, Xin Y, Martin KT, Rezoagli E, Ippolito D, *et al.* CT image segmentation for inflamed and fibrotic lungs using a multi-resolution convolutional neural network. *Sci Rep* 2021;11:1455.
370 Xu Y, Sonka M, McLennan G, Guo J, Hoffman EA. MDCT-based 3-D texture classification of emphysema and early smoking related lung pathologies. *IEEE Trans Med Imaging* 2006;25: 464–475.
371 Hopkins SR. Ventilation/perfusion relationships and gas exchange: measurement approaches. *Compr Physiol* 2020;10:1155–1205.